Investigating the Effect of Biological and Chemical Factors on the Reaction Kinetics and Mineralogy of Ureolytic Bio-Cementation

Robert J Burdalski II

A thesis

submitted in partial fulfillment of the

requirements for the degree of

Master of Science in Civil Engineering

University of Washington

2020

Committee:

Michael Gomez

Brett Maurer

Program Authorized to Offer Degree:

Civil and Environmental Engineering

University of Washington

Abstract

Investigating the Effect of Biological and Chemical Factors on the Reaction Kinetics and Mineralogy of Ureolytic Bio-cementation

Robert J Burdalski II

Chair of the Supervisory Committee:
Michael Gomez
Civil and Environmental Engineering

Microbially Induced Calcite Precipitation (MICP) is a bio-mediated soil improvement method that has received significant recent attention for its ability to transform soil engineering properties through precipitation of calcium carbonate minerals on soil particle surfaces and contacts. Despite significant advances in treatment application techniques and characterization of post-treatment engineering properties, relationships between biogeochemical conditions during precipitation and post-treatment material properties have remained poorly understood. Bacterial augmentation, stimulation, and cementation treatments can vary dramatically in their chemical constituents, concentrations, and ratios between researchers, with specific formulas perpetuating despite limited understanding of their implications on reaction kinetics and end-state mineral products. In this study, small-scale batch experiments were used to systemically investigate how biogeochemical conditions during bio-cementation may influence ureolysis and calcium carbonate precipitation

kinetics and precipitate mineralogy using direct aqueous measurements, X-ray diffraction (XRD) analyses, and scanning electron microscope (SEM) imaging. The results of these experiments revealed that reactant concentrations, process by-products, and common soil cations such as magnesium can have significant effects on the kinetics of microbial ureolysis during bio-cementation. Additionally, experiments suggested that the presence of various biological factors including growth factors, non-ureolytic spectator cells, and extracellular polymeric substances may have important consequences with respect to the mineralogy, morphology, and distribution of produced bio-cementation. Through the identification of critical chemical and biological factors affecting bio-cementation material properties, the long-term chemical and mechanical resilience of bio-cementation can be better understood and improved.

TABLE OF CONTENTS

LIST OF FIGURES

LIST OF TABLES

ACKNOWLEDGEMENTS

First and foremost, I would like to thank my thesis advisor Professor Michael Gomez, who was willing to take a chance on me as his first master's track research assistant at the University of Washington and without whom this research would not have been possible. Professor Gomez introduced me to the world of biogeotechnics and was integral in guiding me through every step of this research project.

I would also like to thank all of my professors in the geotechnical department at the University of Washington, especially Professor Brett Maurer for his personal guidance, his offers of teaching assistantship, and his role as the second member of my thesis supervisory committee. Special thanks also go to Professor Drew Gorman-Lewis from the Earth and Space Sciences department, who provided valuable resources, feedback and direction during the small plate experiments, and his doctoral candidate Addien Wray, who aided in the total direct cell counts. Extra special thanks go to Professor Emeritus Bob Holtz, who provided me with guidance in the geotechnical world and whose eponymous fellowship helped fund the first year of my master's education.

Minyong Lee, doctoral candidate in the geotechnical department, spent countless hours helping, training, troubleshooting, and giving valuable feedback, and was an overall inspiration to work with as laboratory mate. Bruna Gabrielly, also a PhD student, helped with experiment preparation and sampling during winter quarter 2020. I would also like to thank the rest of my student peers and classmates at the University of Washington for their support, especially those in the Biogeotechnics Laboratory research group.

Presented XRD analyses and SEM images were made possible by the Molecular Analysis Facility, a National Nanotechnology Coordinated Infrastructure site at the University of Washington which is supported in part by the National Science Foundation (grant NNCI-

1542101), the University of Washington, The Molecular Engineering & Science Institute, and the Clean Energy Institute. Special thanks are extended to Scott Braswell and Samantha Young, who helped train me to use the SEM and XRD machines and also stepped in to collect data for this work when MAF facilities were otherwise unavailable to students due to the COVID-19 crisis.

Laboratory work would not have been possible without the help of Lab & Instrumentation Manager Sean Yeung at the More Hall Environmental Labs and Assistant Engineer Yiming Liu at the Geotechnical Lab. Thanks is also due to Nathaniel Peters, who aided in early experiments involving microscopy at the Keck Center at University of Washington.

Perhaps most importantly, a huge thank you to my partner Casey Heller, without whose hard work and unwavering support I would not have pursued the opportunity for my graduate studies and research work.

Funding for this research was provided by the National Science Foundation (ECI-1824647) and is greatly appreciated. Research collaboration made possible through the Engineering Research Center Program of the National Science Foundation under NSF Cooperative Agreement No. EEC_1449501 is also appreciated and acknowledged.

Any opinions, findings, conclusions, or recommendations expressed in this document are those of the author and do not necessarily reflect the views of the National Science Foundation or other funding sources.

Chapter 1. INTRODUCTION

Out of necessity, geotechnical engineering has traditionally employed energy-intensive or environmentally detrimental techniques in order to improve the engineering properties of soils. Similar to many other fields, over the past decade there has been increased interest in finding new ways to reduce the economic and environmental impacts of solving geotechnical problems. This motivation coupled with the realization that geotechnically-relevant soils contain a wealth of microorganisms capable of a diverse range of biogeochemical processes has helped generate an explosion of interest and research in the relatively young field of bio-inspired and bio-mediated geotechnics (Mitchell and Santamarina 2005; DeJong et al 2013). Bio-inspired geotechnics draw inspiration from natural biological systems to develop new geotechnical solutions, while bio-mediated geotechnics directly employ biogeochemical processes via living organisms to improve soil engineering properties (DeJong and Kavazanjian 2019). Bio-inspired and bio-mediated processes have the potential to increase the efficiency, applicability, speed, size, and range of traditional ground improvement methods while reducing economic and environmental costs.

Calcium carbonate ($CaCO_3$) mineral precipitation or bio-cementation technologies are particularly promising and perhaps the most widely-researched bio-mediated ground improvement processes to-date. One such bio-cementation method, is referred to as Microbially-induced Carbonate Precipitation (MICP) and involves the precipitation of calcium carbonate ($CaCO_3$) in soils induced via microbial urea hydrolysis. While lithification and cementation of soils and rocks already occur naturally over time as a result of physical, chemical, and biological processes, these processes are generally slow occurring over geologic time. Through the use of biological agents, however, cementation processes can be greatly accelerated when favorable chemical conditions

are provided. Although not generally observed at high abundances in nature, ureolysis-driven MICP is a powerful process that can be harnessed for soil improvement purposes by introducing or enriching native ureolytic microorganisms and injecting necessary chemical reactants into the subsurface.

Bio-cementation has the potential to transform soil engineering properties through the coating of soil particle surfaces, bonding of soil particles at contact locations, and increasing soil dry densities through the addition of precipitated $CaCO_3$ solids. Collectively these changes can result in increases in peak shear strengths, initial shear stiffnesses, and resistances to liquefaction triggering, while achieving reductions in soil porosities and hydraulic conductivities (Montoya and DeJong 2015; Minto et al., 2016; Gomez and DeJong 2017; Darby et al., 2019; Lee et al., 2020). Bio-cementation can be applied for a wide variety of geotechnical applications including improvements of foundation bearing capacities, mitigation of slope instabilities, improvement of soil erosional resistances, mitigation of earthquake-induced soil liquefaction, seepage control, and underground construction as well as other geoenvironmental applications including modification of groundwater flow, remediation of soils and groundwater via co-precipitation and immobilization of divalent contaminants, and wellbore repair and improvement (DeJong et al., 2006, 2013; Seagren and Aydilek 2010).When compared to other more commonly used ground improvement methods (e.g. jet grouting, deep dynamic compaction, chemical grouting), bio-cementation also has the potential to reduce environmental impacts by reducing the amount of energy and materials needed as well as eliminating the use of hazardous grouting materials like polyurethanes, which can contaminate soils and groundwater (Karol 2003).

1.1 BIO-CEMENTATION PROCESS

The process of bio-cementation via microbial urea hydrolysis begins with a chemical reaction wherein intra-cellular urease enzymes catalyze the hydrolysis of urea [$CO_2(NH_2)_2$], liberating ammonia (NH_3) and carbonic acid (H_2CO_3) (equation 1.1) (Stocks-Fisher et al., 1999; DeJong et al., 2006; Gomez et al., 2019). When the surrounding solution pH is not highly alkaline, some amount of this ammonia protonates to become ammonium (NH_4^+), thereby producing an equal amount of hydroxide (OH^-) ions (equation 1.2). The production of hydroxide ions consequently promotes the deprotonation of produced carbonic acid, forming increasing concentrations of bicarbonate (HCO_3^-) and carbonate (CO_3^{2-}) ions (equation 1.3). When calcium ions are present in sufficient quantities, and the product of the activities of calcium and carbonate ions exceed the solubility product of $CaCO_3$ minerals, the solution becomes supersaturated and calcium carbonate ($CaCO_3$) minerals are thermodynamically favored to precipitate (equation 1.4). This precipitation of calcium carbonate, or bio-cementation, can occur on soil particle surfaces and contacts thereby transforming soil engineering properties.

$$CO_2(NH_2)_2 + 2H_2O \rightarrow 2NH_3 + H_2CO_3 \quad (1.1)$$

$$NH_3 + H_2O \leftrightarrow NH_4^+ + OH^- \quad (1.2)$$

$$H_2CO_3 \leftrightarrow HCO_3^- + H^+ \leftrightarrow CO_3^{2-} + 2H^+ \quad (1.3)$$

$$Ca^{2+} + CO_3^{2-} \leftrightarrow CaCO_3 \quad (1.4)$$

Urease enzymes needed to complete urea hydrolysis and drive carbonate mineral precipitation are biogenically produced, existing in many bacterial, fungal, and plant species and play a critical role in nitrogen cycling. Most commonly, bacterial species containing active urease enzymes (ureolytic bacteria) are used to media bio-cementation in the process known as Microbially-induced Carbonate Precipitation (MICP) (DeJong et al., 2006). In particular, *Sporosarcina*

pasteurii (*S. pasteurii*) has been widely used due to its highly active enzymes, although many similar ureolytic bacterial species exist within natural soils (Graddy et al., 2018). Bio-cementation utilizing lab-cultured and injected *S. pasteurii*, or other ureolytic pure cultures, is the most common treatment technique used for MICP to-date and is commonly referred to as bio-augmentation (Ferris et al., 1997; DeJong et al., 2006; van Paassen et al., 2010). More recently, the selective enrichment and use of indigenous ureolytic bacteria, already present in naturals soils, to complete MICP has been shown to be effective in a process known as bio-stimulation (Fujita et al., 2000; 2008; Tobler et al., 2011; Burbank et al., 2011; Gomez et al., 2014; 2016; 2018). In addition to the use of whole ureolytic cells to complete ureolysis, other researchers have extracted urease enzymes most commonly from plants known to produce the enzyme, such as jack bean plants (*Canavalia ensiformis*) and soybeans (*Glycine max*) (Krajewska 2009). When urease enzymes are extracted from biological sources and used to catalyze urea hydrolysis for bio-cementation, without any microbial cells present, the process is referred to as Enzymatically-induced Carbonate Precipitation (EICP) (Hamdan and Kavazanjian 2016). The process offers the potential to increase reaction rates by removing diffusion limitations; however, notable differences have been observed between EICP and MICP (Nafisi et al., 2019)

1.2 Life-Cycle Performance of Bio-cementation and Mineral Stability

Before bio-cementation soil improvement can be expected to see wider implementation in geotechnical practice, critical knowledge gaps regarding the life-cycle performance and permanence of bio-cemented materials must be addressed. While several studies have examined the performance of bio-cemented soils when subjected to extreme environmental conditions such as freeze-thaw cycles and synthetic acid rain exposure (Chen et al., 2016; Cheng et al., 2016), these specific experiments do not address the broad range of geochemical conditions that bio-

cementation may be subjected to during and following practical field-scale applications. Additionally, no studies to-date have systematically investigated the performance of bio-cemented materials from the aspect of mineral stability and potential for long-term dissolution.

While the cementing agent in bio-cementation is often colloquially referred to as being calcite, the calcium carbonate minerals precipitated following urea hydrolysis have the potential to exist in a number of different crystalline structures called mineral polymorphs. Abiotically, the most abundant and thermodynamically stable polymorph at standard temperature and pressure is indeed calcite, which has a trigonal (rhombohedral) lattice structure (Bladh et al., 2001). Two other metastable crystalline phases of calcium carbonate exist rather commonly on earth; aragonite, which has an orthorhombic crystal structure, and vaterite, which has a hexagonal crystal structure and often appears in a spherical form (Bladh et al., 2001). In addition, calcium carbonate can exist in an amorphous calcium carbonate (ACC) form with no definitive crystalline structure. At temperatures near freezing, calcium carbonate can also be found in nature to exist as ikaite, which has a monoclinic crystal structure and often has a spike-like morphology (Bladh et al., 2001).

Each calcium carbonate mineral phase has different physical properties which in turn may translate to differences in engineering properties, making the mineralogy of precipitated calcium carbonate bio-cementation a matter of significant practical importance. For instance, the morphology and distribution of calcium carbonate precipitates on soil particle surfaces could have important engineering implications such as influencing soil tensile strengths, dilatancy, and interparticle friction angles (ϕ_{cv}'). In addition, calcium carbonate polymorphs all have different chemical stabilities, or thermodynamic solubility products (K_{sp}), which are expected to significantly influence their permanence following bio-cementation treatments. The K_{sp} of a mineral governs the conditions under which a mineral phase in contact with aqueous solutions will

be favored to dissolve, precipitate, or remain in equilibrium, although it does not control the rate at which these processes will occur (Sposito 2008). For a given solution, the tendency of calcium carbonate minerals to either precipitate or dissolve is described by the ratio of the ion activity product (IAP), which is the product of solution calcium (Ca^{2+}) and carbonate (CO_3^{2-}) activities, to the solubility product (K_{sp}) of a given calcium carbonate mineral phase. This ratio is commonly referred to as a solution's saturation ratio ($\Omega = IAP/ K_{sp}$). When $\Omega = 1$, the system is in equilibrium and neither precipitation nor dissolution are thermodynamically favored. When $\Omega > 1$, the solution is super-saturated with respect to a mineral phase and precipitation is favored. When $\Omega < 1$, the solution is under-saturated with respect to a mineral phase and dissolution is favored.

The K_{sp} values for common polymorphs of calcium carbonate relevant to MICP are shown in Table 1.1 (Plummer and Busenberg 1982; Gal et al., 2002; APHA 2005). More soluble polymorphs have higher K_{sp} values. As shown, the solubility of amorphous calcium carbonate ($10^{-6.40}$) is over two orders of magnitude larger than that of calcite ($10^{-8.48}$). Such vast solubility differences suggest that bio-cementation composed of calcite minerals may persist longer and in greater quantities than bio-cementation composed of other, less stable mineral phases, when dissolution is favored. Figure 1.1 shows the thermodynamic equilibrium lines ($\Omega = 1$) for different calcium carbonate mineral polymorphs of interest for bio-cementation.

Table 1.1. K_{sp} of Calcium Carbonate Polymorphs

Polymorph	**K_{sp} (at 20° C, 1 atm)**
Calcite	$10^{-8.48}$
Aragonite	$10^{-8.34}$
Vaterite	$10^{-7.91}$
Ikaite	$10^{-6.62}$
Amorphous $CaCO_3$	$10^{-6.40}$

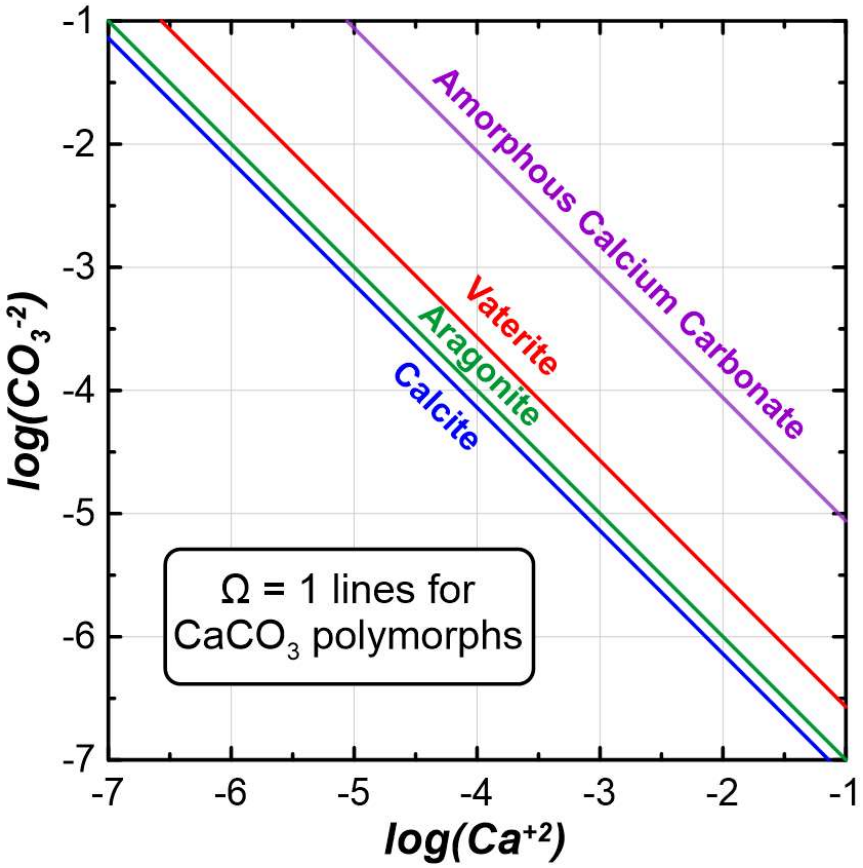

Figure 1.1 Thermodynamic equilibrium lines (Ω = 1) for calcium carbonate mineral polymorphs.

Mineral characterization analyses, most frequently X-ray diffraction (XRD) measurements, have been used in many past studies primarily to detect the presence of calcite as a means to confirm the generation of bio-cementation (Burbank et al., 2011; Kavazanjian et al., 2017; and others). In some of these XRD analyses the presence of other calcium carbonate polymorphs have also been detected. For example, Almajed et al., (2017) found that bio-cementation displayed increases in calcite rather than vaterite or aragonite when bulk ureolysis rates were reduced in EICP experiments. Zhang et al., (2015) observed that the formation of aragonite instead of calcite was favored when acetate was present. In a meter-scale MICP experiment using both stimulation

and augmentation methods, Gomez et al., (2016) observed that aqueous solution IAP values approached the K_{sp} of calcite as solutions approached equilibrium.

While the formation of abiotic mineral phases can be predicted thermodynamically, less thermodynamically favorable calcium carbonate polymorphs have been observed to form and remain stable over long periods of time when biogenic factors are present (Raz et al., 2003, Al-Sawalmih et al., 2009, and many others) The American Lobster (*Homarus americanus*), for example, has been observed to maintain stable amorphous calcium carbonate throughout its yearly molt cycle (Addadi et al., 2003). Both amorphous calcium carbonate and aragonite were also found to be abundant in the process of bivalve shell formation, with the disordered ACC serving to isolate pathogens and promote shell repair when infected with a shell disease (Huang et al., 2018). Under abiotic conditions and standard temperature and pressure, these same metastable mineral phases often exist only briefly before dissolving and reprecipitating into more stable mineral phases, while always moving towards the mineral phase with the lowest K_{sp}, calcite, in a process known as Ostwald ripening (Zhou et al., 2010). However, when biogenic agents are present, the Ostwald ripening process can be disrupted and/or stalled leading to the prolonged stability of otherwise thermodynamically unfavorable phases like aragonite and vaterite (Myszka et al., 2019). Vaterite crystals have been observed to form in otherwise unfavorable thermodynamic conditions in the presence of xantham gum and various amino acids (e.g. glutamic acid, aspartic acid). In fact, the presence of vaterite in natural $CaCO_3$ precipitates has even been suggested as being potentially indicative of the presence of biofilms or mucilage-producing organisms at the time of mineral formation (Braissant et al., 2003).

1.3 TREATMENT APPROACHES

Researchers investigating MICP have used a wide range of different chemical reagents and reagent concentrations in applied bio-cementation treatment solutions. As shown in equations 1.1. and 1.4, the bio-cementation reaction network requires both urea and calcium sources for microbially-mediated carbonate production and calcium carbonate precipitation, respectively. As shown in Figure 1.2, the magnitudes and ratios of supplied urea and calcium reagents, however, have varied widely between researchers over the past 25 years. While many MICP studies have employed urea-to-calcium ratios of 1.0 (Whiffin et al. 2007; van Paassen et al. 2010; Mortensen et al. 2011; Al Qabany et al. 2012; Cheng et al. 2013; Dawoud et al. 2014; Minto et al. 2016; and many others), many other studies have involved much higher urea to calcium ratios. For example, urea-to calcium ratios between 1.3 and 2.0 have been used in many past studies (Chu et al. 2012; Montoya et al. 2013; Gomez et al. 2014; 2016; 2018, Kavazanjian et al. 2017; and others), with much higher ratios exceeding 100.0 (Ferris et al. 1997); Chou et al. 2011) in some cases. In these same studies, concentrations of urea and calcium have exhibited similarly large variations with concentrations ranging from ~25 to 3000 mM and ~2.4 to 2000 mM, respectively. Higher concentrations of urea used in MICP applications may have been intended to ensure increased availability of carbonate ions for $CaCO_3$ precipitation in the event of incomplete ureolysis. As shown in more recent studies, however, excess urea is not required for near full precipitation of supplied calcium and the use of excess urea decreases the material efficiency of applied bio-cementation treatments. While large variations in urea-to-calcium ratios and reagent concentrations were to be expected during the early development of this technology, as shown in Figure 1.2 , large variations in these values still exist between even the most recent studies. Significant discrepancies in treatment formulations between current studies, suggest that

researchers have yet to reach firm conclusions regarding the effect of urea and calcium ratios and concentrations on bio-cementation, despite twenty five years of research, Urea and calcium concentrations may have dramatic implications for the life cycle environmental impacts of MICP by affecting both material and energy consumption during treatment applications (Gebrehiwet et al. 2012) as well as the long-term permanence of bio-cementation.

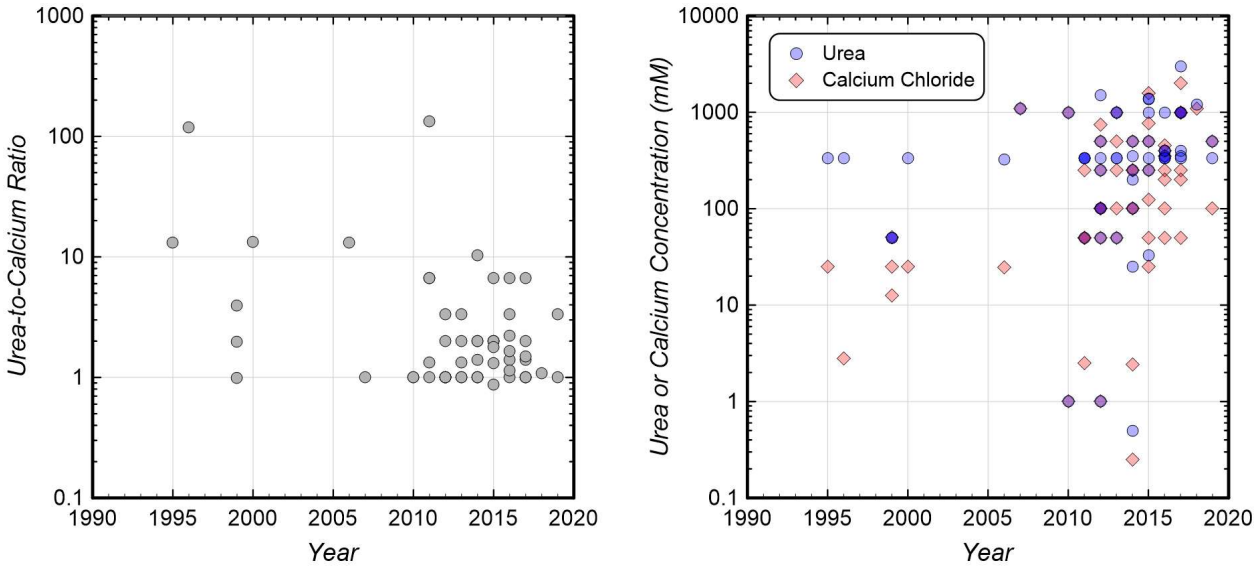

Figure 1.2 Urea and calcium concentrations and urea-to-calcium ratios from past MICP studies show that large variations in treatment techniques have persisted over the past 25 years.

In addition to urea and calcium, many other chemical constituents are also added to bio-cementation treatment solutions. For example, chemical compounds containing nutrients needed for microbial growth, or growth factors, are almost universally applied with cells during augmentation injections and are also oftentimes included in bio-cementation solutions. These growth factors provide trace minerals, amino acids, proteins, and respirable carbon necessary to maintain and grow ureolytic cell populations. Many of these growth factors used in past MICP studies, such as yeast extract, nutrient broth, molasses, corn steep liquor, and beef extract, have no

definitive elemental composition and thus can vary widely between different manufacturers and products types. Other studies have also included more well-defined nutrient sources such as sodium acetate, a non-fermentable carbohydrate which does not contain amino acids or proteins. Beyond growth factors additions, a variety of other treatment additions have also been used in past studies including sodium bicarbonate (Ferris et al., 1996; and many others), ammonium chloride (Chou et al. 2011; Gomez et al. 2017; and many others), ammonium sulfate (Zhang et al., 2018), and tris base (Zhang et al. 2018). In addition to impacting material usage and therefore environmental impacts and economic costs, it is hypothesized that the selection of treatment additives and supplied growth factors may significantly impact the mineralogy and physical properties of bio-cementation. Currently the implications of these different treatment solution additions on the performance of bio-cementation remains unknown.

Although researchers have the opportunity to directly control bio-cementation treatment solution compositions, many other biogeochemical conditions are governed by environmental factors related to the application location including parent soil mineralogy, groundwater composition (ions, pH), temperature, and the presence of other existing microorganisms and biogenic organic compounds. Unlike treatment additives, the presence and impact of these different factors may be unavoidable. The effects of solution chemistry and pH have been studied to some extent in past studies (Mortensen et al. 2011; Cheng et al. 2014; Putra et al. 2016; and others), however, these experiments generally involved only measurements of global engineering properties, which may not be able to resolve differences in precipitate structure and mineralogy. Additionally, oftentimes such studies have involved multiple simultaneous biological, chemical, and physical changes making it difficult to attribute observed differences to specific isolated mechanisms.

Abiotic calcium carbonate synthesis experiments conducted under more controlled conditions suggest that even small changes in solution chemistry can dramatically alter $CaCO_3$ precipitate formation. For example, Berner et al. (1975), Zhang et al. (2000), and Meldrum et al. (2001) all observed large changes in calcite precipitation kinetics and precipitate morphology when trace concentrations of magnesium (Mg^{2+}) were added. Busenberg and Plummer (1985) found that sulfate (SO_4^{2-}) concentrations commonly found in marine waters can significantly inhibit calcite precipitation rates. The presence of manganese, strontium, and phosphate have also been identified as important factors influencing calcium carbonate precipitation (Morse et al. 2007). While it remains unclear what impacts specific treatment additives and environmental conditions have on the physical and chemical properties of bio-cementation, it is clear that these factors merit closer investigation and may have significant consequences for the long-term performance of bio-cemented soils.

Chapter 2. SMALL PLATE BATCH REACTOR EXPERIMENTS

The identification of key chemical and biological factors that control bio-cementation material properties will likely be critical towards understanding how MICP may perform when applied to different field sites. While applied treatment solutions can be formulated as desired, environmental factors including groundwater chemistry and soil mineralogy are unavoidable and uncontrollable factors that could have dramatic effects on the end-state mineral products formed during MICP. Past MICP studies have attempted to characterize end-state precipitate properties; however, complex and simultaneous changes in biological, chemical, and physical factors encountered during precipitate synthesis between studies have hindered the ability of researchers to attribute observed properties and behaviors to more specific isolated changes and mechanisms. Understanding the relationships between biogeochemical reaction conditions during precipitation and post-treatment material properties are key towards answering practical questions regarding site selection for MICP applications as well as better understanding the engineering performance of bio-cementation materials including long-term chemical and mechanical resilience over a wide variety of conditions.

Most laboratory studies have not been well suited to examine a wide range of conditions due to the effort, time, and materials needed to complete individual experiments. For example, soil column experiments are relatively time and material intensive and generated results necessarily involve other complicating factors related to reactive transport in soils. In this study, a small-scale plate batch experiment was developed and used to investigate the effects of a wide range of chemical and biological factors on MICP process reaction kinetics and precipitate mineralogy and morphology. These batch experiments minimized experimental time and materials needed in comparison to other testing venues and may allow researchers to investigate isolated mechanisms

more systematically between experiments. Furthermore, batch experiments homogenize solutions, thus eliminating potential reactive transport effects, and involve only single treatment applications. The use of batch experiments in this study was intended to increase the range of factors that could be practically investigated. The relative simplicity of the set-up and ability to tightly control test conditions between experiments enabled systematic isolation and attribution of experimental results to more specific individual factors.

During all experiments, small volume solution samples were collected in time to capture both ureolysis and precipitation kinetics through direct urea and soluble calcium measurements. Following experiments, end-state bio-cemented materials were preserved and scanning electron microscopy (SEM) imaging and X-ray diffraction (XRD) analyses were used to characterize the morphology and mineralogy of synthesized calcium carbonate precipitates. A PHREEQC batch reaction model was also used to estimate applied cell densities and examine the effect of various factors on microbial activity. Ultimately, the presented batch reactor set-up is intended to provide a new venue through which critical knowledge gaps in our understanding about the effect of biogeochemical conditions during precipitation can be addressed. In this study, performed experiments specifically focused on factors expected to control long-term material performance and affect field-scale treatment applications including changes in $CaCO_3$ crystal morphology, distribution, and mineralogy as well as microbial and precipitation reaction kinetics.

2.1 Experimental Set-Up

2.1.1 *Soil Materials*

All plate batch experiments were performed using Ottawa F-65 silica sand (U.S. Silica) with the exception of soil type experiments presented in Chapter 3.7. Ottawa F-65 soil material

classifies as a poorly-graded sand (SP) with a D_{10} of 0.13mm, a D_{30} of 0.18 mm, a D_{60} of 0.23 mm, and no fines (Carey et al. 2019). XRD analysis performed on untreated Ottawa F-65 sand indicated that its mineralogy was composed of greater than 90% quartz.

2.1.2 *Sporosarcina pasteurii Cell Culture Preparation*

Sporosarcina pasteurii (*S. pasteurii*) cells were prepared for plate batch experiments using ATCC 11859 growth media consisting of 15.74 g/L tris base, 20 g/L yeast extract, and 10 g/L ammonium sulfate, that was pH-adjusted to 9.0. Following preparation, growth media was autoclaved at 121ºC for 24 minutes, cooled to room temperature (23ºC), and inoculated with a *S. pasteurii* frozen stock culture (ATCC 11859). The *S. pasteurii* frozen stock culture consisted of 25% glycerol by volume (diluted in water) and was stored at -80ºC following preparation from an ATCC 11859 freeze-dried pellet wherein plating and isolation of a single colony was used to inoculate previous growth media. Inoculated growth media was incubated for 48 hours at 30ºC on an orbital shaker at 175 rpm before harvesting. Concentrated *S. pasteurii* cell pellets were created by centrifuging 50 mL of incubated cell growth media in a conical-bottom tube for 10 minutes at 4200 rpm and then removing the supernatant. The remaining cells in the conical-bottom tube were then rinsed using 50 mL of autoclaved isotonic saline solution (154 mM NaCl), mixed thoroughly, and centrifuged again until the supernatant appeared to be clear (typically 2 rinses). A final cell suspension was created by adding 10 mL of isotonic saline to the remaining bacterial cells and mixing thoroughly. The OD_{600} of this 10 mL suspension was measured using a microplate spectrophotometer and typically ranged between 1.5 and 1.6, which was estimated to correlate to between 2.7 and 3.3 x 10^9 cells/mL based upon a lab-specific total direct cell count to OD_{600} correlations.

2.1.3 *Bio-Cementation Treatments*

Plate batch experiments were conducted in 100 mm x 15 mm flat bottom glass petri dishes (Pyrex, Corning Inc.). Each experiment included 5.3 grams of soil material and 44 mL of cementation solution unless otherwise noted. Prior to starting experiments, the 5.3 grams of Ottawa F-65 sand was augmented with a *S. pasteurii* cell suspension, mixed to promote an even distribution of cells across particle surfaces, and allowed to reside overnight at 1.6°C in order to mimic current treatment processes wherein soils are first augmented or stimulated to achieve ureolytic activity and then subsequently cemented. At the start of each experiment, 44 mL of prepared cementation solutions were first added to augmented sand materials, vortexed at 800 rpm for 10 seconds, placed into the petri dish, and then covered with parafilm to minimize solution/air interactions and potential evaporation.

Cementation solutions were prepared by mixing solutions of urea (Fisher Scientific, 99.2% assay) and calcium chloride dihydrate (Fisher Scientific, >99.0% assay) in deionized water at the desired concentrations and ratios. All sets of experiments included a control specimen that received solutions with 250 mM urea and calcium chloride at a 1:1 ratio and an estimated *S. pasteurii* cell density of approximately 1.8×10^7 cells/mL. This control specimen was intended to provide a consistent reference condition for all experiments, which were conducted at different times, allowing for small rate differences resulting from slight variations in temperatures, microbial concentrations, and microbial activities to be accounted for. Control specimens also allowed for the variability in obtained results expected between identical experiments to be understood and quantified.

Monitoring of all experiments was completed during ureolysis and precipitation reactions which occurred over various time intervals up to 76 hours, with most tests completed after only 24

hours. Upon completion of experiments, all remaining solutions were collected from petri dishes and frozen for future analysis. Remaining bio-cemented materials were rinsed twice with 96% ethanol by volume (diluted in water) to cease microbial and ureolytic activity, remove soluble reaction by-products, and limit the potential for subsequent precipitate changes including dissolution in time. Precipitates were then stored in a vacuum desiccator at a relative humidity of less than 10% to prevent potential degradation and other mineralogical changes associated with the presence of water.

2.2 PHREEQC BIOGEOCHEMICAL MODELING

PHREEQC (Parkhurst and Appelo 2013), an open-source USGS geochemical code, was used to estimate cell densities for all plate batch experiments. *S. pasteurii* cell densities were estimated by matching a Michaelis-Menten cell normalized ureolysis kinetic model to observed urea concentration measurements in time. In order to match this model to experimental observations, ureolytic cell density inputs to the model were varied to match the observed initial ureolysis rates (from ≈250 mM to 200 mM urea), recognizing that changes in microbial activity may occur during reactions due to a number of factors including cell death and encapsulation. It should be noted that these cell density estimates were based solely on observed microbial activity. Other cell density estimates were also made using OD_{600} measurements using a lab-specific OD_{600} to total direct count relationship. When urea degradation trends modelled using the Michaelis-Menten kinetic were compared to actual direct urea measurements from experiments, generally modelled results suggested greater urea degradation than experiments particularly when reactions proceeded to greater than 75% completion. As such, care was taken to fit the Michaelis-Menten model to

experimental urea degradation trends only at the start of experiments were more limited changes in cell viability would be expected.

2.2.1 *Input Parameters*

In this PHREEQC model, microbial ureolysis was modeled using a cell-normalized Michaelis-Menten kinetic rate expression (2.5) following Lauchnor et al. (2015):

$$Bulk\ ureolysis\ rate\ \left(\frac{mM}{hr}\right) = \frac{d[urea]}{dt} = [X]\left(\frac{V_{max}[urea]}{K_m + [urea]}\right) \quad (2.5)$$

In this expression, *d[urea]/dt* is bulk urea hydrolysis rate in solution in units of mM of urea per hour, *[urea]* is urea concentration in units of mM urea, *[X]* is ureolytic cell density in units of cells per mL, V_{max} is the maximum ureolysis rate per cell in units of millimoles of urea hydrolyzed per hour per cell, and K_m is the half-saturation coefficient for urease enzymes in whole *S. pasteurii* cells in units of mM urea. Whole cell kinetic parameters reported by Lauchnor et al. (2015) for *S. pasteurii* (ATCC 11859) were implemented in this model, where V_{max} was 6.4 x 10^{-9} millimoles of urea $cell^{-1}$ $hour^{-1}$ and K_m was 305 mM. It should be mentioned that enzyme inhibition and all other kinetically-controlled reactions including calcite precipitation were not considered in this model.

2.2.2 *Comparison to Total Direct Cell Counts*

S. pasteurii cell densities used in plate experiments were also more directly estimated using OD_{600} measurements completed using a microplate spectrophotometer (Biotek, Inc.). OD_{600} measurements provide an indication of aqueous turbidity, which can be reliably correlated to bacterial cell densities (Mandelstam et al., 1968). The wavelength of 600 nm is commonly used for measurements as it provides a reliable peak in absorbance yet does not damage cells or impact cell growth. While OD_{600} measurements are effective at measuring relative changes in cell

densities between samples, they do not provide direct estimates of cell densities alone. In order to quantify cell densities using spectrophotometer measurements, a total cell density to OD_{600} relationship is needed and was determined for the spectrophotometer used in this study using total direct cell counts. Total direct cell counts are a well-established method of directly estimating aqueous cell densities (Hobbie et al., 1975). In this method, diluted cell populations are dyed, filtered, and prepared on a microscope slide and visually counted using an epiflourescent microscope. Cell densities are then estimated from known cell culture volumes and the areas over which counts occur.

In order to conduct total direct cell counts, four *S. pasteurii* cell suspensions were prepared in sterile saline solution and were diluted to within the cell range tolerance for direct counting (between approximately 20 and 70 cells per field of view). For each of these samples, a solution aliquot between 50 and 350 μL was pipetted onto a black polycarbonate membrane filter and dyed using Invitrogen SYBR Green I Nucleic Acid Gel Stain. Microscopic direct counting was performed by counting the bacterial visible in ten different sites across the sample using an epifluorescent microscope calibrated to a known field of view. Cell densities (units of cells per mL) were then calculated using equation 2.6, where X_c is the number of bacteria counted in one microscopic image, A_{FOV} is the area of the field of view (6000 μm^2), A_f is the area of the filter used, and V_s is the volume of the aliquot used.

$$\frac{cells}{mL} = \left(\frac{\frac{X_c}{A_{FOV}} * A_f}{V_s} \right) \tag{2.6}$$

Using cell density estimates from total direct cell counts as well as the dilution ratio to OD_{600} relationship for the spectrophotometer, a cell density to OD_{600} relationship was established for the specific spectrophotometer device and preparation protocol used in this study. Figure 2.2 presents

this cell density to OD_{600} relationship. Cell densities used for each point on this calibration curve were the average of ten different values of X_c (microscope counts).

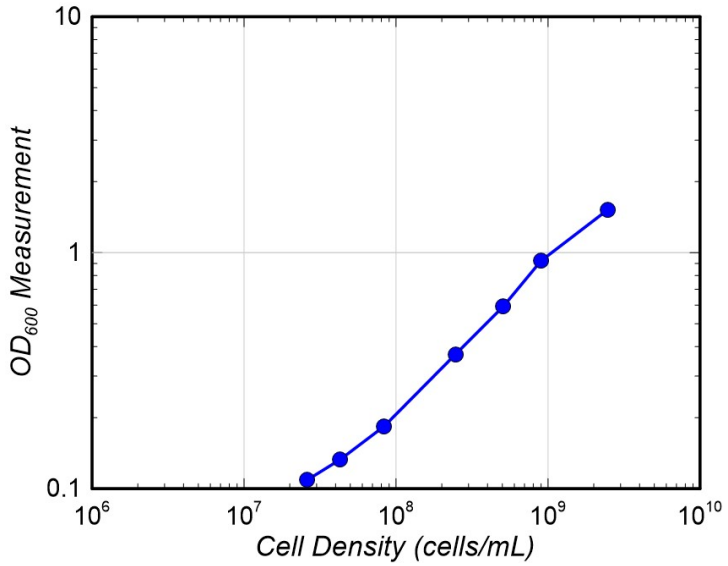

Figure 2.1 Cell density to OD_{600} relationship determined for lab-specific spectrophotometer using total direct cell counts.

Inoculant cell densities for all plate batch experiments were estimated using this OD_{600} to cell density relationship. Using these OD_{600} based cell density estimates, the cell-normalized Michaelis-Menten kinetic rate expression for ureolysis (Equation 2.5) was then used to predict ureolytic rates for experiments as previously described. In particular, OD_{600}-based initial ureolytic rate estimates (at a urea concentration of 250 mM) were compared to experimentally observed initial ureolytic rates, to which the Michaelis-Menten kinetic model was calibrated to as previously described. Figure 2.2 presents a comparison of these two rate estimates for all thirteen control plate batch experiments conducted throughout the course of this study. All control experiments were prepared following identical procedures, as described previously, and included equimolar concentrations of 250 mM urea and soluble calcium.

As shown in Figure 2.2, OD_{600}-based initial ureolytic rate estimates were consistently higher than experimentally observed initial ureolytic rates to which the Michaelis-Menten kinetic was calibrated to. This discrepancy can likely be explained by the fact that the total direct cell count method assumes that all observed cells, whether living or dead, contribute to bulk urea hydrolysis activity. In these experiments, ureolytic activity was expected to be highly dependent on applied cell concentrations, but it can also be affected by other factors including changes in cell viability, temperature, and other environmental conditions. Variations between observed ureolytic activity and OD_{600}-based activity estimates may reflect the impact of the above factors, but may also suggest that the whole cell Michaelis-Menten kinetic parameters from Lauchnor et al. (2015) for *S. pasteurii* (ATCC 11859) may not reasonably reflect per cell activity for our specific experiments. Additionally, it should be mentioned that variations in ureolytic activities were also experimentally observed between specimens with similar OD_{600} values, suggesting that small differences in inoculant activities may have inherently resulted from minor variations in incubation periods, harvesting and rinsing procedures, and other factors.

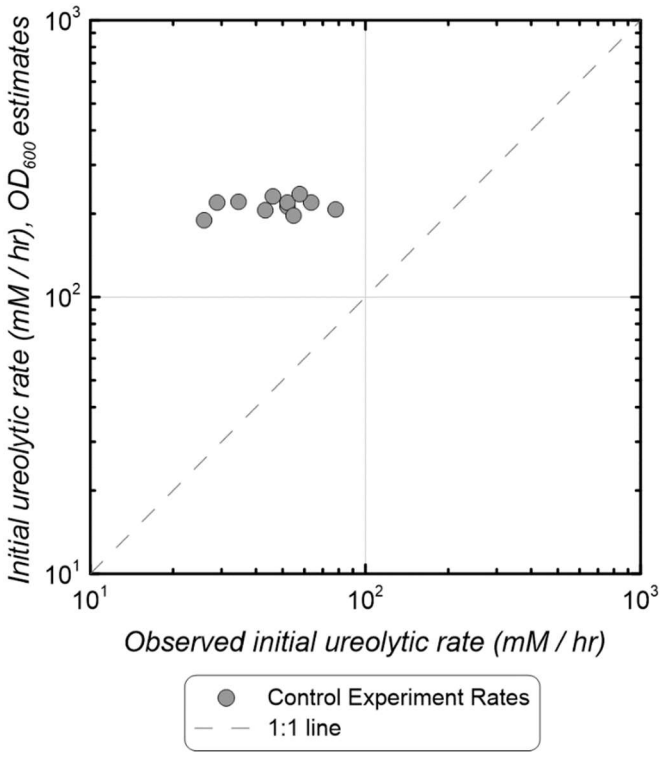

Figure 2.2 Comparison between initial ureolytic rates estimated from OD_{600} measurements and initial ureolytic rates experimentally observed for the 13 control experiments completed in this study containing 250 mM urea and calcium. Initial rates were calculated from cell density estimates using the cell-normalized Michaelis-Menten kinetic rate expression (Equation 2.5) with parameters from Lauchnor et al. (2015).

2.3 Biogeochemical Monitoring and Analysis

2.3.1 *Small-Volume Sampling*

Aqueous solution samples of 120 µL were collected from batch experiments at pre-determined time intervals to capture changes related to urea hydrolysis activity and calcite precipitation. Sampling was completed more frequently at the start of experiments wherein large chemical changes were occurring and intervals were informed by expected ureolytic rates and the PHREEQC batch reaction model. For all experiments, care was taken to ensure the total sampled

volume would never exceed 10% of the total volume of the solution available (sampled volumes were less than 4.5 mL for all experiments). All aqueous samples were taken near the center of plate experiments using a pipette (Raining Pipet-Lite XLS) with disposable polypropylene tips. Samples were then pipetted into a 2.0 mL conical tube with a 0.22 μm filter (Costar Spin-X cellulose acetate centrifuge tube filter) and centrifuged at 1318 g for a minimum of 30 seconds to remove all solid precipitates and soil solids that may have been suspended in the solution. 80 μL of this filtered solution was then added to 300 μL of 1 N hydrochloric acid and mixed thoroughly using a vortexer. Acid stabilization of the sample was intended to prevent volatilization of produced ammonia and limit the potential for continued ureolytic activity and calcium carbonate precipitation reactions. All aqueous samples were frozen immediately after stabilization until thawing for subsequent chemical analyses.

2.3.2 *Aqueous Chemical Measurements*

Aqueous urea measurements were completed for all samples using a urea assay protocol modified from Knorst et al. (1997) wherein a colorimetric reagent consisting of 4% (w/v) p-Dimethylaminobenzadehyde, and 19% (v/v) HCl in 96% ethanol was added to dilute sample volumes. Absorbance values were measured at 422 nm using a microplate spectrophotometer and compared to calibration curve relationships. Calcium measurements were completed using a QuantiChrom Calcium Assay Kit (BioAssay Systems). Calcium samples were first diluted in Milli-Q purified ultrapure water (containing less than 7.2×10^{-9} mM Ca^{+2}) to achieve concentrations within the linear range of the assay (< 5.0 mM Ca^{+2}). 200 μL of a colorimetric reagent was then added to samples and color changes were allowed to develop for at least 10 minutes before measurements. Absorbance values were then measured at 612 nm using a microplate spectrophotometer and compared to calibration curve relationships. Figure 2.3 provides

example calibration curves for both the urea assay (2.3a) and the calcium assay (2.3b) used in this study.

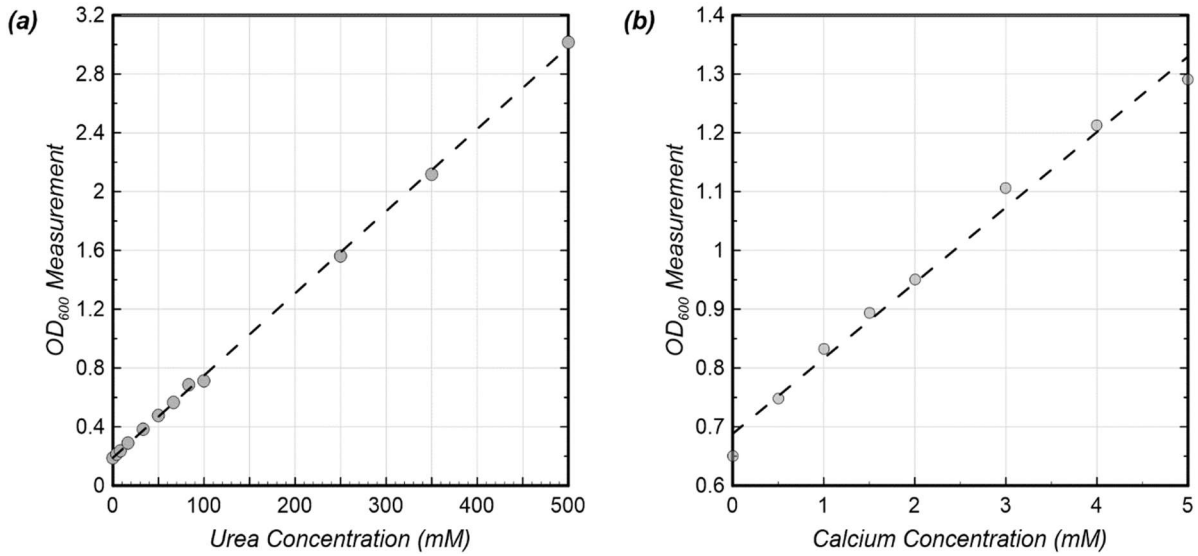

Figure 2.3 Example calibration curves for (a) urea and (b) calcium assays.

2.3.3 *X-ray Diffraction Analyses*

X-ray diffraction (XRD) analyses were performed on end-state precipitate materials to characterize their mineralogy, specifically focusing on detecting and quantifying the presence of calcium carbonate polymorphs such as calcite, vaterite, and aragonite. XRD was also used to identify parent soil minerals and the presence of any other precipitated minerals that may have been produced from various chemical reactions. All XRD analyses were performed using a Bruker D8 Discover X-ray powder diffractometer with a IμS 2-D powder microfocus source, a high-efficiency Cu anode, and a Pilatus 100k large-area 2-D detector. Scans were performed using a phi rotation for 45 seconds for 2Theta (2θ) values from 16° to 93° at increments of 11°. Samples were prepared from ethanol-rinsed precipitates obtained from plate experiments and were ground into a fine powder with particle sizes ranging from 10 to 50 μm using an agate mortar and pestle prior to

XRD analyses. S-Q analysis of the obtained diffraction patterns was performed to estimate relative quantities of the different mineral phases present using Diffrac.EVA XRD software (Bruker).

Mineralogy was assessed for all specimens using X-ray diffraction to identify the presence of calcite, vaterite, and aragonite, each of which can be identified via a representative diffraction spectrum. Since X-ray diffraction relies on comparing known refracted angles of X-rays by various crystalline atomic structures, it is unable to reliably identify amorphous phases such as amorphous calcium carbonate. For further investigation of the abundance of amorphous calcium carbonate in obtained precipitates, other methods of identification like Fourier-transform infrared spectroscopy (FTIR) may be necessary.

2.3.4 *Scanning Electron Microscope Imaging*

Scanning electron microscope (SEM) imaging was completed to visually examine the morphologies of precipitated calcium carbonate minerals. SEM images also provided the opportunity to examine the relative size, shape, and distribution of calcium carbonate crystals within bio-cemented sand specimens, as well as other physical differences. All SEM imaging was performed using a FEI XL830 Dual-Beam Focused Ion Beam Scanning Electron Microscope. Prior to imaging, ethanol-rinsed precipitates from plate experiments were sub-sampled and coated using a 60%/40% Gold/Palladium (Au/Pd) alloy target for 60 seconds at an approximate deposition rate of 13 nm/min in an Argon gas chamber using an SEM sputter coater. This process was completed to increase the conductivity of the samples, thereby increasing their stability under the electron beam and achieving higher resolution imaging.

Chapter 3. EFFECT OF CHEMICAL FACTORS ON MICP

3.1 CALCIUM AND UREA CONCENTRATIONS

One of the first decisions to be made when formulating MICP treatment solutions, is the selection of urea and calcium concentrations in cementation solutions. In order to investigate the consequences of urea and calcium concentration changes on MICP, four plate batch experiments were performed. All plate experiments had a urea-to-calcium concentration ratios of 1 and included reagents at equimolar concentrations of either 50 mM, 250 mM, 500 mM, or 1250 mM.

3.1.1 *Ureolytic Rate Effects*

Figure 3.1 presents normalized concentrations of urea and calcium (C/C_0) in time for all four urea/calcium concentration experiments. Normalized concentrations were used to better compare concentrations observed in time (C) to the initial concentrations (C_0) measured at the start of each experiment (i.e. applied solution concentrations). All experiments were inoculated with an estimated cell density of 7.4×10^7 cells/mL of *S. pasteurii* cells. As shown, urea (Figure 3.1a) and calcium (Figure 3.1b) concentrations followed similar trends in time. Similar temporal trends in urea degradation and calcium consumption suggested that the kinetics of microbial ureolysis appeared to govern the rate of calcium carbonate precipitation reactions for each of these experiments. Despite this general agreement, a small time lag did exist between urea degradation and calcium consumption trends in time and suggested that although calcium carbonate precipitation appeared to occur soon after urea hydrolysis, the precipitation reaction was somewhat slower.

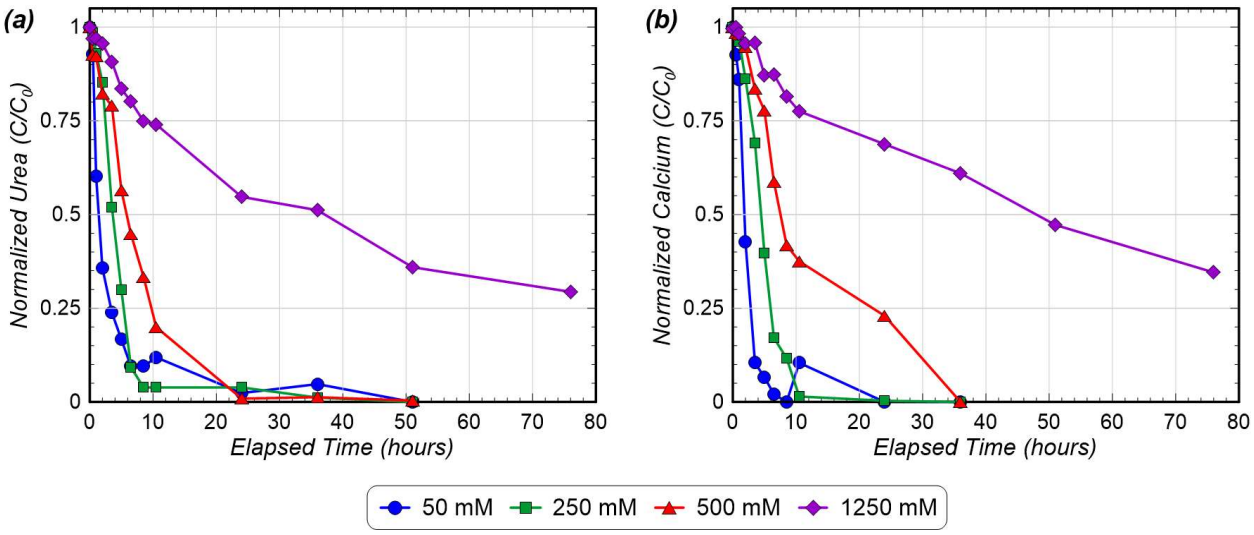

Figure 3.1 Normalized concentrations of (a) urea and (b) calcium in time measured during concentration varied experiments with urea-to-calcium ratios of 1.

In order to further compare the rate at which calcite precipitation and ureolysis reactions proceeded, the concentrations of both urea and soluble calcium at each point in time during experiments were compared (Figure 3.2). In general, concentrations of urea appeared to be less than or equal to concentrations of calcium at all points in time. As mentioned previously, although the rate of calcium carbonate precipitation was slightly slower than ureolysis, the proximity of all data points to the 1:1 line suggested that precipitation reactions occurred relatively quickly after urea degradation in all experiments. Thus, for practical reactive transport modelling purposes, the kinetics of calcium carbonate precipitation may be sufficiently fast to be approximated as an equilibrium reaction with overall precipitation rates largely governed by urea hydrolysis rates. These results agree well with similar approaches taken in more recent reactive transport modelling efforts (Nassar et al. 2018).

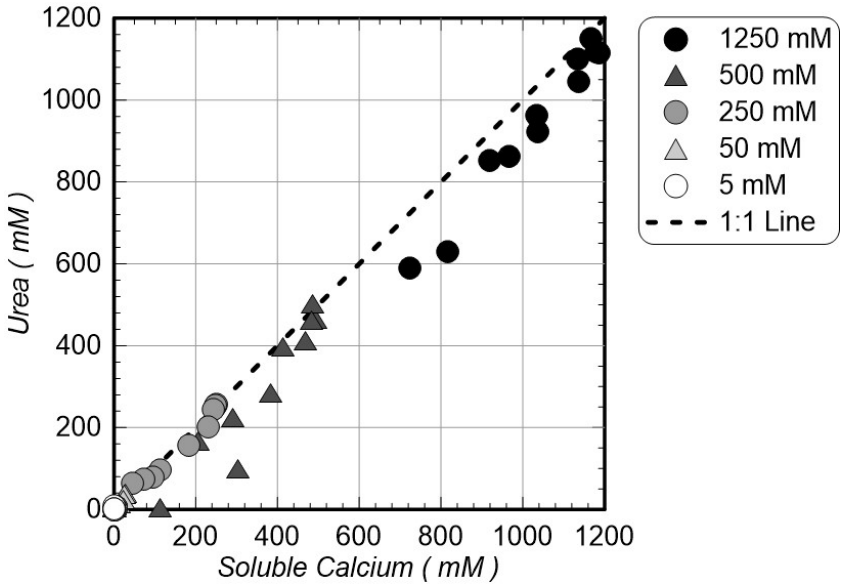

Figure 3.2 Comparison of urea and calcium concentrations during urea/calcium concentration experiments.

Figure 3.3 shows normalized concentrations of urea in time for each of all four experiments compared to rates predicted by the PHREEQC Michaelis-Menten ureolysis model assuming a constant cell density of 1.8 x 10^7 cells/mL. The modelled cell density was selected following the results of the ureolytic rate varied experiments as described further in Chapter 4.1, which involved equimolar urea and calcium concentrations of 250 mM. Thus, as expected, modelled urea degradation trends matched well with the 250 mM control condition (Figure 3.3b). Modelled urea degradation trends were intended to compare experimentally observed ureolytic rates to predicted ureolytic rates assuming a stationary cell density and acknowledging rate dependencies on changes in urea concentrations. For the 50 mM (Figure 3.3a) and 250 mM (Figure 3.3b) concentration experiments, experimentally observed rates matched favorably with the PHREEQC modelled trends. At higher chemical concentrations, however, the experimentally observed rate was moderately slower than predicted for the 500 mM experiment (Figure 3.3c) and experimental trends were substantially slower than that predicted for the 1250 mM experiment (Figure 3.3d).

Discrepancies between experimentally observed rates and PHREEQC model predictions at high chemical concentrations were believed to have resulted from several possible mechanisms including: (1) potential inhibition of ureolysis due to higher ionic strengths in the high concentration experiments, (2) potential reductions in viable cell densities in time due to the absence of growth factors and long reaction times, and (3) the presence of greater magnitudes of calcium carbonate precipitation in higher concentration experiments and potential encapsulation of cells within the precipitated crystal structure (Phoenix et al. 2012). While all of the above mechanisms may have contributed to ureolytic activity decreases in time in the higher concentration experiments, the presence of higher precipitation magnitudes seemed particularly impactful. During precipitation events, the coating of bacterial cells with $CaCO_3$ minerals, or cell encapsulation, could have resulted in cell death, reductions in cellular diffusion, and isolation of cells from bulk aqueous solution, therefore decreasing the ability of cells to actively participate in urea hydrolysis.

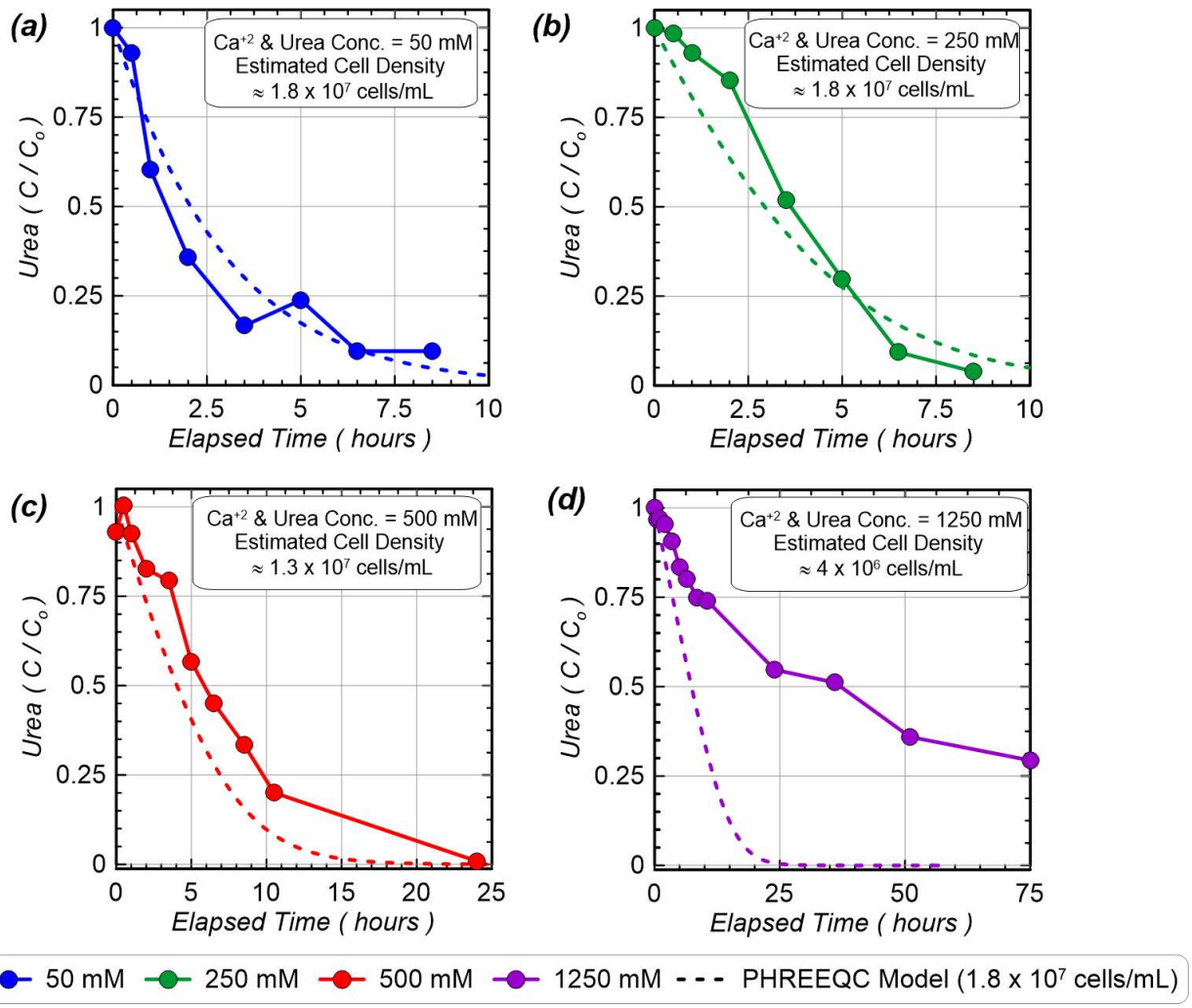

Figure 3.3 Normalized concentrations of urea in time for (a) 50 mM, (b) 250 mM, (c) 500 mM, and (d) 1250 mM experiments with predicted urea degradation trends from the PHREEQC model assuming a constant cell density of 1.8 x 10^7 cells/mL. The PHREEQC model was also calibrated to observed urea degradation trends and estimates of the "observed cell densities" are provided in upper right text blocks.

In order to better understand the mechanism responsible for these decreases in ureolytic rates at higher concentrations of urea and calcium, a series of additional plate experiments were performed. Two plate experiments were prepared following identical protocols as previous experiments and included 1250 mM urea and calcium (urea-to-calcium ratio of 1). A third plate experiment was also prepared with 1250 mM urea and included no added calcium. One of the 1250

mM plates with calcium and the plate without calcium were sampled in time over 30 hours. The other 1250 mM plate with calcium was allowed to react over multiple days until achieving full reaction completion. Normalized urea concentrations in time are presented in Figure 3.4 along with urea degradation trends as estimated by the PHREEQC model for the estimated applied cell density. In this comparison, the 1250 mM urea plate with no calcium closely followed the predicted rate from the PHREEQC model. However, in both plates with added calcium, ureolysis proceeded at a much slower rate (initial rate was ~60% of that observed without added calcium). The dramatic reduction in ureolysis rates with added calcium, suggest that precipitation effects may play a critical role in reducing ureolytic rates during MICP particularly when high chemical concentrations near 1250 mM are applied. It should be noted that this experiment did not entirely control for potential inhibition of ureolysis resulting from increases in solution ionic strengths and calcium concentration changes. However, the fact that the 1250 mM experiment without calcium did not show any detectable rate inhibition in time as high concentrations of ammonium were produced suggests that ionic strength effects alone are unlikely to fully account for the significant inhibition observed in the calcium containing experiments. Although not discussed here, additional experiments were completed wherein sodium concentrations were varied to examine potential inhibition of ureolysis by increases in ionic strength. While some small reductions in rate were observed as sodium concentrations approached 1000 mM, these reductions in ureolytic rates were considerably smaller than those observed in these calcium containing experiments. One remaining possibility is that calcium ions, in particular, may inhibit cell functions at concentrations near 1250 mM. This mechanism is experimentally difficult to isolate, as the addition of calcium would also be expected to result in precipitation. Nevertheless, continued experimentation will be completed to investigate this potential factor.

While acknowledging the above experimental limitations, the additional plate experiments conducted supported the hypothesis that the mechanism responsible for the large reductions in ureolytic rates at high chemical concentrations may likely be related to the formation of increased magnitudes of calcium carbonate precipitation. Increased precipitation may have decreased the ability of ureolytic cells to contribute to bulk ureolysis rates through cell encapsulation, diffusion limitations, and cell death. Furthermore, when high concentrations of calcium and urea are used, higher augmented cell densities and/or the addition of growth factors to treatment solutions may be required to maintain similar rates of ureolysis during MICP reactions. The results of these experiments also suggest that the assumption of a stationary cell density may be inadequate for accurate modelling of urea degradation trends in time when significant calcium carbonate precipitation occurs.

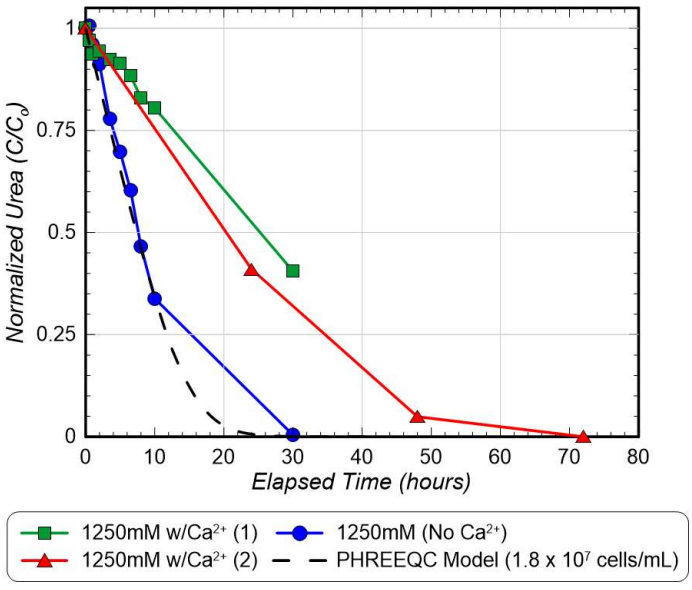

Figure 3.4 Normalized concentrations of urea in time for 1250 mM experiments containing either 1250 mM calcium or no calcium with expected urea degradation trends modelled using PHREEQC.

3.1.2 *Precipitation Effects*

Following all concentration varied experiments, XRD analyses were performed to examine potential differences in precipitate mineralogy. Figure 3.5 presents the mineralogical composition of $CaCO_3$ precipitates resulting from concentration varied experiments as determined by S-Q analysis of the XRD diffraction patterns. As shown, "control" percentages are included (dashed lines), which represent expected mineral compositions for all control specimens as determined by averaging mineral percentages across all control experiments conducted in this study. Results from the 50 mM experiment are not presented as the amount of calcium carbonate precipitated was too small in relation to the parent soil minerals to be able to accurately identify small quantities of vaterite or aragonite, although obtained results did suggest the presence of some calcite. In all three of the other experiments, calcite was found to be the dominant mineral phase, with over 90% obtained for both the 250 mM and 500 mM experiments. For the 1250 mM sample, however, a dramatic decrease in calcite percentage (75%) and increase in vaterite percentage (23%) (detected by the strong peak at a 2θ value of 32.8º) was observed.

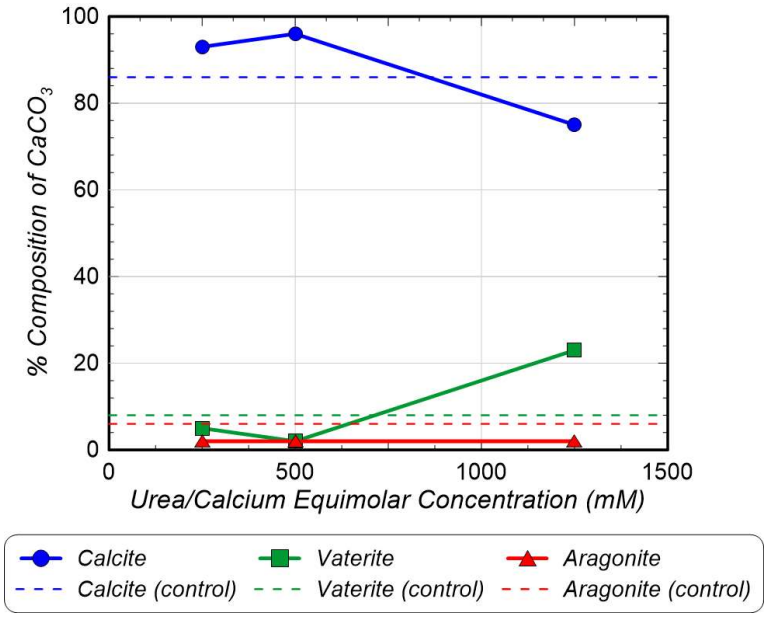

Figure 3.5 XRD results showing relative $CaCO_3$ mineral content percentages for concentration varied experiments.

One hypothesized explanation for the presence of vaterite in the 1250 mM experiment was that vaterite may exist as an intermediate mineral phase during the MICP process, with transformation into calcite minerals occurring via dissolution and re-precipitation events near the end of experiments when lower calcium and carbonate concentrations are present. At these lower concentrations of calcium and carbonate ions (low IAP), solutions can remain super-saturated relative to calcite, which has a lower solubility (K_{sp}), but can be under-saturated relative to vaterite, which has a higher solubility, thus inducing vaterite dissolution. This mechanism is commonly referred to as Ostwald ripening and is a thermodynamically-driven process that occurs because lower solubility minerals more energetically favored than higher solubility minerals (Ratke, Voorhees, 2002). Similar vaterite to calcite transformations have been observed in abiotic calcium carbonate precipitation experiments (Ogino et al., 1990). At standard temperature and pressure, deviations from rhombohedral calcite involving the presence of other calcium carbonate

polymorphs and morphologies are typically associated with biogenic calcium carbonate formation, although such occurrences have also been observed for select inorganic conditions (Zhou et al., 2010). Due to a much slower ureolysis rate than expected, the initial 1250 mM experiment was terminated before all of the supplied urea and calcium could be consumed. This may have allowed solutions to maintain higher IAP values, thus remaining super-saturated relative to vaterite at the end of the experiment and possibly leaving vaterite minerals in obtained samples which would have dissolved and re-precipitated to form calcite had lower calcium and carbonate concentrations (lower IAP values) been achieved.

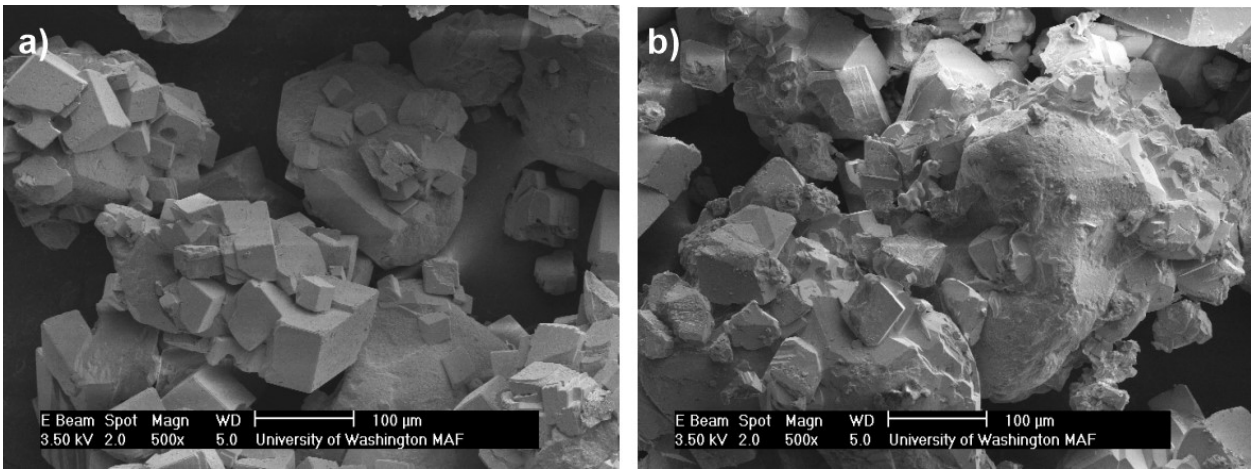

Figure 3.6 Representative SEM images of (a) 250 mM and (d) 1250 mM end-state precipitate samples from concentration varied experiments. It should be mentioned that the 1250 mM sample did not react to completion.

Figure 3.6 presents SEM images used to visually inspect the morphology of end-state precipitates from the 250 mM and 1250 mM experiments. Images of precipitates formed in the 250 mM sample generally demonstrate well-defined, cubic forms that were consistent with the crystalline structure of calcite. As expected, images of the 1250 mM concentration precipitates

showed larger crystals and more precipitation of the surface of sand particles. While most crystal forms found in the 1250 mM sample appeared to be consistent with the rhombohedral form expected for calcite, the morphology of many of these precipitates did not exhibit the sharp, well-defined edges visible in the 250 mM concentration precipitates. Additionally, many of these vaguely rhombohedral forms appeared to be only partially-formed or somewhat distorted in appearance.

Despite XRD analyses suggesting that significant quantities of vaterite were present in the 1250 mM concentration sample, surprisingly SEM imaging revealed no obvious spherical crystal morphologies that would be consistent with vaterite. In both the 250 mM and 1250 mM concentration experiments, however, crystal morphologies with circular-shaped voids were observed in some instances. Past studies have shown that during Oswald ripening dissolution and re-precipitation processes, calcite crystal can develop and grow while being attached to dissolved vaterite spheres, leaving calcite crystals with "vaterite-like casts" (Rodriquez, Shaw, Benning 2010) or spherical voids. Figure 3.7 shows three images of calcite crystals with altered morphologies consistent with "vaterite casts", which are hypothesized to have resulted from this vaterite to calcite transformation process. The apparent lack of vaterite visible in the SEM images obtained for the 1250 mM sample may be explained by storage of the end-state sample for some time in a faulty desiccator at higher than desirable relative humidity. This desiccator was subsequently replaced prior to SEM imaging. The presence of some moisture in this sample during storage may have allowed for the ripening process to proceed even after the experiment was terminated.

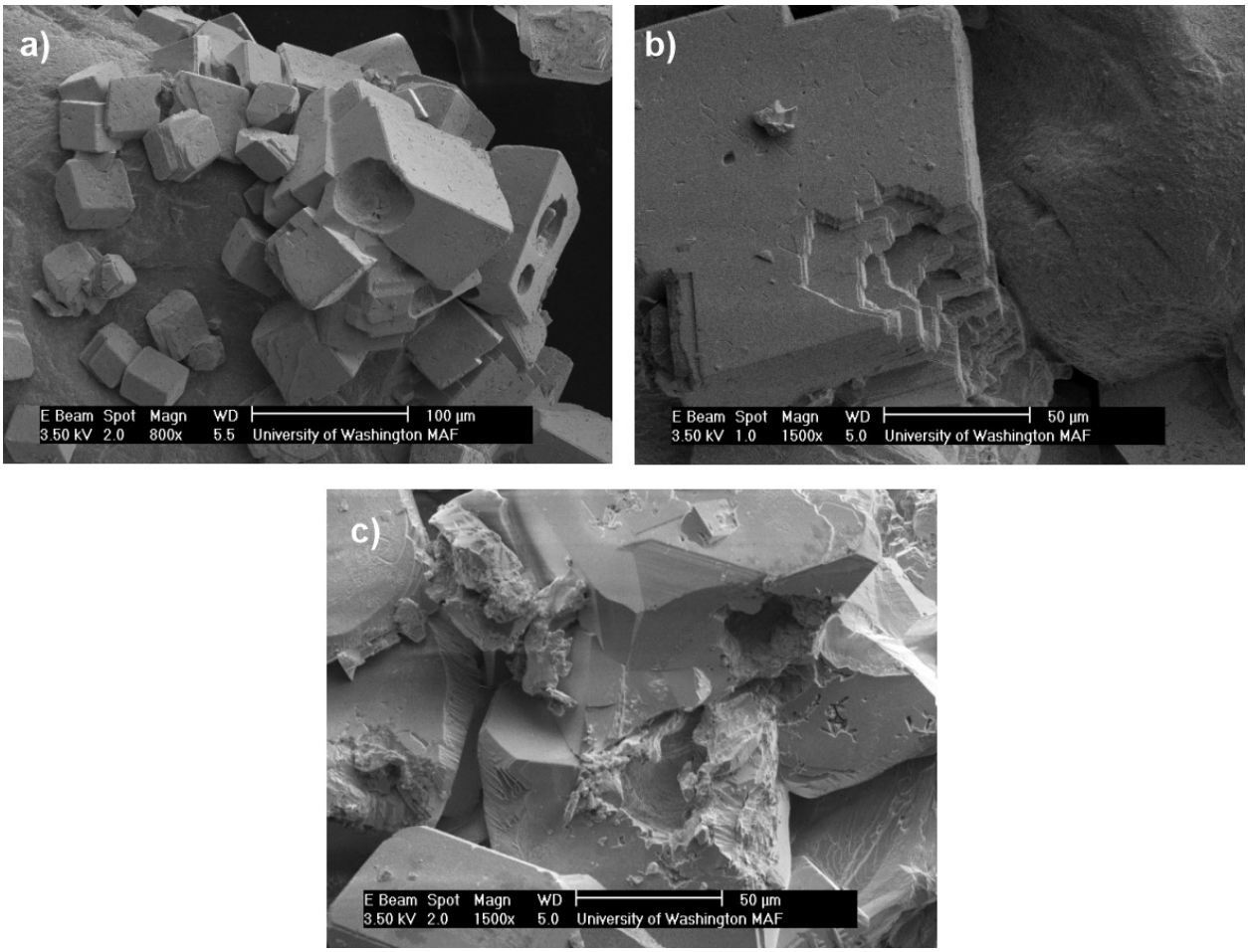

Figure 3.7 Representative SEM images of "vaterite casts" observed in (a,b) 250 mM and (c) 1250 mM concentration experiments.

3.1.3 *Temporal Effects*

In order to further investigate the potential role of Ostwald ripening processes on the mineralogy and morphology of precipitates over time, another experiment was designed wherein the 1250 mM urea with calcium concentration experiment was repeated side by side in four identical plates that were stopped at various points in time during the MICP process. This experiment was intended to examine potential changes in the relative mineral compositions in time during the MICP process by terminating ureolysis and collecting precipitate samples at various times. Figure 3.8 presents normalized concentrations of urea in time for the four plate

experiments. As shown, similar urea degradation in time was observed for all experiments. At different times corresponding to roughly 5%, 25%, 60%, and 100% degradation of the applied urea, experiments were terminated, soil and precipitate samples were rinsed twice in ethanol, and samples were stored immediately in a desiccator with a relative humidity of less than 10%.

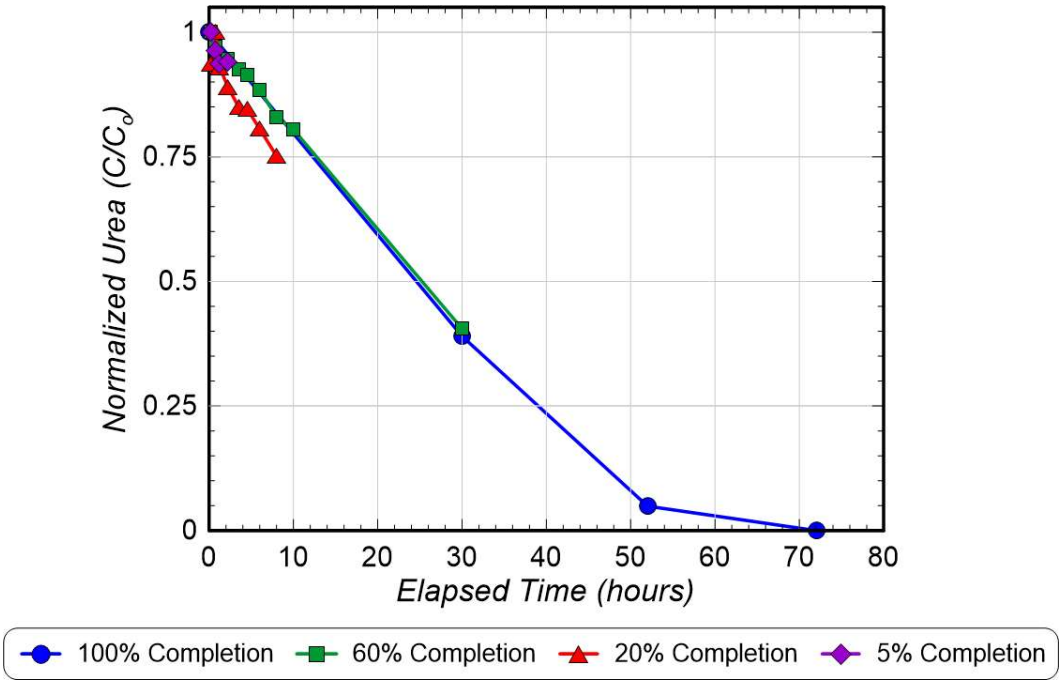

Figure 3.8 Normalized concentrations of urea in time for 1250 mM concentration experiments stopped at various percentages of reaction completion.

Figure 3.9 presents S-Q analysis results for the diffraction patterns obtained following XRD analysis of all 1250 mM experiments stopped at various points in time. As shown, the relative percentages of calcite and vaterite appeared to be coupled in time, with calcite percentages decreasing at first and then increasing as ureolysis proceeded towards reaction completion. Vaterite percentages followed the opposite trend, increasing at first and then decreasing in time as ureolysis proceeded toward completion. These results supported the hypothesis that a dissolution and re-precipitation process like Ostwald ripening may have indeed affected mineral compositions

over time, particularly when reactions are stopped before completion. These results also suggest that relative percentages of different calcium carbonate polymorphs may converge over time towards a relatively consistent end state, at least for the relatively simple conditions tested in this experiment involving deionized water based solutions, rinsed and pelleted bacterial inoculants, equal concentrations of urea and calcium, and no other chemical additions.

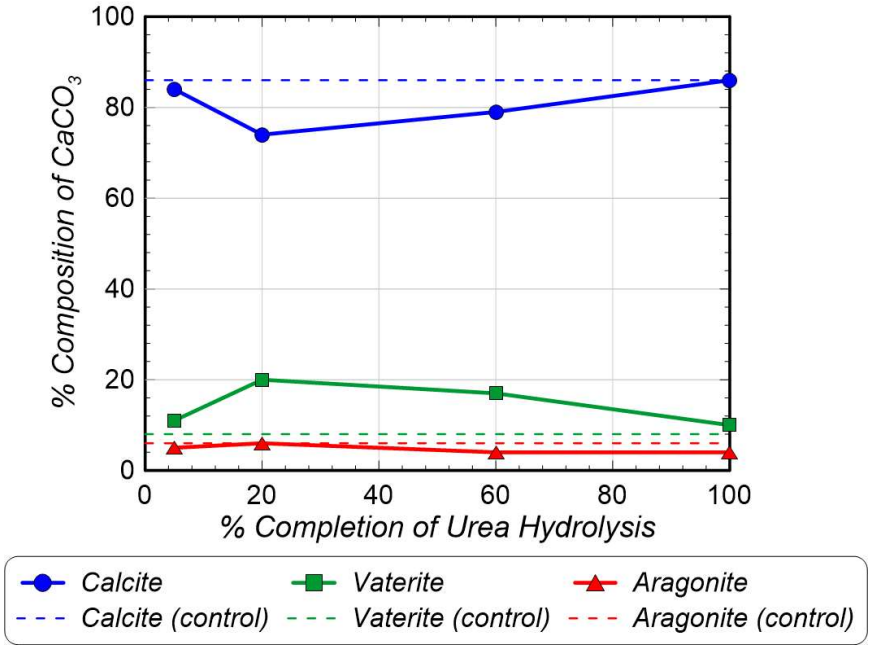

Figure 3.9 S-Q analysis of XRD results show temporal changes in $CaCO_3$ mineral percentages during MICP reactions for 1250 mM urea and calcium experiments.

Figure 3.10 presents SEM images of the precipitate samples obtained at various points in time during reactions and support the findings of these XRD analyses. Spherical crystalline forms typically associated with vaterite are immediately visible in the images of the 5% reaction completion experiment precipitates (Figure 3.10a). Spherical forms become even more abundant in the images of precipitates from the 20% (Figure 3.10b) and 60% (Figure 3.10c) reaction completion experiments. In comparison to the 5% and 20% reaction completion samples, a number

of spherical forms in the 60% reaction completion sample appear to be less spherical in shape, and some were even observed on the surfaces of cubic calcite crystals in what appeared to be an ongoing dissolution-reprecipitation event (Figure 3.11). In the sample that was allowed to proceed to achieve 100% reaction completion, spherical forms were no longer visible. The remaining crystal forms appeared to be generally rhombohedral in shape (Figure 3.10d). However, as shown in Figure 3.12b, many of these rhombohedral forms showed significant defects or damage to their typical morphology when examined under higher magnifications. Additionally, some precipitates appeared to have more chaotic crystalline or amorphous morphologies (Figure 3.12a). While these forms were dramatically different with respect to crystal angularity, surface area, and distribution, they did not change the resulting XRD spectra, which suggested that end-state precipitates contained predominantly calcite. As such, it is suspected that bio-cemented materials synthesized using high urea and calcium concentrations may display noticeably different engineering properties, such as dissolution resilience, when compared to precipitates formed using lower urea and calcium concentrations, despite having near equivalent mineralogy as determined by XRD. Further analysis of such precipitates may allow for better understanding and quantification of these seemingly amorphous calcium carbonate mineral phases.

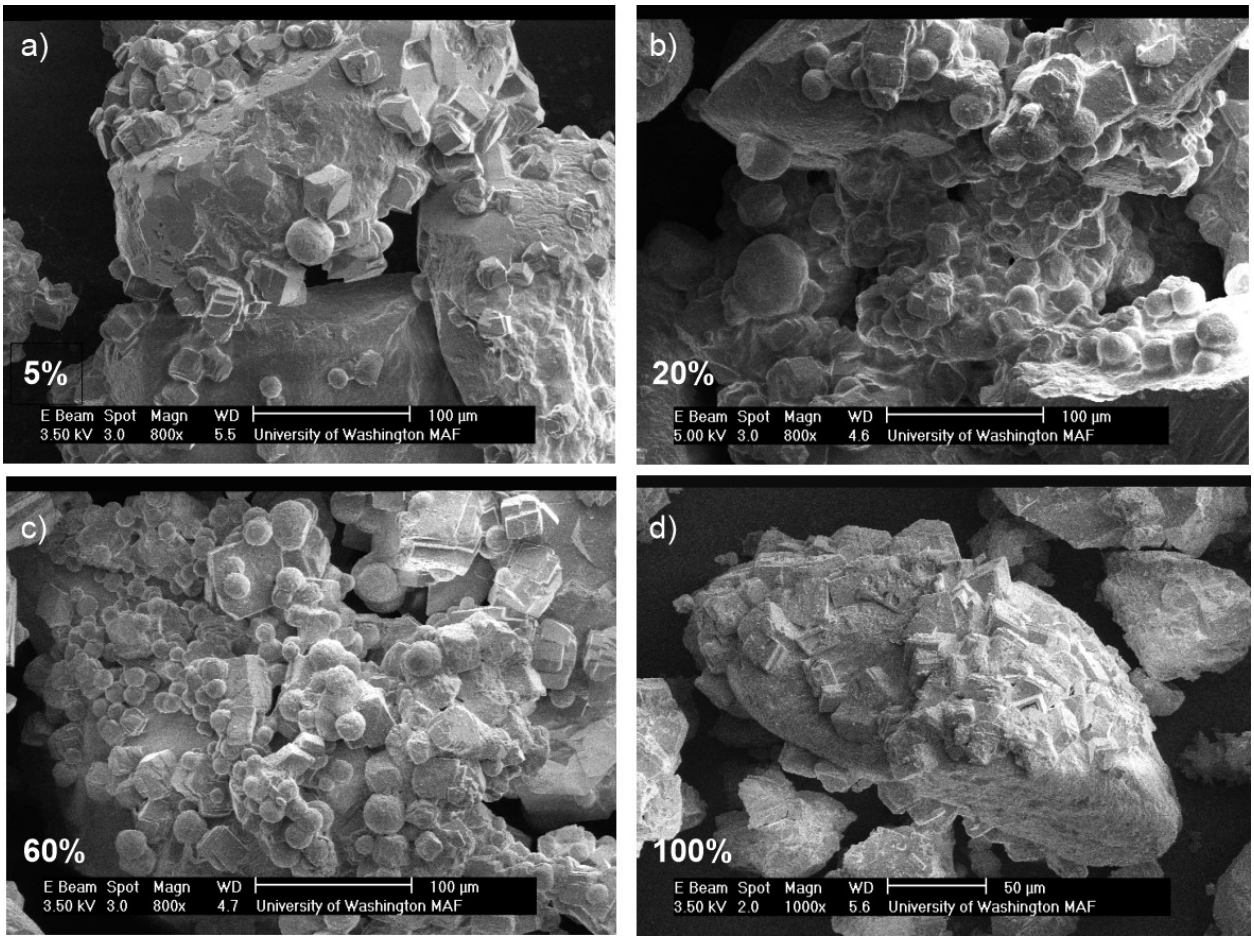

Figure 3.10 Representative SEM images of end-state precipitates from 1250 mM concentration experiments wherein ureolysis was stopped at (a) 5%, (b) 20%, (c) 60%, and (d) 100% reaction completion.

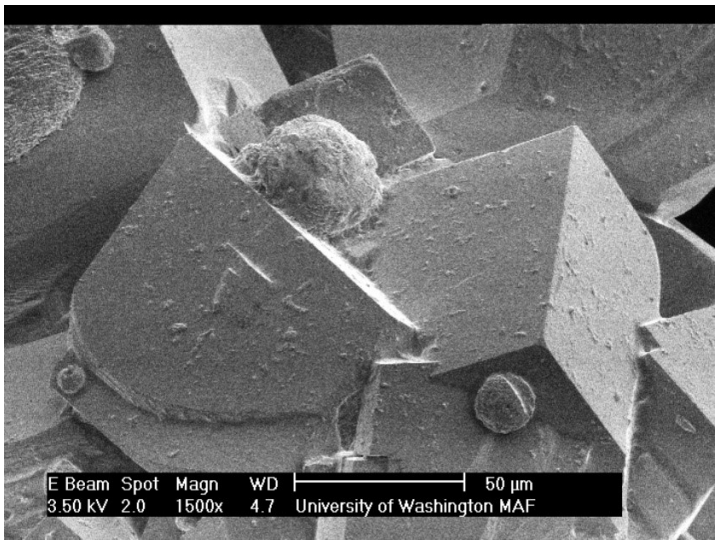

Figure 3.11 SEM image (1500x magnification) of a spherical vaterite crystal that appears to be dissolving on the surface of rhombohedral calcite crystal in the 1250 mM experiment at 60% reaction completion.

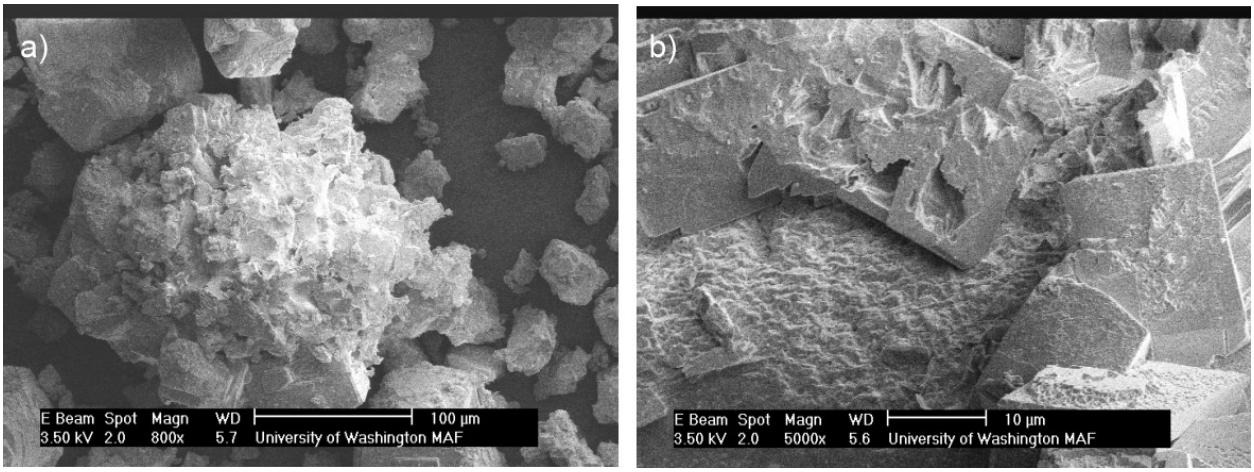

Figure 3.12 Representative SEM images of end-state precipitates from the 1250 mM concentration experiment achieving 100% reaction completion. Prominent crystal forms are rhombohedral in shape but can be (a) chaotic or amorphous in appearance (seen at 800x magnification) and have some (b) surface defects (seen at 5000x magnification).

3.2 Urea and Calcium Ratios

Although most experiments completed in this study involved urea-to-calcium concentration ratios of 1, past studies have used a wide range of urea-to-calcium ratios with some studies even exceeding ratios of 6 (Montoya 2015). When MICP reactions are allowed to proceed to completion, only minor increases in calcium carbonate precipitation can be obtained when supplied urea exceeds concentrations of supplied calcium. Despite this, researchers adding higher concentrations of urea may do so to ensure that injected calcium concentrations are fully consumed during the treatment process even if reductions in ureolytic activity occur.

In order to examine the effect of different urea-to-calcium concentration ratios and magnitudes on the MICP process, six plate experiments were performed. Plates received cementation solutions prepared at urea-to-calcium ratios of either 0.5, 1, or 5 and contained either calcium concentrations of 250 mM or 500 mM. Similar calcium concentrations between experiments receiving different ratios was intended to keep magnitudes of resulting precipitation similar between experiments. All experiments were inoculated with *S. pasteurii* cells at a total cell density of 7.68×10^7 cells/mL estimated from OD_{600} measurements.

Figure 3.13 presents normalized concentrations of urea and calcium in time for all urea-to-calcium ratio experiments. Figure 3.14 shows similar normalized concentrations of urea in time for each of the urea-to-calcium ratio experiments along with PHREEQC modelled trends that were calibrated to the observed urea degradation trends assuming a constant cell density. For the 250 mM experiments with urea-to-calcium ratios of 0.5 (Figure 3.14a) and 1 (Figure 3.14b), and the 500 mM experiment with a urea-to-calcium ratio of 0.5 (Figure 3.14d), experimentally observed urea degradation trends match well with models that assumed cell densities of approximately 1.0×10^7 cells/mL. For the 500 mM experiment with a urea-to-calcium ratio of 1 (Figure 3.14e), a

moderate reduction in ureolytic activity was observed with the modelled cell density being approximately 6.0 x 10^6 cells/mL (40% lower). More dramatic reductions in ureolytic activity were observed in the 250 mM (Figure 3.14c) and 500 mM (Figure 3.14f) experiments with a urea-to-calcium ratio of 5 wherein the modelled cell density was approximately 4.0 x 10^6 cells/mL (60% lower). These results were consistent with previous observations from concentration varied experiments, wherein ureolytic rates were slower at urea concentrations exceeding 500 mM when compared to the 250 mM control condition. More dramatic inhibition observed in the highest urea-to-calcium ratio experiments suggest that higher urea concentrations (>1250 mM) may even further inhibit ureolytic rates.

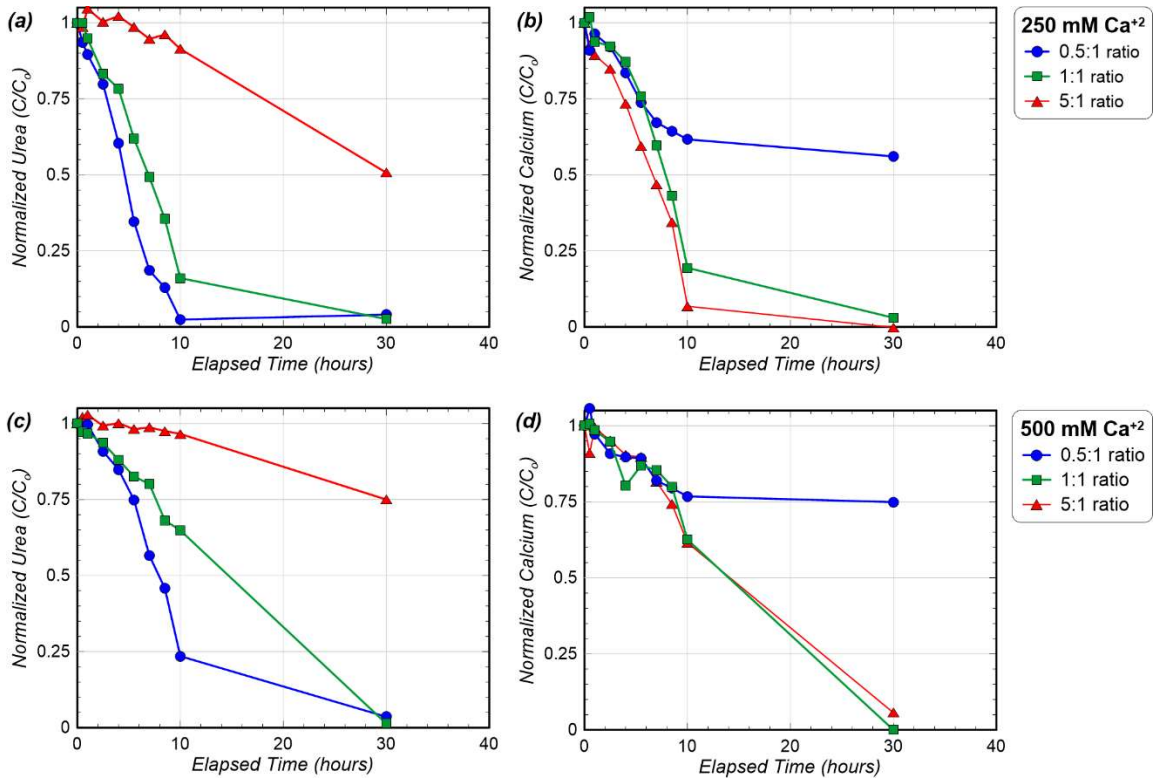

Figure 3.13 Normalized concentrations of (a,c) urea and (b,d) calcium in time measured during urea-to-calcium ratio experiments with calcium concentrations of (a,b) 250 mM and (c,d) 500 mM and varying urea-to-calcium ratios.

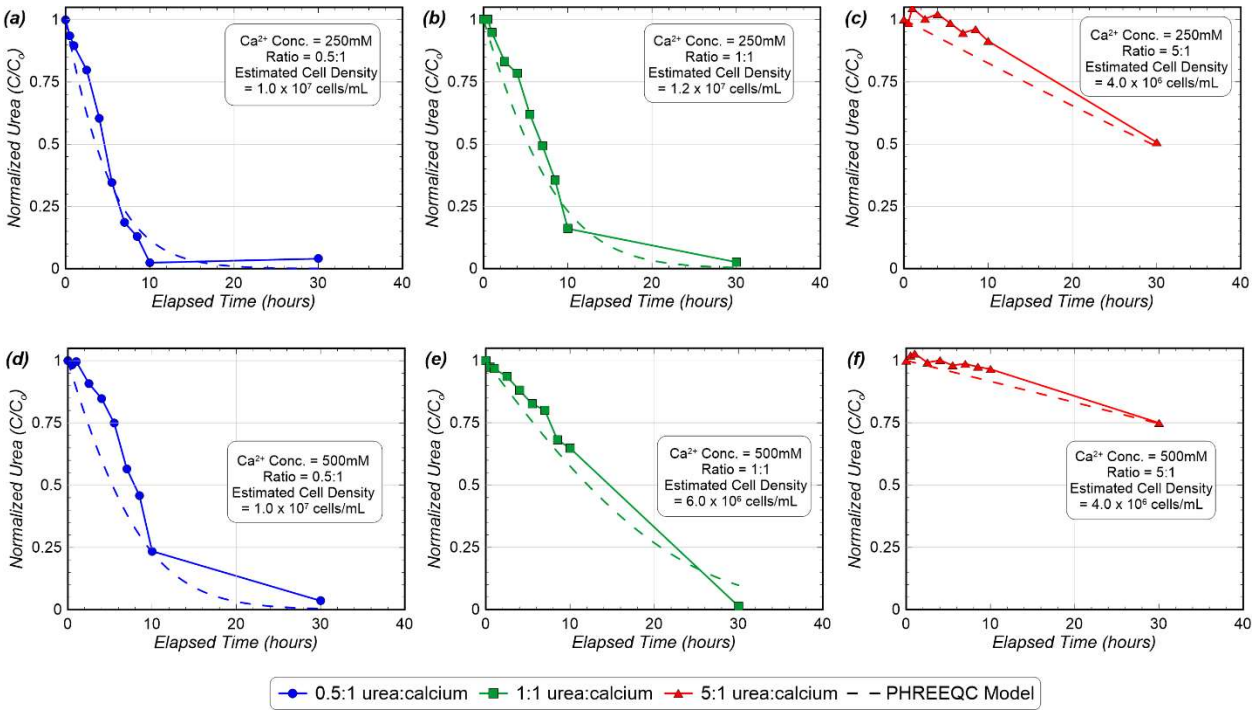

Figure 3.14 Normalized concentrations of urea in time for urea-to-calcium ratio experiments with calcium concentrations of either (a,b,c) 250 mM or (d,e,f) 500 mM and varying urea-to-calcium ratios. Urea degradation trends predicted using the PHREEQC model are presented and correspond to reported cell densities in text blocks.

Figure 3.15 presents the results of the S-Q analysis for the XRD diffraction patterns obtained for all end-state precipitates from the urea-to-calcium ratio experiments. For all three urea-to-calcium ratios and both calcium concentrations, calcite was found to be the dominant mineral phase, with generally higher calcite and lower vaterite abundances in 250 mM calcium experiments when compared to 500 mM calcium experiments. When looking at variations between specimens with different urea-to-calcium ratios only minor trends in relative mineral compositions were observed, with generally higher calcite percentages observed at lower urea-to-calcium ratios.

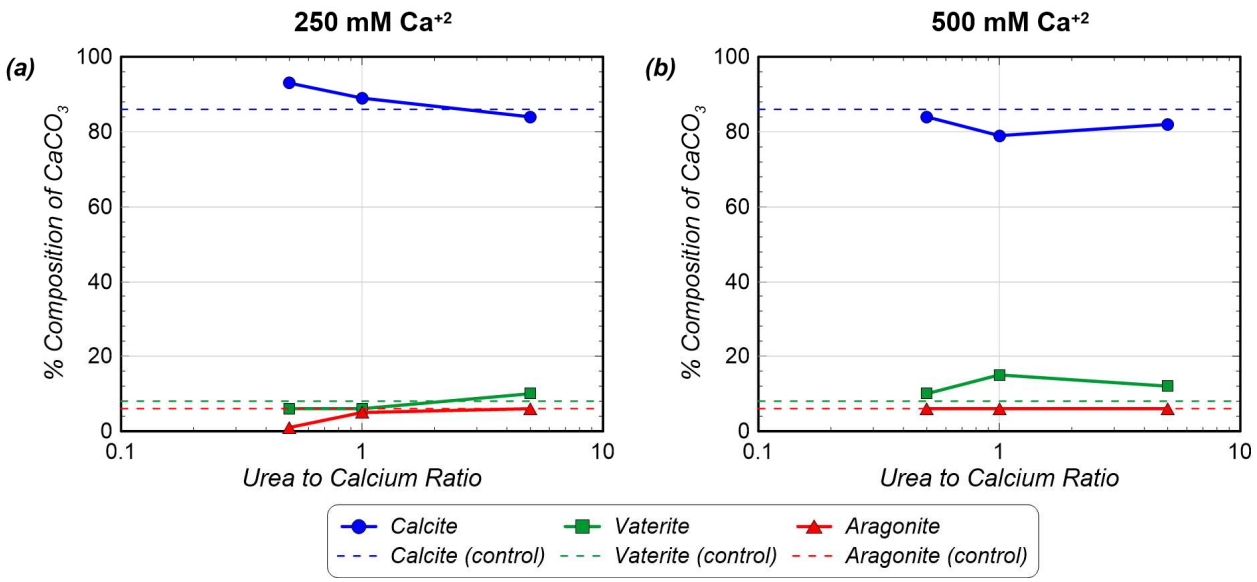

Figure 3.15 XRD results showing relative $CaCO_3$ mineral content percentages for urea-to-calcium ratio experiments with either (a) 250 mM or (b) 500 mM calcium at varying urea-to-calcium ratios.

Figure 3.16 presents SEM images of the urea-to-calcium ratio varied experiments with 500 mM calcium. These images generally supported the findings of the XRD analyses, with no significant changes in crystal morphology, size, or distribution observed between end-state precipitates with urea-to-calcium ratios of 5 (Figure 3.16a), 1 (Figure 3.16b), and 0.5 (Figure 3.16c).

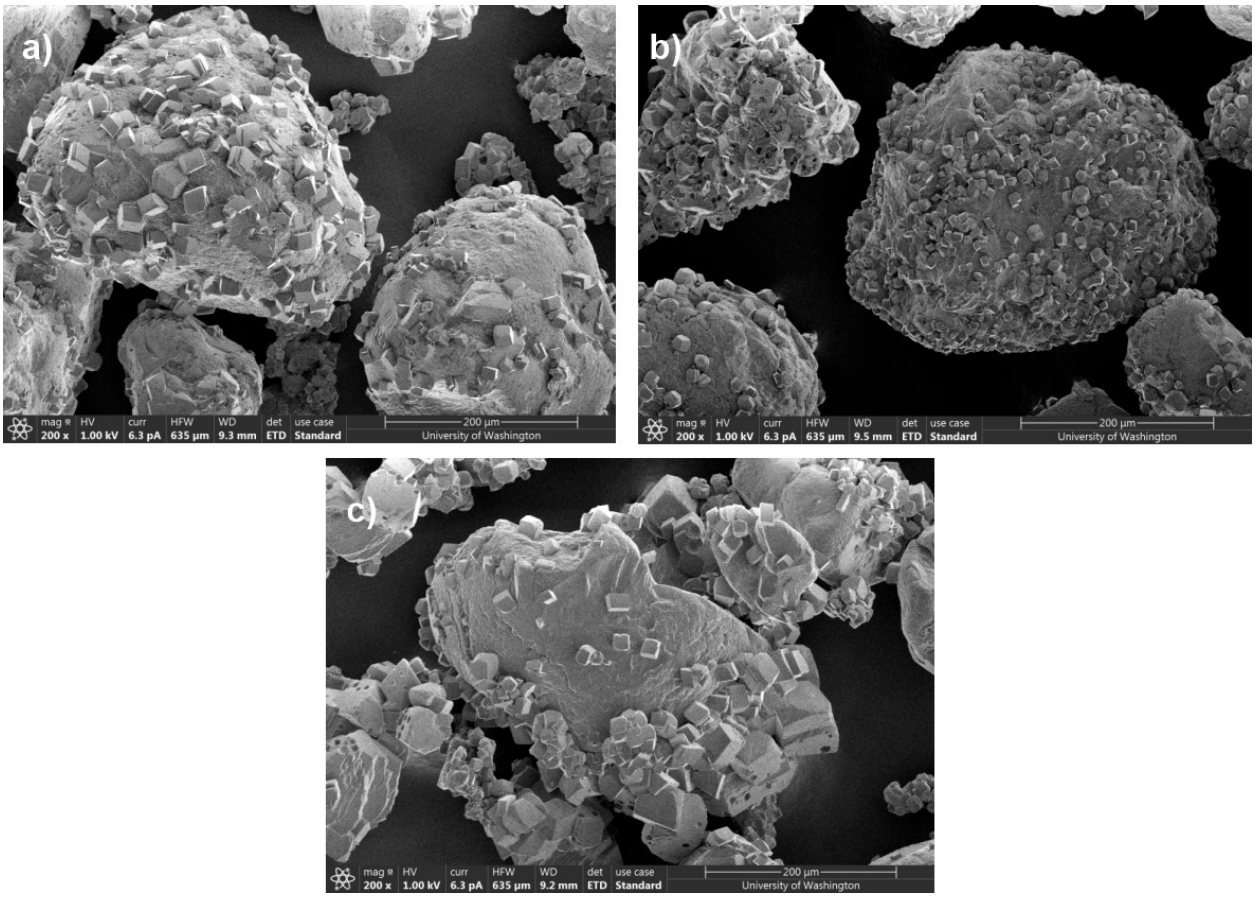

Figure 3.16 Representative SEM images of end-state precipitate samples from experiments with urea-to-calcium ratios of (a) 5, (b) 1, and (c) 0.5 with 500 mM calcium.

3.3 Initial Solution pH

When MICP is applied to different project sites, a wide range of groundwater and site water chemistries and initial solution pH values may be encountered. In order to examine the effect of initial solution pH on the MICP process, three plate experiments were performed. Cementation solutions were prepared to initial solution pH values intended to reflect relatively acidic (pH = 5), neutral (pH = 7), or alkaline (pH = 9) initial conditions. All solutions were prepared by adding 250 mM urea and calcium chloride dihydrate to deionized water. Following this, solution pH was adjusted by adding either 1 M hydrochloric acid (HCl, Fisher Scientific) or 1 M sodium hydroxide

(NaOH, prepared with from sodium hydroxide pellets, Fisher Scientific, 98.9% assay) in order to decrease or increase pH, respectively. Solution pH was verified using a glass-body pH electrode probe with +/- 0.01 pH unit accuracy.

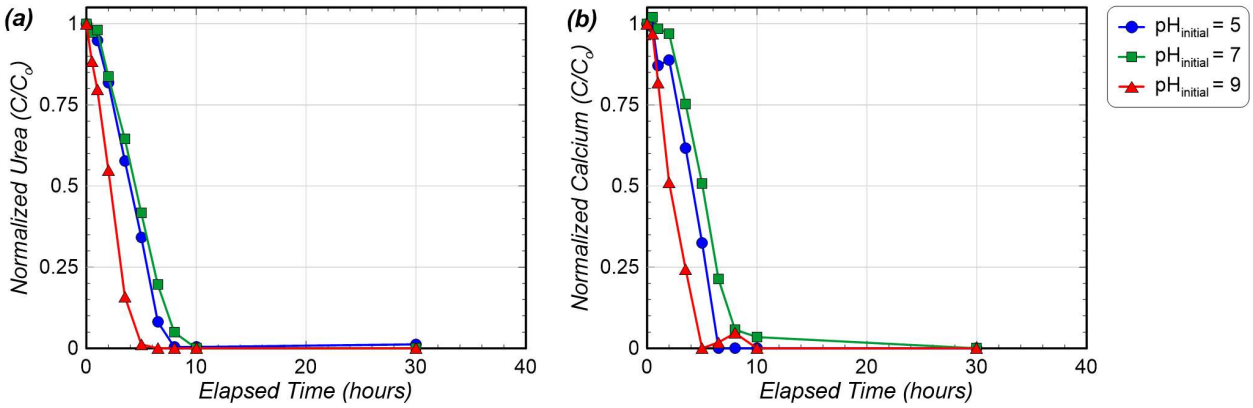

Figure 3.17 Normalized concentrations of (a) urea and (b) calcium in time measured during initial pH varied experiments.

Figure 3.17 presents normalized concentrations of urea and calcium in time for the all initial pH varied experiments. All experiments were inoculated with *S. pasteurii* at a total cell density of 7.6 x 10^7 cells/mL. Although experiments with an initial pH of 5 and 7 showed similar urea degradation trends, the initial pH of 9 experiment exhibited a considerably faster ureolytic rate. Although this increase in urea degradation rate at a more alkaline initial pH was unexpected, the activity of both free urease enzymes (Stocks-Fischer et al. 1999) and whole cell urease (Whiffin 2004) have been observed to exhibit pH-dependent activities. These past studies have suggested that free urease may exhibit an optimum rate near a pH of 8.5 with whole cell urease generally showing only a minor pH dependency when pH values are between 6 and 8.5. While these past results do not fully explain observations in the experiment with an initial pH of 9, they do suggest that the pH dependency of urease enzyme activity and other ureolytic cellular processes may play

some role. In addition, although a small lag in urea hydrolysis activity was commonly observed during the first 30 to 60 minutes of most plate experiments conducted in this research, in the initial pH of 9 experiment, no such lag was observed. While the exact mechanisms responsible for both urea degradation rate increases and the notable absence of a lag in ureolysis at the start of the experiment were not investigated further, these observations do suggest that high initial pH may favor increased initial ureolytic activity.

Figure 3.18 presents the results of the S-Q analysis for the XRD diffraction patterns obtained for all end-state precipitates from the initial pH varied experiments. In all three experiments, calcite was found to be the dominant mineral phase at 86%, with vaterite and aragonite present at 8% and 6%, respectively. The relative composition of $CaCO_3$ minerals was consistent for all three plate experiments, suggesting that the initial pH of the cementation solution did not have discernable effects on the mineralogy of the calcium carbonate minerals precipitated during MICP. SEM images shown in Figure 3.19 support this conclusion, as all precipitates appeared to have well-defined, rhombohedral morphologies that were consistent with the crystal structures expected for calcite. No prominent differences were observed even between SEM images of the lowest (pH = 5) and highest (pH = 9) initial pH specimens. The results of these experiments suggest that the initial pH of applied cementation solutions has a minimal, if any, effect on the MICP process when solutions are adjusted with HCl and/or NaOH, pH values are between 5 and 9, and the buffering capacity of solutions is relatively small. It should be noted, however, that differences in results may have occurred if more strongly buffered solutions had been used.

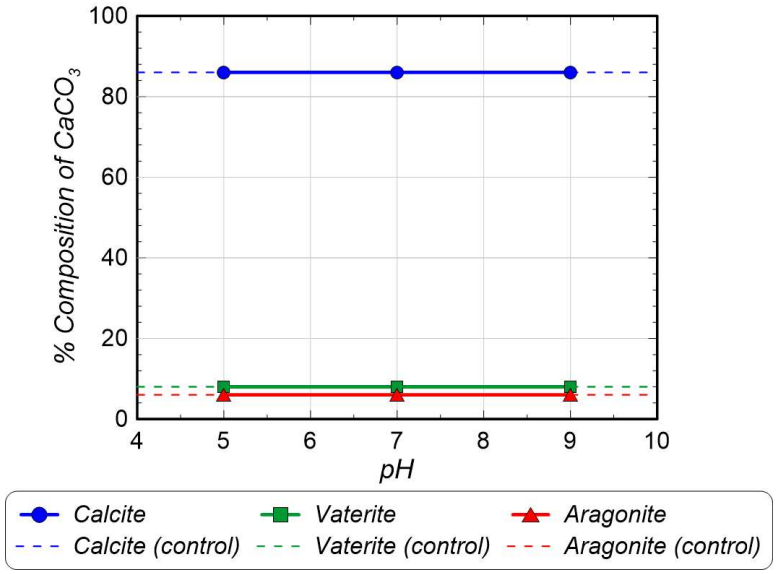

Figure 3.18 Relative $CaCO_3$ mineral content percentages for pH varied experiments determined from XRD analyses.

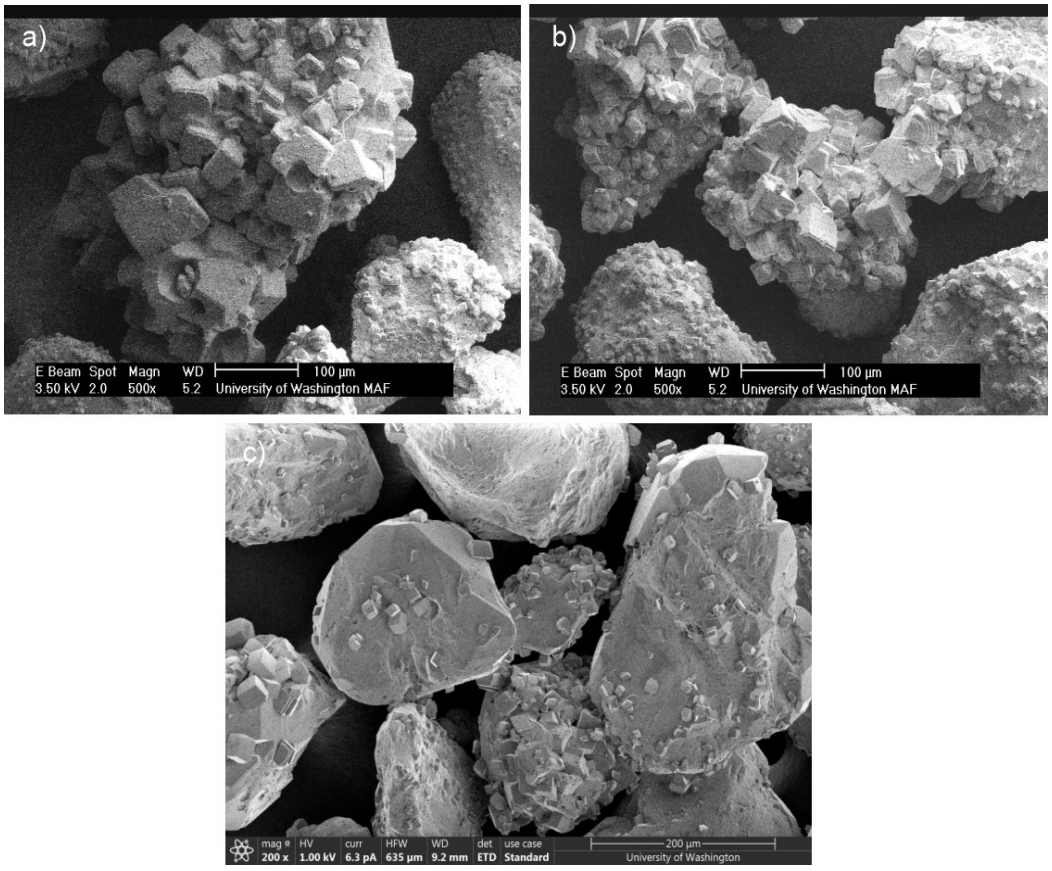

Figure 3.19 Representative SEM images of end-state precipitate samples from experiments with initial pH values of (a) 5, (b) 9, and (c) 7.

3.4 SYNTHETIC SEAWATER MIXTURES

MICP has been proposed for a variety of marine applications wherein large changes in surrounding aqueous solution chemistry may be present. Given the high alkalinity and calcium concentrations naturally present in seawater, precipitated bio-cementation may also be expected to remain stable or even build over time in many of these environments. In order to examine the effects of seawater ions on the MICP process, three plate experiments were performed. Two plates contained cementation solutions prepared in artificial seawater at 100% by volume and 50% by volume with de-ionized water to represent marine seawater and brackish environments, respectively. All seawater solutions were prepared using dried sea salts (Sigma-Aldrich) added to de-ionized water at 38 g/L for 100% seawater and 19 g/L for 50% seawater. Dried salts were formulated to recreate the typical natural ion composition of seawater including various trace ions and contained less than 0.05% insoluble matter. Ion concentrations present in the artificial seawater as specified by the manufacturer are provided in Table 3.2. All cementation solutions were prepared by adding 250 mM urea and calcium chloride dihydrate to these seawater mixtures.

Table 3.2. Ion Composition of 100% Artificial Seawater

Ion	**Concentration (mM)**
Chloride (Cl^-)	536
Sodium (Na^+)	478
Magnesium (Mg^{+2})	54
Sulfate (SO_4^{-2})	27
Calcium (Ca^{+2})	10
Potassium (K^+)	5
Carbonate (CO_3^{-2})	3
Strontium (Sr^{+2})	0.5
Boron (B^{+3})	0.03

3.4.1 *Ureolytic Rate Effects*

Figure 3.20 presents the normalized concentrations of urea and calcium in time for all seawater concentration experiments. All experiments were inoculated with *S. pasteurii* at a total cell density of 7.6 x 10^7 cells/mL. As shown, the 50% seawater experiment showed a near negligible decrease in ureolytic rate when compared to the deionized water control. The 100% artificial seawater experiment, in contrast, showed a much more significant reduction in ureolytic rate and had an initial ureolysis rate that was near half of that observed in deionized water. This large reduction in ureolytic rate suggested that increasing concentrations of seawater had an inhibitory effect on urea hydrolysis. It remained unclear, however, what mechanisms were responsible for this ureolytic rate inhibition. Several explanations for the observed rate reductions at higher salinities were hypothesized including potential inhibition of ureolysis by the presence of: (1) high solution ionic strengths, which may interfere with cellular and enzyme activity as well as intercellular diffusion, (2) particular ion species, which may interfere with enzyme functions and cellular processes, and/or (3) additional precipitation events that may have resulted from the presence of other ions and the formation of new minerals phases, thus further decreasing ureolytic activities from cell encapsulation. Although ureolysis did not cease completely in the 100% seawater specimen, the observed 50% decrease in initial ureolytic rate could have important implications for field-scale implementations of augmented MICP if such effects are not anticipated and incorporated into reactive transport models.

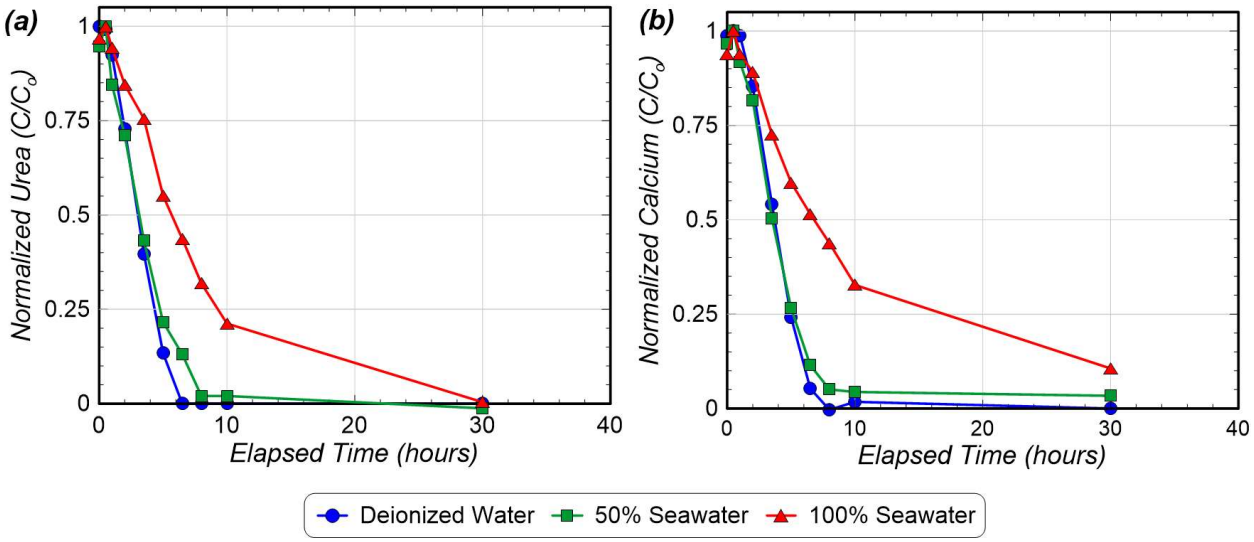

Figure 3.20 Normalized concentrations of (a) urea and (b) calcium in time for deionized water, 50% seawater, and 100% seawater solution experiments.

In order to further investigate and isolate the effect of various ions present in seawater on urea hydrolysis, three ions, magnesium, strontium, and sulfate, were selected for further study. Magnesium and strontium were selected as they are both divalent cations with an ionic charge similar calcium (+2), and thus were suspected to potentially participate and interference with calcium carbonate formation during bio-cementation, possibly via ion substitution. Additionally, numerous past studies have involved the use of MICP as a bio-remediation technique for sequestration and immobilization of strontium at contaminated sites, via co-precipitation (Achal et al., 2012), making its effect on MICP mineralogy and process kinetics a question of practical importance. Sulfate was also selected for investigations due to its high concentration in seawater and its similar charge to carbonate anions (-2). Past studies have examined the effects of sulfate on abiotic $CaCO_3$ precipitation (Reddy and Nancollas 1976), and it was suspected that sulfate ions may potentially interfere with $CaCO_3$ precipitation and participate in the formation of gypsum or calcium sulfate ($CaSO_4$) minerals. The experiment was designed so that each ion was applied at

concentrations corresponding to 50%, 100%, and 200% of their expected concentrations in natural seawater to explore their effects on ureolysis and calcium carbonate precipitation reaction kinetics and end-state minerals. When preparing cementation solutions containing high concentrations of sulfate (>10mM), however, $CaSO_4$ minerals appeared to precipitate abiotically immediately after cementation solutions were prepared. A maximum sulfate concentration of 10 mM was therefore examined in these experiments wherein abiotic precipitation events were minimized. Following these experiments, another series of plate experiments were performed using higher concentrations of sulfate without added calcium, thereby mitigating potential $CaSO_4$ precipitation and allowing the effect of sulfate on microbial ureolysis to be more fully understood. All experiments contained *S. pasteurii* at a cell density of 7.1×10^7 cells/mL and had initial urea and calcium concentrations of 250 mM.

Figure 3.21 presents normalized concentrations of urea and calcium in time for the magnesium, strontium, and sulfate concentration varied experiments. As shown in Figure 3.21a and Figure 3.21b, increases in magnesium concentrations resulted in strong inhibitory effects on observed ureolytic rates. In experiments containing 27 mM and 54 mM magnesium, a roughly 15% decrease in initial ureolytic rate was observed, while the higher 108 mM magnesium experiment exhibited a larger 45% decrease in initial ureolytic rate. While 27 mM and 54 mM magnesium experiments exhibited similar inhibition, increases in magnesium concentrations appeared to significantly decrease ureolytic rates. These results suggest that ureolytic rate decreases may be significant for locations with soils and/or groundwater containing high magnesium concentrations, such as marine environments and karst regions containing dolomite parent rocks. In contrast, when strontium and sulfate concentrations were increased up to concentrations of 0.22 mM and 10 mM, respectively, no significant effects on ureolytic rates were

observed (Figure 3.21c, Figure 3.21d). Figure 3.22 presents the results of the additional experiments that contained higher sulfate concentrations without added calcium along with deionized water and seawater controls. The results suggested that sulfate concentrations near those present in seawater (28 mM) appeared to have no detectable effects on ureolysis. It should be mentioned, however, that these results did not definitively conclude that increased sulfate concentrations will have no effect in the presence of calcium, however, such effects, if any, would likely be related to the presence of $CaSO_4$ precipitation.

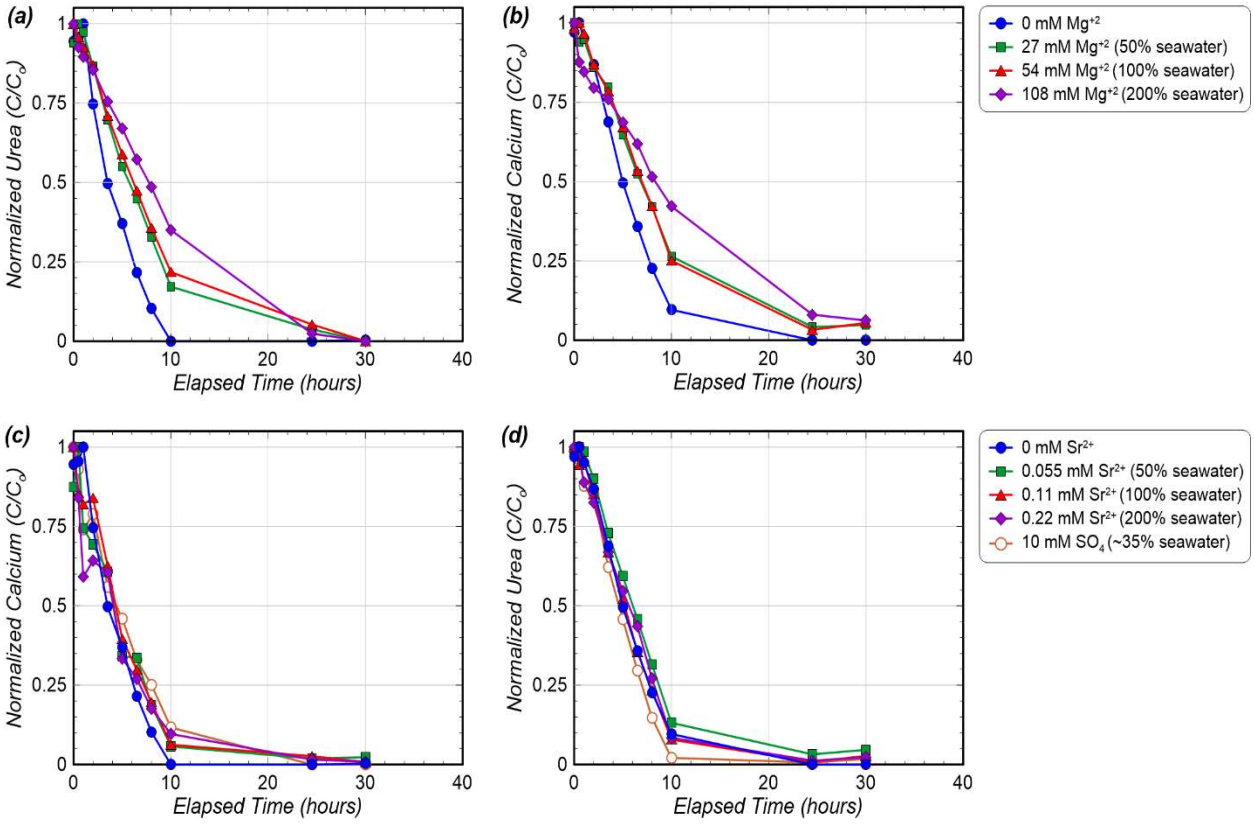

Figure 3.21 Normalized concentrations of (a, c) urea and (b, d) calcium in time for (a, b) magnesium concentration varied experiments and (c, d) strontium and sulfate concentration varied experiments.

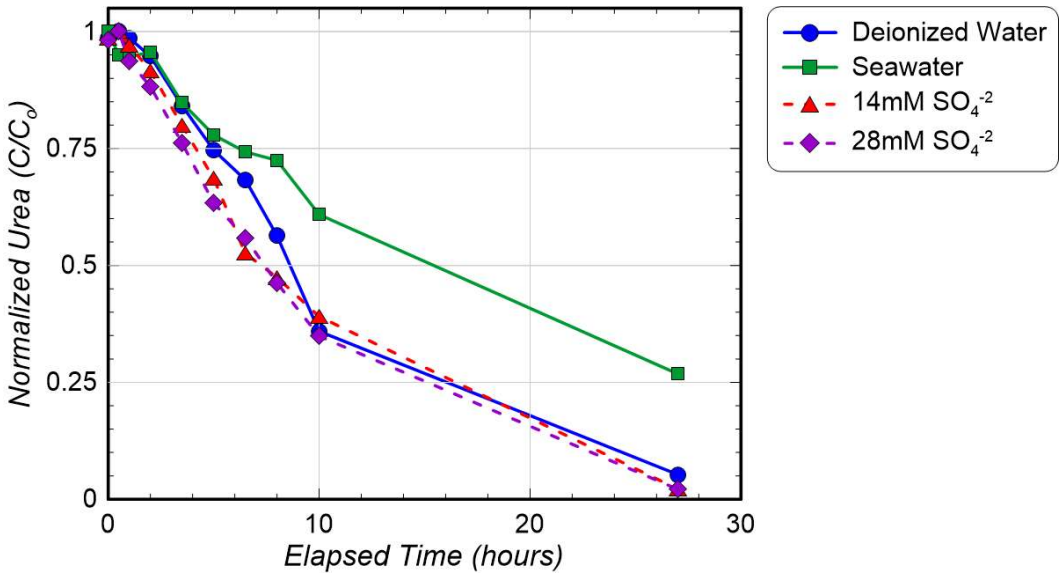

Figure 3.22 Normalized concentrations of urea in time for experiments with varying sulfate concentrations and no added calcium.

While these results suggested that the presence of magnesium can significantly influence ureolytic rates, comparisons between seawater and magnesium concentration varied experiments suggested that magnesium additions alone could not fully account for observed ureolytic rate decreases. Thus, subsequent experiments were performed to better isolate the effect of magnesium on ureolytic rates when compared to seawater. These plates contained minimal added calcium and compared urea hydrolysis activity in artificial seawater and deionized water to other specimens containing deionized water with magnesium concentrations of 54 mM and 108 mM corresponding to concentrations in 100% and 200% seawater, respectively. To better isolate the effects of magnesium changes on microbial ureolysis, all experiments were performed with either no calcium (0 mM) or 10 mM calcium added, which was intended to match the small concentration of calcium present in the artificial seawater. Removing all calcium additions in certain specimens allowed for the removal of any inhibitory effects related to calcium carbonate precipitation therefore isolating the effects of ionic strength changes and magnesium additions on observed ureolytic rates.

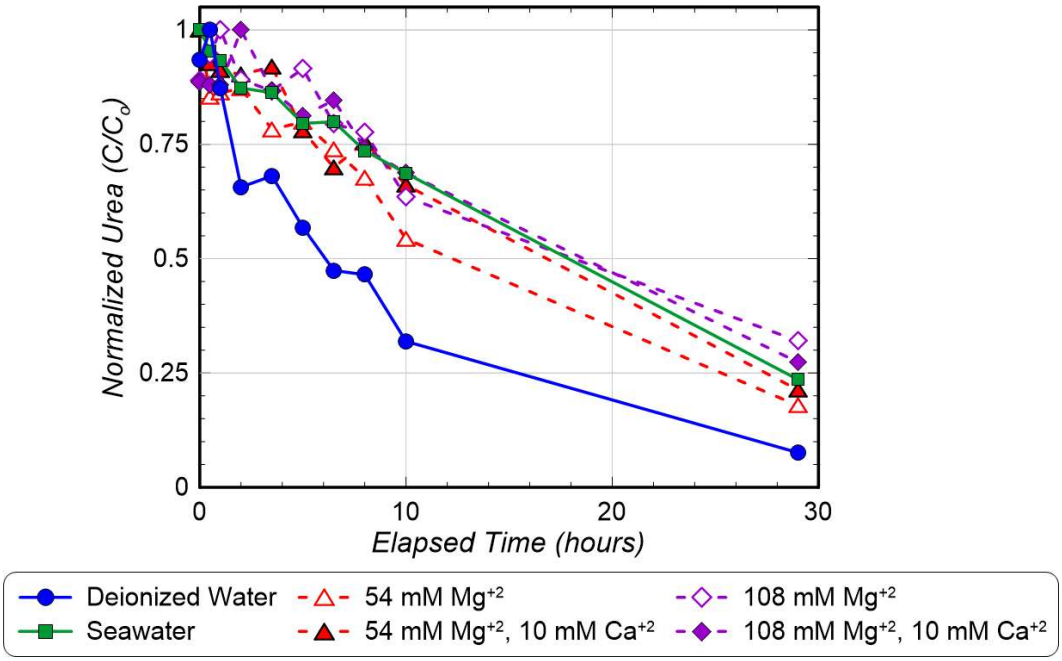

Figure 3.23 Normalized concentrations of urea in time for magnesium concentration varied experiments containing either 10 mM calcium (concentration in 100% seawater) or no calcium added to isolate potential effects on microbial ureolysis. The seawater mixture included 54 mM magnesium and 10 mM calcium.

Figure 3.23 presents normalized concentrations of urea in time for magnesium concentration varied experiments containing either 10 mM calcium or no calcium as well as seawater and de-ionized water control experiments. These results suggest that increases in magnesium concentrations can result in decreases in ureolytic rates even when calcium is not present, further supporting the findings of the previous experiment. Additionally, when comparing the 54 mM magnesium experiment to the artificial seawater experiment, it appears that approximately 80% of the ureolytic rate reduction observed in the artificial seawater can likely be primarily attributed to changes in magnesium ion concentrations. Despite this, the results also suggest that other factors may contribute at least marginally to the observed rate decreases.

3.4.2 *Precipitation Effects*

Figure 3.24 presents the results of the S-Q analysis for the XRD diffraction patterns obtained for end-state precipitates from the previous seawater experiments. As shown, calcite was the dominant mineral phase in all experiments, with slight decreases (≈6%) in calcite relative percentages as seawater concentrations increased. Aragonite relative percentages in turn increased from 6% to 13% as salinity increased from the deionized water control to 100% seawater. The XRD results also showed a slight shift [up to $2\theta = 0.2^{o}$] in the peaks of the calcite diffraction patterns in the 100% seawater specimen. This small shift is consistent with the reference signal of magnesian calcite, a precipitated mineral wherein magnesium ions are substituted for calcium ions within the crystalline structure of calcite at varying percentages. Although the S-Q analysis was not able to accurately quantify the relative amount of magnesium substitution, results qualitatively suggested that substitutions were present. It should also be noted that no magnesite ($MgCO_3$) peaks were detected in the diffraction patterns for any of the artificial seawater experiments. This was notable given the relatively low solubility of magnesite ($K_{sp} = 10^{-8.03}$). It remains possible, however, that given the equimolar concentrations of urea and calcium used, magnesite may have precipitated during the treatment process, but then ripened near the end of reactions to form lower solubility calcite minerals ($K_{sp} = 10^{-8.48}$) in a manner consistent with Ostwald ripening. It is also possible that if increased urea concentrations had been applied in these experiments, magnesite minerals may have persisted in end-state precipitates. The presence of magnesite and the conditions under which it may be formed during MICP merits further investigation as it may impact the long-term durability of MICP in marine environments.

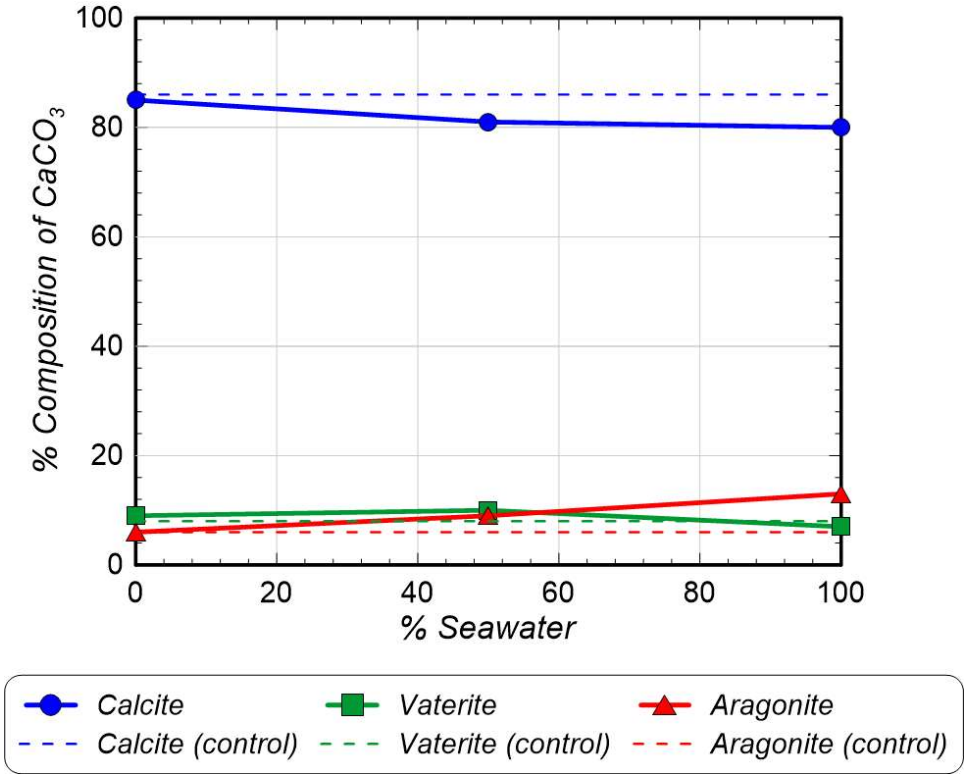

Figure 3.24 Relative $CaCO_3$ mineral content percentages for seawater varied experiments determined from XRD analyses.

As shown in Figure 3.25, SEM images revealed more dramatic differences in precipitate morphology for seawater varied experiments than the XRD results suggested. As shown in Figure 3.25a, the deionized water control sample showed almost exclusively rhombohedral crystal morphologies expected for calcite and also observed in earlier experiments. The 50% seawater sample (Figure 3.25b), however, showed the presence of some spherical morphologies expected for vaterite that were seemingly interspersed with rhombohedral morphologies. Many of the calcite-like crystal forms in this sample exhibited dull edges in comparison to the sharp, well-formed crystalline structures formed in deionized water. The images also showed a number of precipitates that appeared to be amorphous with almost no discernible crystalline structure. The abundance of unusual, amorphous morphologies is even more apparent in images of the 100%

seawater precipitates (Figure 3.25c). As shown in Figure 3.25d, vaguely rhombohedral forms were sometimes visible, however, crystal edges were more rounded when compared to the sharp edges observed for calcite crystals formed in the control experiment. Additionally, the faces of these crystal forms appeared to have a desiccated appearance in comparison to the flat, solid faces found in de-ionized water. Although amorphous calcite could not be detected in the XRD analyses completed, these SEM images suggest that many of the precipitates formed in the presence of seawater may have been amorphous.

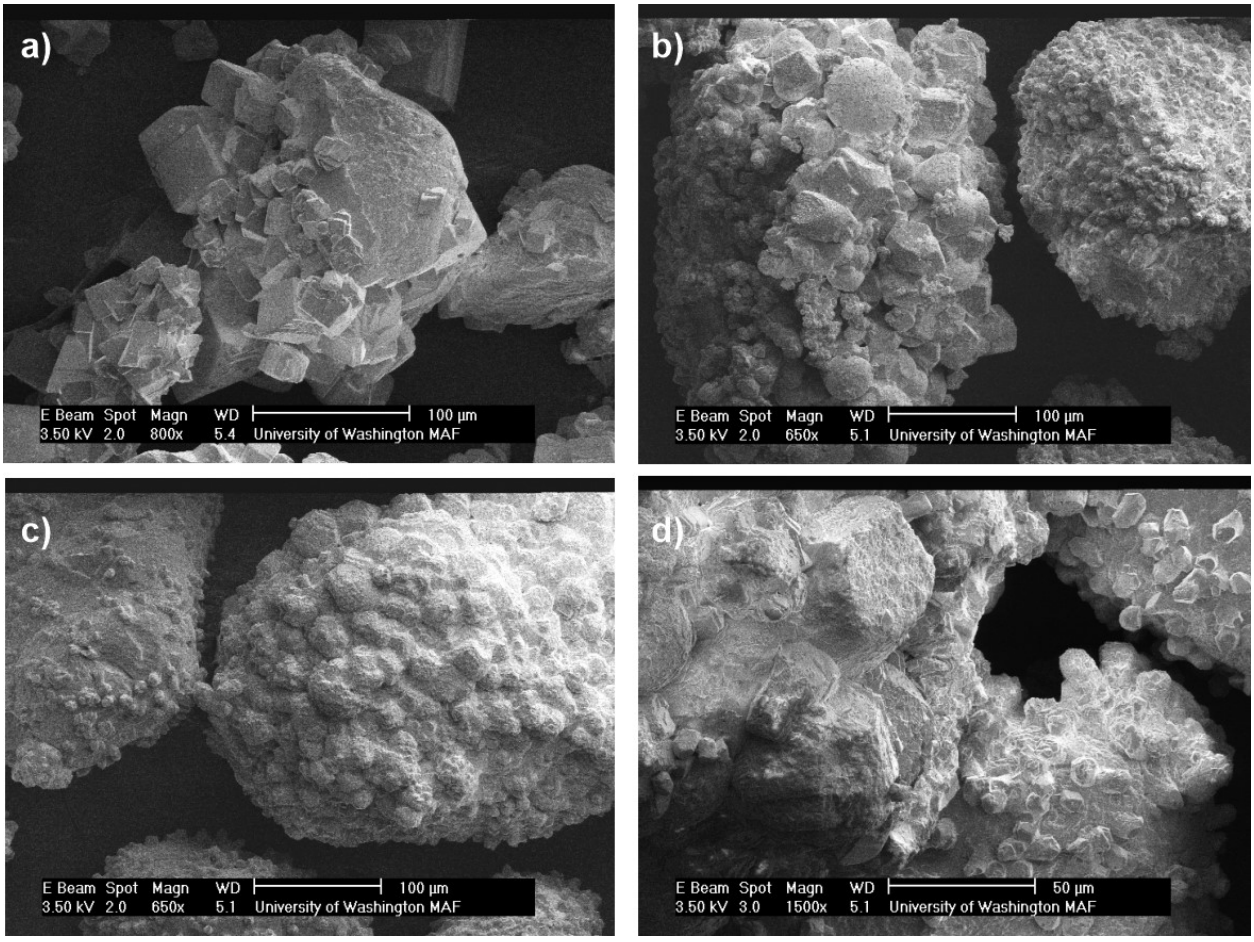

Figure 3.25 Representative SEM images of (a) 0% seawater, (b) 50% seawater, and (c,d) 100% seawater end-state precipitate samples.

3.5 GROUNDWATER IONS

3.5.1 *Magnesium*

In order to examine the effect of magnesium ions on the MICP process, four plate experiments were performed. All solutions were prepared using crystalline magnesium chloride hexahydrate (Fisher Scientific, 99.4% assay) at concentrations of 0 mM, 27 mM, 54 mM, and 108 mM. Selected concentrations corresponded to magnesium concentrations expected in 0%, 50%, 100%, and 200% seawater. Cementation solutions were prepared by adding 250 mM urea and calcium chloride dihydrate to each solution. Figure 3.21 presents normalized concentrations of urea and calcium in time for all magnesium concentration varied experiments. These results were discussed in greater detail in Chapter 3.4.1, however, in summary, large reductions in ureolytic rates were observed with increases in magnesium concentrations.

The obtained precipitates were characterized using XRD following all experiments. Figure 3.26 presents the results of the S-Q analysis of the observed diffraction patterns for the magnesium varied experiments. As shown, calcite was the dominant mineral phase in all experiments. At the highest magnesium concentration (108 mM), however, a slight decrease in the calcite relative percentage with a corresponding increase in the vaterite relative percentage was observed. Similar to the previously discussed seawater experiments, XRD results also showed a slight shift [up to $2\theta = 0.2^{o}$] in the peaks of the calcite diffraction patterns indicative of the presence of some magnesian calcite, although the relative abundance of this mineral could not be accurately quantified. Also similar to the seawater experiments, no magnesite was detected in any of the magnesium varied experiments, potentially due to ripening of precipitates into lower solubility calcite.

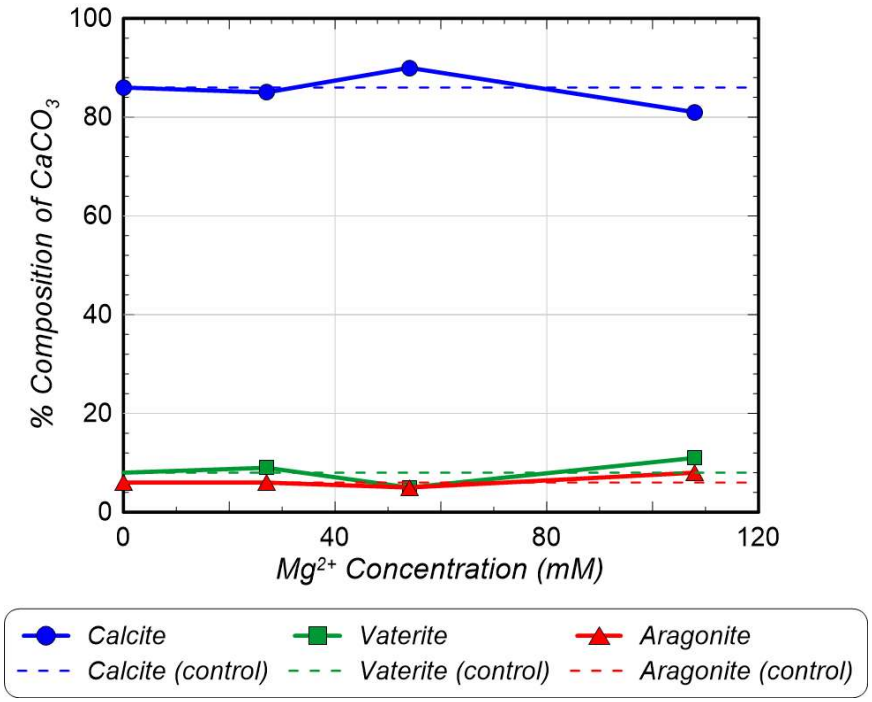

Figure 3.26 Relative $CaCO_3$ mineral content percentages for magnesium concentration varied experiments determined from XRD analyses.

Similar to the seawater experiments, although XRD results suggested little mineralogical differences between experiments, SEM images revealed more dramatic differences (Figure 3.27). While images of seawater experiments showed frequent amorphous and poorly-structured precipitates, more well-defined crystalline forms were observed in all magnesium concentration varied experiments. As expected, in the deionized water control sample (Figure 3.27a), rhombohedral forms were present that were consistent with the appearance of other calcite crystals observed in other control experiments . In the 27 mM magnesium experiment, however, forms were precipitated that often had 8 or more faces and crystals appeared to display a greater degree of anisotropy when compared to other crystals formed without magnesium present (Figure 3.27b). Observed crystal faces also often displayed a rougher surface texture. Similar crystal forms were observed at higher concentrations of magnesium (Figure 3.27c,d), with generally crystal surfaces

becoming rougher and crystal edges becoming smoother as magnesium concentrations increased. In addition, other crystal morphologies similar in appearance to “broken cylinders” became more prominent in the two highest magnesium concentration samples (54 mM, 108 mM). Somewhat surprisingly, truly amorphous forms similar to those observed in the seawater experiments were not observed, nor were spherical forms consistent with vaterite, despite XRD characterizations suggesting that slight increases in vaterite and aragonite were present in samples with increasing magnesium concentrations.

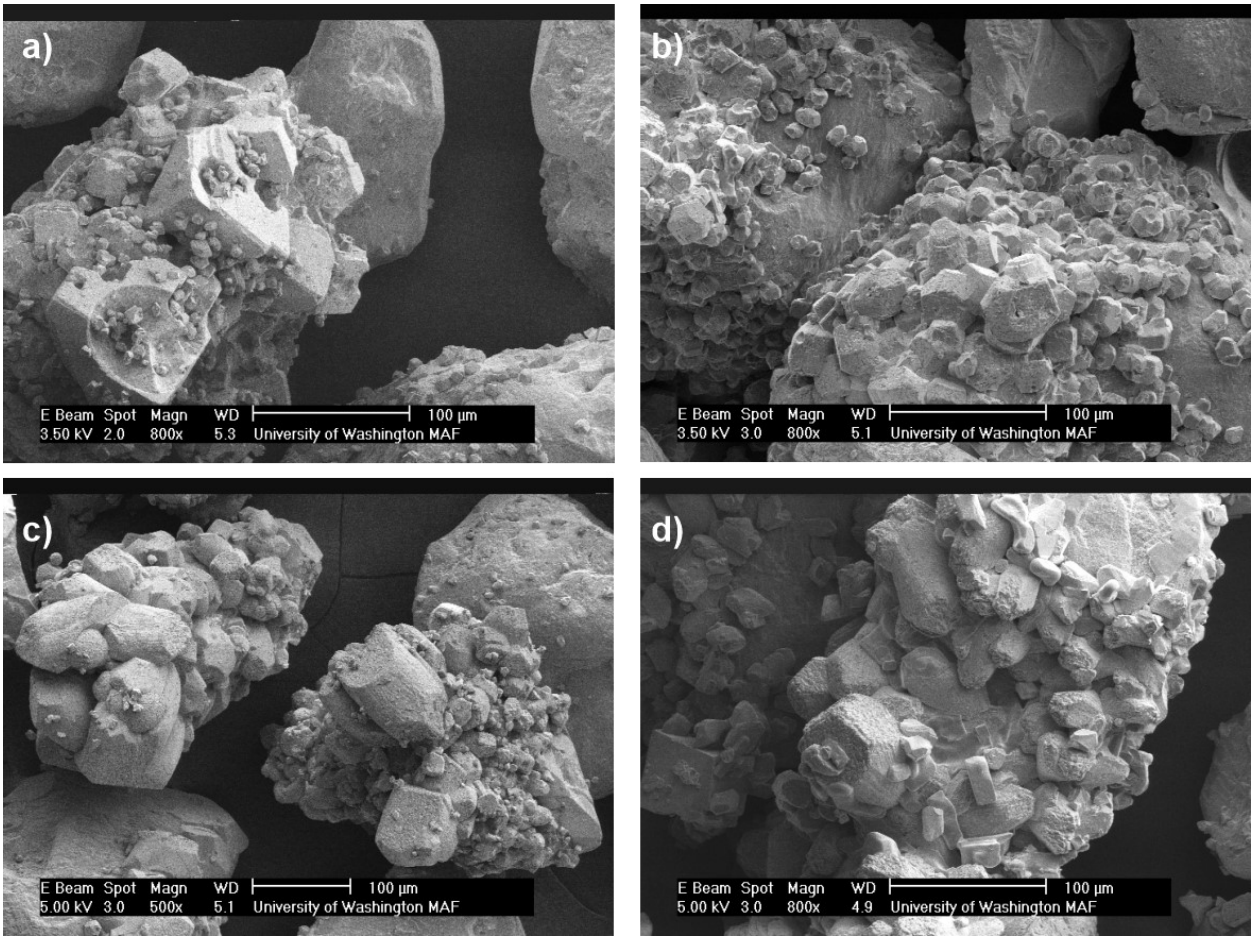

Figure 3.27 Representative SEM images of end-state precipitate samples from (a) 0 mM, (b) 27 mM, (c) 54 mM, and (d) 108 mM magnesium concentration experiments.

3.5.2 *Strontium and Sulfate*

In order to examine the effect of strontium and sulfate ions on the MICP process, five plate experiments were performed. All strontium varied solutions were prepared using strontium chloride hexahydrate (Fisher Scientific) at concentrations of 0 mM, 0.055 mM, 0.11 mM, and 0.22 mM. Again, selected concentrations corresponded to strontium concentrations in 0%, 50%, 100%, and 200% seawater. In addition, one sulfate solution was prepared using sodium sulfate powder (Alfa Aesar, >99.0% assay) at a concentration of 10 mM, which was 37% the concentration present in seawater and was selected solely to minimize the abiotic precipitation of gypsum during preparation (see Chapter 3.4.1). Cementation solutions were prepared by adding 250 mM urea and calcium chloride dihydrate to all solutions. Normalized concentrations of urea and calcium in time for all strontium and sulfate concentration experiments involving 250 mM calcium are presented in Figure 3.21. These results were discussed in greater detail in Chapter 3.4.1, however, in summary, no large changes in ureolytic rates were observed with changes in strontium or sulfate concentrations. Additional experiments were completed wherein higher concentrations of sulfate up to 28 mM were applied without calcium, and again no detectable effects on urea hydrolysis activity were observed (Figure 3.22).

End-state precipitates formed in the strontium and sulfate varied experiments containing 250 mM calcium were further characterized using XRD. Figure 3.28 presents the results of the S-Q analysis of the observed diffraction patterns for the strontium varied experiments. At all three strontium concentrations, calcite was found to be the dominant mineral phase with only minimal changes in relative precipitate compositions as strontium concentrations were increased. Although not plotted, the 10 mM sulfate experiment displayed similar results, with calcite, vaterite, and aragonite present at relative percentages of 85%, 10%, and 5%, respectively. Notably some

gypsum was also detected in the 10 mM sulfate experiment's XRD results; however, the amount of this mineral was small enough that it could not be reliably quantified in the S-Q analysis. Collectively, the S-Q results of the XRD diffraction patterns suggest that neither strontium nor sulfate appeared to have a significant effect on the calcium carbonate polymorphs precipitated during MICP when compared to the control condition.

SEM images for these experiments are presented in Figure 3.29. As shown, all precipitates appeared to have well-defined rhombohedral crystal forms that were consistent with the high calcite relative percentages detected using XRD. No other significant differences were observed when comparing precipitates from the highest strontium concentration experiment (Figure 3.29a) and sulfate concentration experiment (Figure 3.29b) to the de-ionized water control. Overall, these results suggest that strontium and sulfate ion concentrations appear to have minimal, if any, effects on the MICP process, when present at concentrations within the range examined.

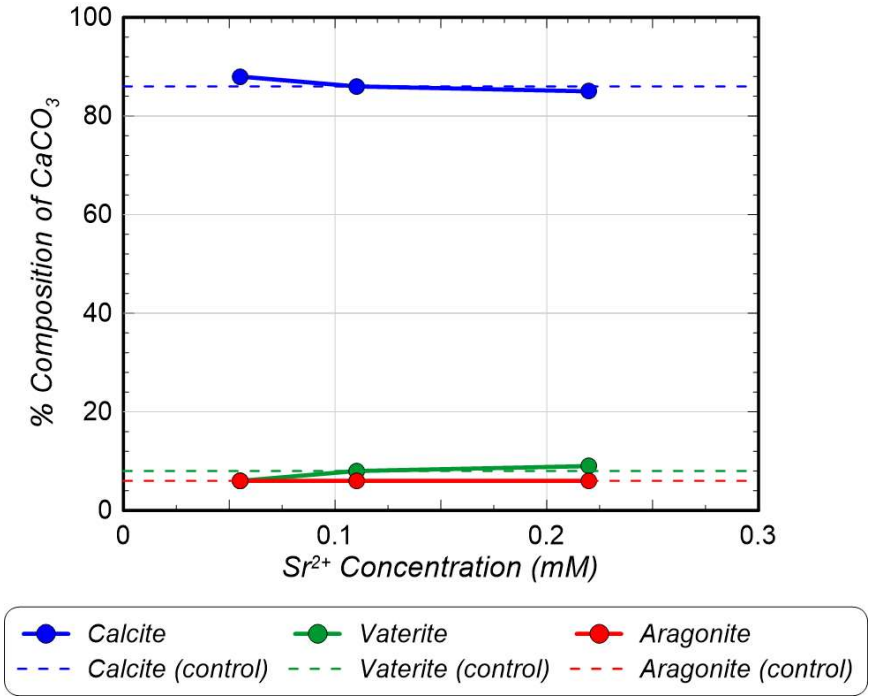

Figure 3.28 Relative $CaCO_3$ mineral content percentages for strontium concentration varied experiments determined from XRD analyses.

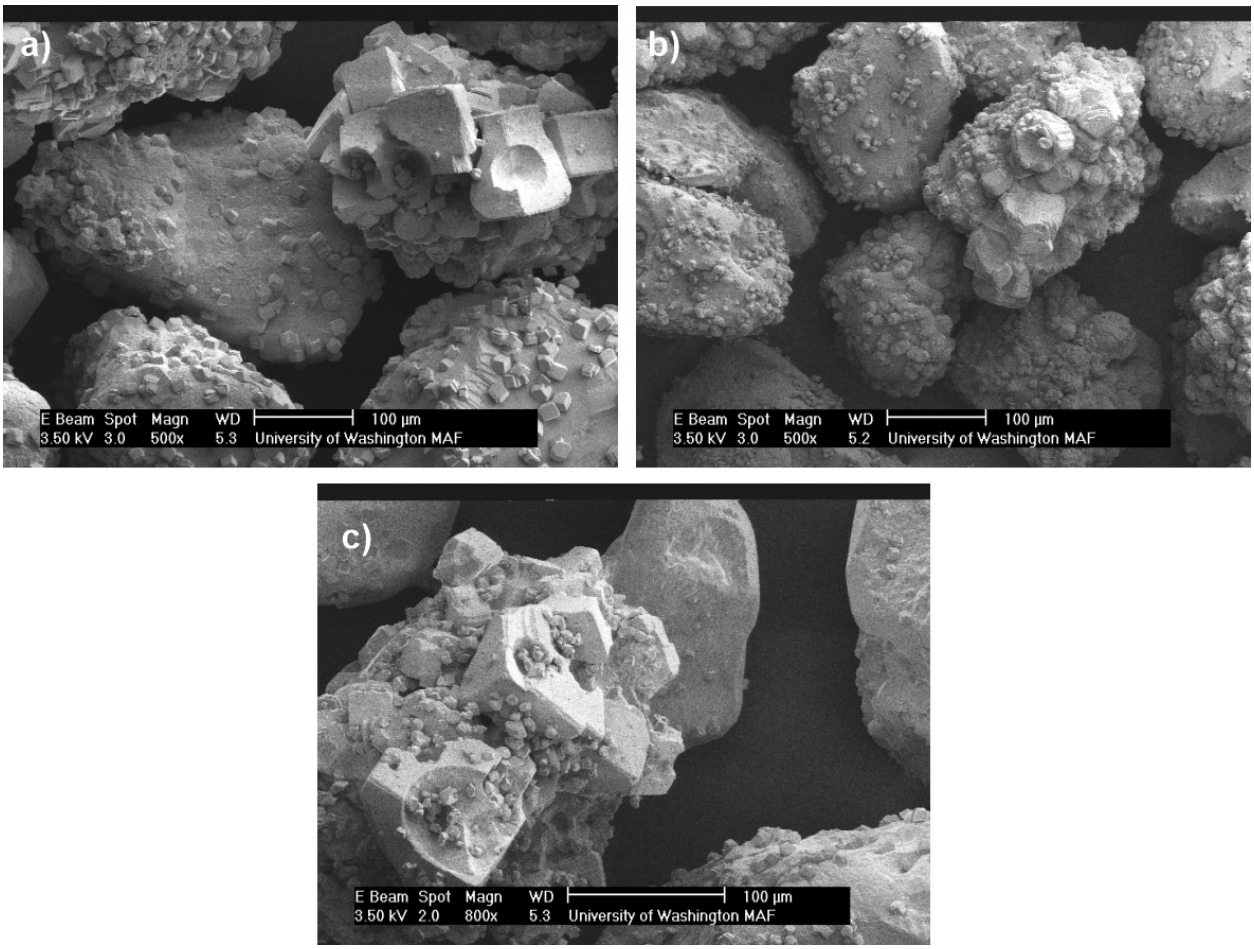

Figure 3.29 Representative SEM images of end-state precipitate samples from (a) 0.22 mM strontium, (b) 10 mM sulfate, and (c) control experiments.

3.5.3 *Sodium and Ionic Strength*

Although previous experiments focused on ion additions most relevant to marine environments, in other locations more passive ions may exist that can lower the activity of calcium and carbonate ions in solution through ionic strength increases. In order to study the effect of passive ions and ionic strength changes on the MICP process, a series of four plate experiments were performed containing varying concentrations of supplied sodium ions. Due to the relatively

high solubility of sodium chloride ($K_{sp} = 10^{1.58}$), sodium carbonate (soluble in water up to 300 g/L at 20°C), and sodium bicarbonate (soluble in water up to 87 g/L at 20°C) it was suspected that these sodium additions would not result in significant changes to resulting precipitates. Solutions were prepared using sodium chloride (Fisher Scientific, 99.6% assay) concentrations of 0 mM, 10 mM, 100 mM, and 1000 mM. The highest sodium concentration corresponded to roughly twice the sodium concentration of seawater. Examined sodium concentrations spanned three orders of magnitude in order to investigate relevant groundwater and seawater concentrations and magnify any potential ionic strength effects. All cementation solutions were prepared by adding 250 mM urea and calcium chloride dihydrate.

Figure 3.30 presents normalized concentrations of urea and calcium in time for all sodium concentration varied experiments. All experiments included *S. pasteurii* at a cell density of 8.0 x 10^7 cells/mL. As shown, minimal changes in ureolytic rates were observed for sodium concentrations ranging from 0 mM to 100 mM. In the 1000 mM sodium chloride specimen, a modest decrease (< 20%) in ureolytic rate was observed. The observed reduction in ureolytic activity at high ionic strength may be important for understanding and modelling ureolytic rates in MICP solutions containing high concentrations of calcium chloride and other dissolved salts as well as for MICP applications in highly saline locations such as arid desert environments. Furthermore, is also interesting to relate this finding to the results of the suite of experiments conducted in Chapter 3.4.1 examining the effect of magnesium concentration changes and seawater on ureolytic rates. Although magnesium concentration increases were found to be the most significant factor contributing to the inhibition of ureolysis, the inhibition observed in seawater could not be fully accounted for through magnesium ion additions alone. Following the

results of this investigation, it is likely that some fraction of the inhibition observed in seawater solutions can likely be attributed to the high ionic strength of seawater (≈ 0.7 M).

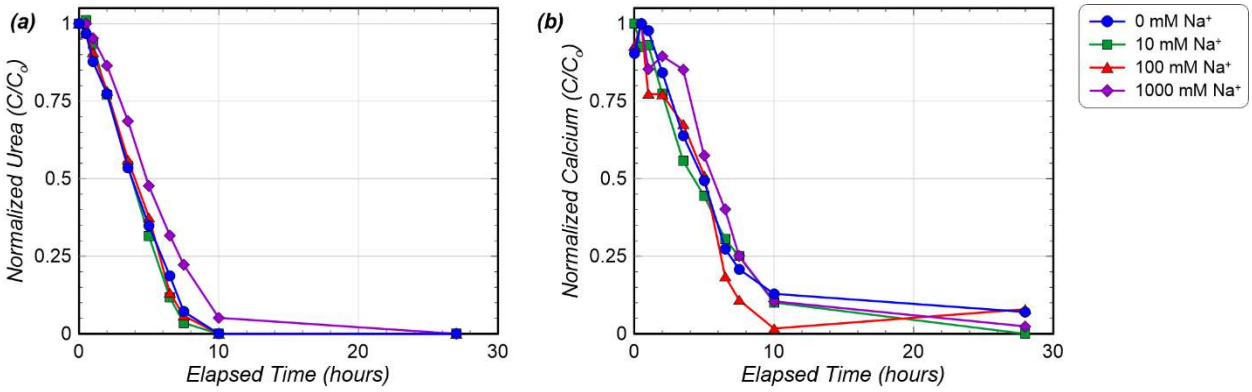

Figure 3.30 Normalized concentrations of (a) urea and (b) calcium in time for experiments with varying concentrations of sodium.

Figure 3.31 presents SEM images of end-state precipitates from select sodium concertation varied experiments. As shown in Figure 3.31b, precipitates from the highest sodium concentration (1000 mM) experiment generally exhibited well-defined rhombohedral forms that were consistent with the crystalline structure of calcite and the control experiment containing no sodium (Figure 3.31a). No other significant differences in precipitate morphology, distribution, or size were observed with changes in sodium concentrations. Although XRD results are not provided herein, given the similarity in SEM images and process kinetics, it was concluded that changes in sodium concentrations had minimal, if any, effects on end-state precipitates.

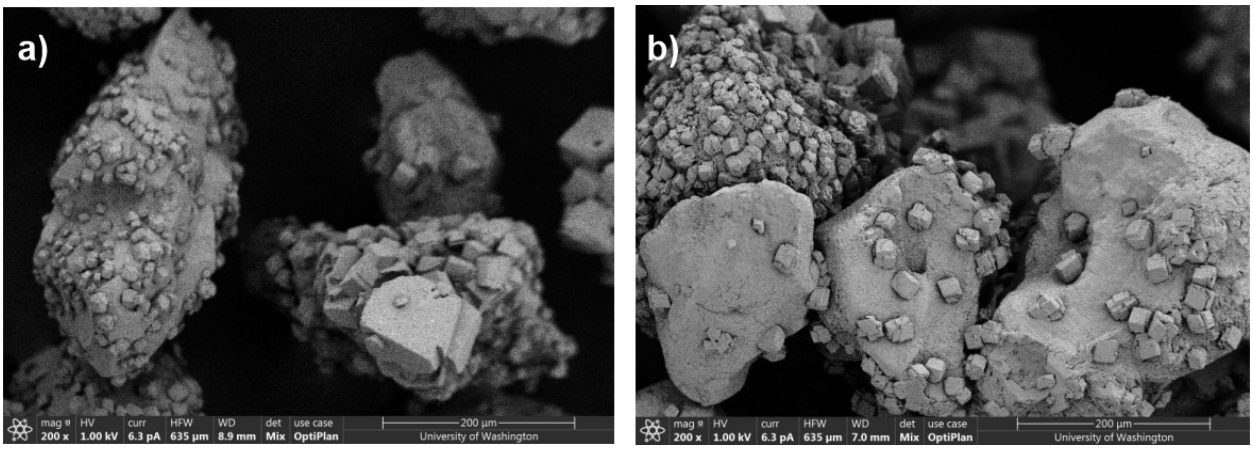

Figure 3.31 Representative SEM images of end-state precipitates from (a) 0 mM and (b) 1000 mM sodium concentration experiments.

3.6 INORGANIC TREATMENT ADDITIVES

A variety of chemical additives are commonly included in MICP treatment solutions. Here we explore two of the most commonly added inorganic chemical constituents, ammonium chloride and sodium bicarbonate, to explore their effects on process reaction kinetics and end-state precipitates.

3.6.1 *Sodium Bicarbonate*

Sodium bicarbonate is a commonly supplied treatment additive in MICP cementation solutions. While the exact rationale for adding sodium bicarbonate to these solutions is not fully clear, past studies have suggested that increases in carbonate species resulting from sodium bicarbonate additions may offer the ability to more strongly buffer cementation solutions, thus mitigating large pH changes (Al Qabany and Soga, 2013). In addition to this potential benefit, it is suspected that the introduction of sodium bicarbonate may increase abiotic calcium carbonate precipitation, thus allowing for increased $CaCO_3$ precipitation when ureolytic activity is poor and full reactions cannot be achieved through ureolysis alone. When sodium bicarbonate is added at

sufficient concentrations and surrounding solution pH permits the presence of carbonate ions, these sodium bicarbonate additions can result in supersaturation of solutions with respect to $CaCO_3$ mineral phases even before ureolysis begins. Thus, less carbonate production from microbial ureolysis is required to initiate and maintain supersaturation of solutions. Although perhaps once viewed as being beneficial, it is suspected that the abiotic formation of $CaCO_3$ may limit obtained engineering improvements through the precipitation of $CaCO_3$ in free solution rather than on soil particle surfaces and contacts where many of the ureolytic microbes meditating this reaction reside. Concentrations of sodium bicarbonate used in cementation solutions have differed significantly between studies with concentrations ranging from 25 mM (DeJong et al., 2006, and many others) to 167 mM (Spencer, Sass, 2019).

In order to examine the effect of sodium bicarbonate additions on the MICP process a series of four plate experiments was performed. All cementation solutions were first prepared by adding 250 mM urea and calcium chloride dihydrate to deionized water. In order to reduce the possibility of abiotic precipitation events occurring before experiments, crystalline sodium bicarbonate (Fisher Scientific, ≈100.1% assay) was added to all solutions immediately prior to experiments at concentrations of either 0 mM, 25 mM, 250 mM, or 1000 mM. Concentrations were selected to encompass values used in previous MICP experiments and spanned three orders of magnitude to maximize our ability to observe potential effects on the MICP process. All experiments contained *S. pasteurii* cells at an estimated cell density of 7.6×10^7 cells/mL.

Figure 3.32 presents normalized concentrations of urea and calcium in time for all sodium bicarbonate concentration varied experiments. As shown, no significant differences in urea hydrolysis rates were observed as concentrations of sodium bicarbonate were increased. In contrast, calcium trends in time showed more interesting differences. As shown, greater soluble

calcium reductions were observed in time when sodium bicarbonate concentrations were increased, suggesting increases in $CaCO_3$ precipitation rates. As expected, this suggested that as carbonate ions became increasing available from sodium bicarbonate additions, greater abiotic calcium carbonate precipitation occurred. In the absence of urea hydrolysis, it is suspected that continued carbonate consumption from abiotic $CaCO_3$ precipitation may have stopped precipitation reactions in time due to pH decreases. Thus, even when higher sodium bicarbonate concentrations are added, urea hydrolysis may play some role in precipitation events, particularly near the end of reactions where hydroxide ion production is needed to maintain supersaturation.

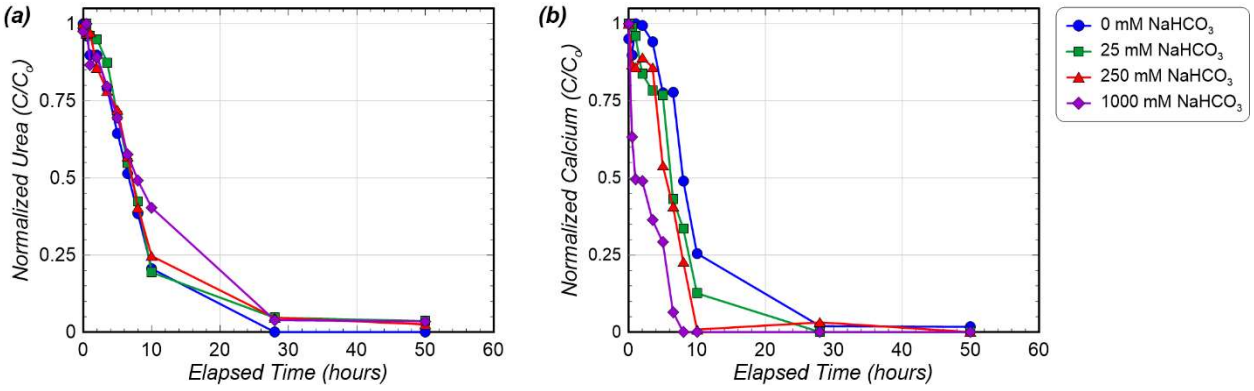

Figure 3.32 Normalized concentrations of (a) urea and (b) calcium in time for sodium bicarbonate varied experiments.

Following all experiments, end-state precipitates were characterized using XRD. Figure 3.33 presents the results of the S-Q analysis of the observed diffraction patterns for the sodium bicarbonate concentration varied experiments. In all experiments, calcite was found to be the dominant mineral phase and was present at similar relative percentages as that observed in the control. In the 250 mM sodium bicarbonate specimen, a previously absent peak at a 2θ value of 31.7º was observed, likely corresponding to the presence of halite (NaCl). A similar and stronger

peak was also observed in the 1000 mM sodium bicarbonate sample. The relative amount of halite in the 250 mM and 1000 mM sodium bicarbonate experiments was relatively small, corresponding to roughly 1.5% and 3% of the total precipitated non-quartz minerals quantified in the S-Q analysis, respectively.

Overall, only minimal changes in the composition of $CaCO_3$ precipitates was observed as sodium bicarbonate concentrations increased. The relative consistency of $CaCO_3$ mineral compositions for all three plate experiments suggested that the addition of sodium bicarbonate to cementation solutions did not have an appreciable effect on the calcium carbonate polymorphs precipitated during MICP. XRD analyses do, however, suggest that the addition of sodium bicarbonate may encourage some minor precipitation of halite in addition to calcium carbonate minerals when concentrations of sodium bicarbonate exceed 250 mM. Given the high solubility of halite ($K_{sp} = 10^{1.58}$), however, it is likely that the presence of this mineral resulted from the precipitate rinsing and drying process used in this study and may not be expected to exist in most environments under fully-saturated conditions.

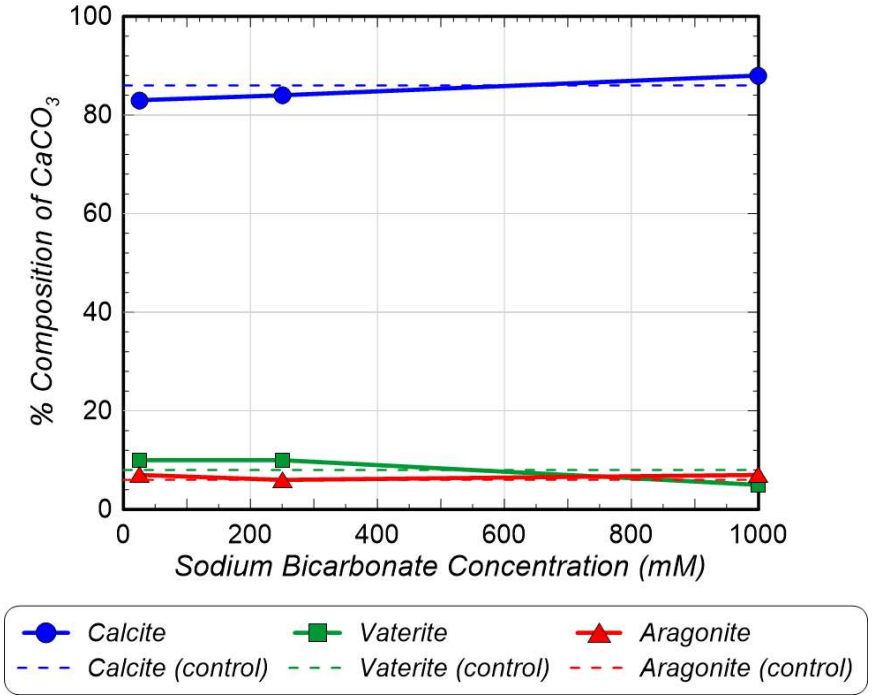

Figure 3.33 Relative $CaCO_3$ mineral content percentages for sodium bicarbonate concentration varied experiments determined from XRD analyses.

Figure 3.34 presents SEM images of end-state precipitates from sodium bicarbonate concentration varied experiments. As shown, images for all experiments generally showed well-defined rhombohedral crystal forms that were consistent with the morphology of calcite. However, considerable differences in precipitate distributions and crystal sizes were observed between the high sodium bicarbonate concentration (1000 mM) experiment and the control. At the highest sodium bicarbonate concentration, SEM images suggested that the majority of the calcium carbonate minerals formed did not exist on sand particle surfaces (Figure 3.34a), in stark contrast to the control experiment (Figure 3.34b). In addition, when examining precipitates more closely (Figure 3.34c,d), crystals observed at higher sodium bicarbonate concentrations were generally smaller (diameter ≈10-20 μm) than crystals observed in the control (diameter ≈20-80 μm). This suggested that when higher concentrations of sodium bicarbonate were present, calcium carbonate

precipitation may occur more frequently in bulk solution and/or on suspended cell surfaces rather than on soil particle surfaces. Given the more rapid $CaCO_3$ precipitation observed with direct chemical measurements when sodium bicarbonate was increased, these results collectively suggest that abiotic precipitation events may encourage the formation of greater magnitudes of $CaCO_3$ in bulk solution. This result may have important implications for the engineering properties of resulting bio-cemented soils as precipitates existing on soil surfaces would be expected to result in greater shear strength and stiffness increases when compared to precipitates existing within soil pore spaces without soil particle bonds. It is also hypothesized that bio-cementation precipitated on soil surfaces may be more resistant to degradation and removal by existing hydraulic gradients and groundwater flow over time.

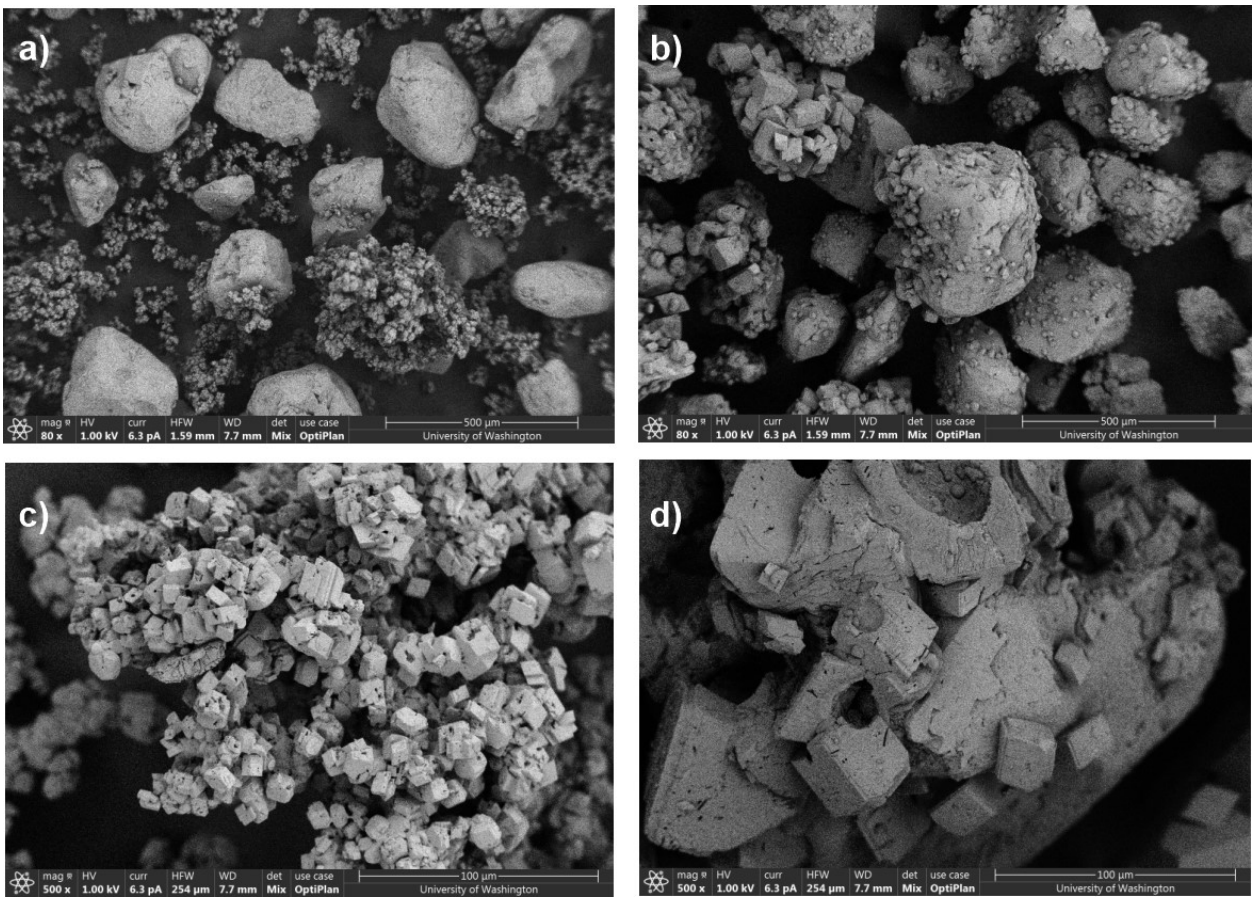

Figure 3.34 Representative SEM images of end-state precipitate samples from (a,c) 1000 mM and (b,d) 0 mM sodium bicarbonate concentration varied experiments at (a,b) 80x and (c,d) 500x magnifications.

3.6.2 *Ammonium Chloride*

Ammonium chloride is another inorganic chemical additive commonly included in MICP cementation solutions. Ammonium chloride has been identified as a non-competitive urease enzyme inhibitor in past studies examining the kinetics of ureolysis using free enzymes (Hoare and Laidler 1950; Fidaleo and Lavecchia 2003), meaning that it inhibits the activity of urease enzymes by binding to non-active sites on the enzyme. On the other hand, other studies have suggested that ammonium chloride concentrations of up to 190 mM do not have any significant effects on ureolytic activity for whole *S. pasteurii* cells (Lauchnor et al., 2015). Although not

explicitly stated in the literature, the rationale for adding ammonium chloride to cementation solutions appears to have been to prevent ureolysis from occurring too quickly during solution injections. Ureolysis and cementation reactions occurring during solution transport can localize precipitates near injection locations, leading to unfavorable reductions in permeability and uneven gradients of cementation across targeted treatment zones. Beyond potentially improving the spatial uniformity of bio-cementation, ammonium chloride has also been included in treatment solutions when indigenous ureolytic microorganisms are enriched *in-situ* in a process known as bio-stimulation. In these solutions, ammonium chloride is included specifically to enhance the enrichment process through increased selective pressure for ureolysis. Concentrations of ammonium chloride used in MICP treatments have ranged between 12.5 mM (Gomez et al. 2014, 2016, 2018) up to values near 374 mM (Martinez et al., 2013).

In order to further explore the effect of ammonium chloride concentrations on the MICP process, four plate experiments were performed. All solutions were prepared using ammonium chloride (Fisher Scientific, 99.6% assay) at concentrations of 0 mM, 10 mM, 100 mM, and 1000 mM. Selected concentrations spanned three orders of magnitude intended to better understand how ammonium chloride concentrations may inhibit ureolytic activity for whole *S. pasteurii* cells as well as influence resulting precipitates. Cementation solutions were prepared by adding 250 mM urea and calcium chloride dihydrate to all solutions. All experiments contained *S. pasteurii* cells at an estimated cell density of 7.6×10^7 cells/mL.

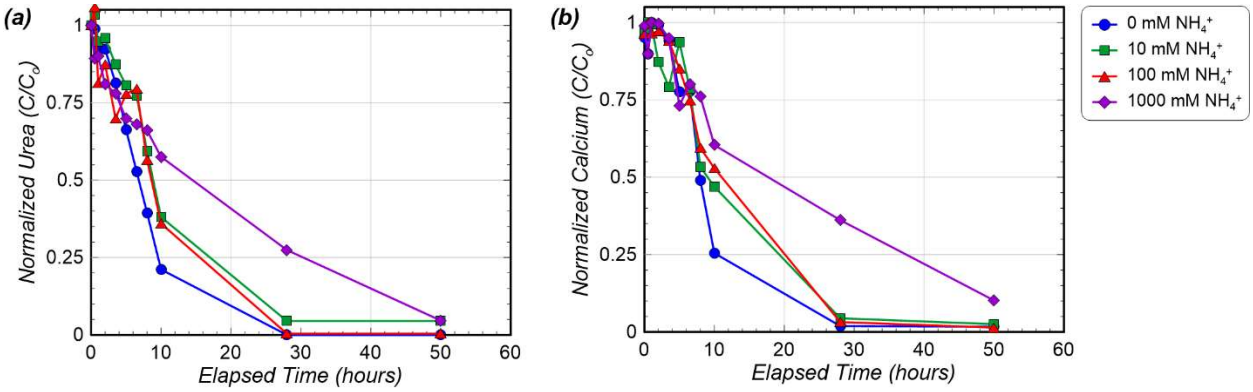

Figure 3.35 Normalized concentrations of (a) urea and (b) calcium in time for experiments containing varying concentrations of ammonium chloride.

Figure 3.35 presents normalized concentrations of urea and calcium in time for all ammonium chloride concentration varied experiments. As shown, 10 mM and 100 mM ammonium chloride concentration experiments exhibited some detectable inhibition of ureolysis with a near 20% reduction in initial ureolytic rate. Additionally, when ammonium chloride concentrations were increased to 1000 mM, greater inhibition of ureolysis was observed corresponding to a near 75% reduction in initial ureolytic rate. While some of this inhibition may have been related to increased ionic strength, the observed ureolytic rate reduction was substantially higher than that observed in an experiment containing an identical concentration of sodium chloride presented in Chapter 3.5.3. Thus, it is suspected increases in solution ionic strength contributed only marginally to the observed inhibition of ureolysis in these experiments.

In order to better distinguish the inhibitory effects of ammonium chloride on ureolysis from ionic strength related effects, a set of seven additional plate experiments was performed wherein equivalent concentrations of ammonium chloride and sodium chloride were supplied. All solutions were prepared using either crystalline ammonium chloride (Fisher Scientific) or sodium chloride (Fisher Scientific) at concentrations of 10 mM, 100 mM, and 1000 mM for each. A control

experiment was also included with no salts added. Cementation solutions were prepared by adding 250 mM urea and calcium chloride dihydrate to the prepared solutions. All experiments contained S. *pasteurii* cells at an estimated cell density of 8.0×10^7 cells/mL.

Figure 3.36 presents normalized concentrations of urea and calcium in time for the ammonium chloride and sodium chloride concentration varied experiments. When compared to the previous experiment, surprisingly the 10 mM ammonium chloride experiment showed no rate inhibition. Additionally, the 10 mM and 100 mM sodium chloride experiments also showed no ureolytic rate changes when compared to the control. In both the 100 mM ammonium chloride experiment and the 1000 mM sodium chloride experiment, however, initial ureolytic rates decreased by nearly 20%. When ammonium chloride concentrations were further increased to 1000 mM, significantly stronger inhibition of ureolysis was observed corresponding to an initial rate decrease near 50%. The results further suggested that ammonium chloride additions may substantially inhibit ureolysis reactions for whole *S. pasteurii* cells when ammonium chloride concentrations greater than near 100 mM are present. Although ionic strength increases were found to somewhat inhibit ureolysis, increases in total ammonium concentrations appeared to result in more significant inhibition of ureolysis that was distinctly different than ionic strength effects. This result may be particularly significant for accurate predictions of ureolytic rates during MICP reactions, as ureolysis directly generates two moles of total ammonium per mole of hydrolyzed urea. Interestingly, inhibition of ureolysis in this experiment was also observed at lower concentrations of ammonium chloride (100 mM) then observed in the past study by Lauchnor et al. (2015), which suggested that ureolysis was not inhibited for whole *S. pasteurii* cells at ammonium chloride concentrations up to 190 mM.

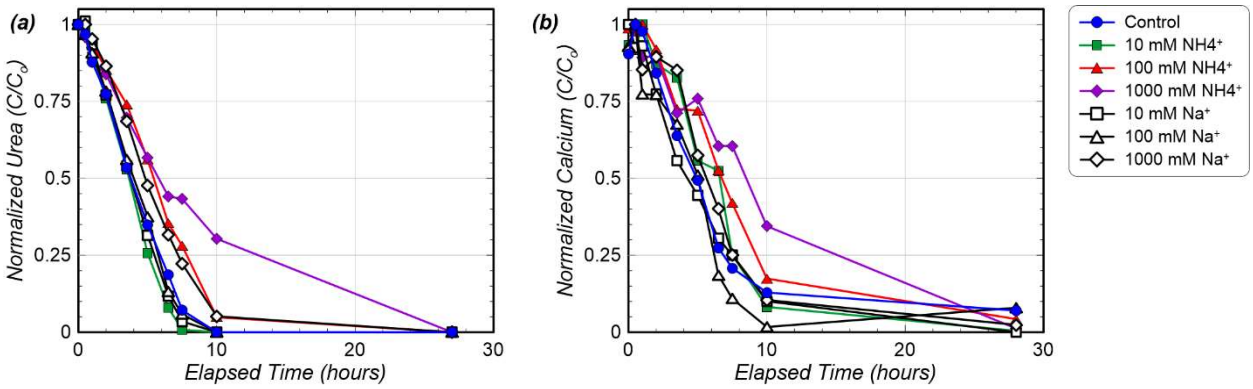

Figure 3.36 Normalized concentrations of (a) urea and (b) calcium in time for experiments wherein ammonium chloride and sodium chloride concentrations were varied to examine potential effects on ureolytic rates.

Following experiments, end-state precipitates were characterized using XRD. Figure 3.37 presents the results of the S-Q analysis of the observed diffraction patterns for all ammonium chloride concentration varied experiments. In all experiments, calcite was found to be the dominant mineral phase and existed at similar relative percentages as that observed in the control specimen. Additionally, minimal changes in relative $CaCO_3$ precipitate compositions were observed as ammonium chloride concentrations were increased up to 1000 mM. The relative consistency of the mineral compositions in all ammonium chloride varied experiments suggested that the addition of ammonium chloride to cementation solutions did not have an appreciable effect on the calcium carbonate polymorphs precipitated during MICP.

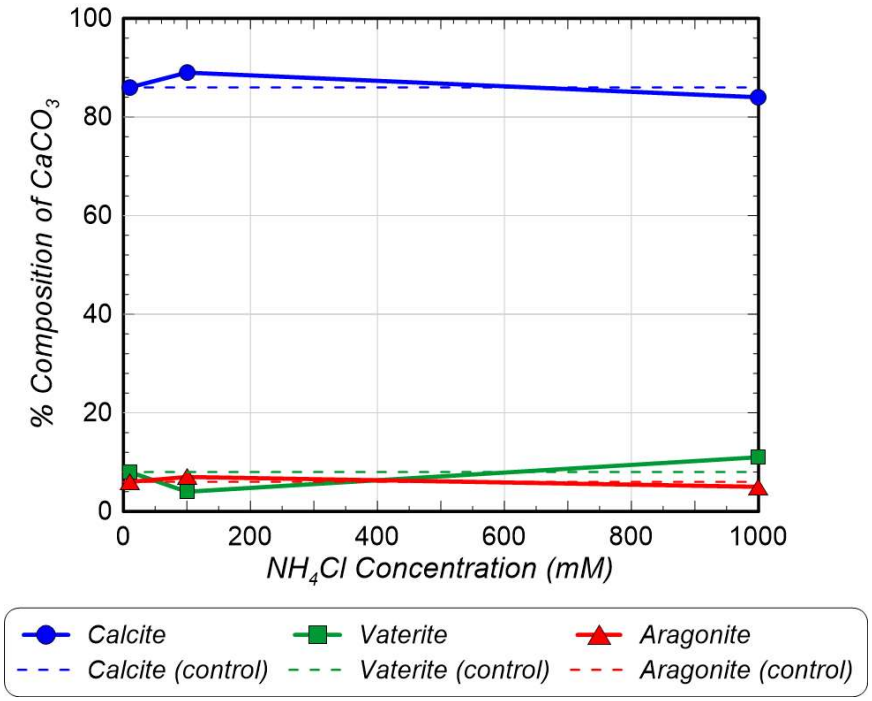

Figure 3.37 Relative $CaCO_3$ mineral content percentages for ammonium chloride concentration varied experiments determined from XRD analyses.

SEM images presented in Figure 3.38 support the previous XRD findings as precipitates visible from all ammonium chloride varied experiments demonstrated well-defined rhombohedral forms consistent with calcite. No other significant differences in morphology or distribution were observed when comparing SEM images of precipitates from the highest ammonium chloride concentration (Figure 3.38a,c) to the control (Figure 3.38b,d). Additionally, crystal sizes were generally similar between experiments (diameter ≈ 20-80 μm), although the highest ammonium chloride concentration specimen appeared to have mostly larger crystals within this size range. While this could be related to the significantly slower precipitation rate that occurred in the 1000 mM ammonium chloride experiment, these apparent differences may have been influenced by the small sample size used for these images. Nevertheless, increases in precipitate crystal sizes have been observed in other past MICP studies when slower ureolytic rates were present (Gomez et al.

2019). Overall, the results of these experiments suggest that ammonium chloride concentration likely have only minimal effects on end-state precipitates but can have significant effects on reaction kinetics when supplied at concentrations exceeding 100 mM.

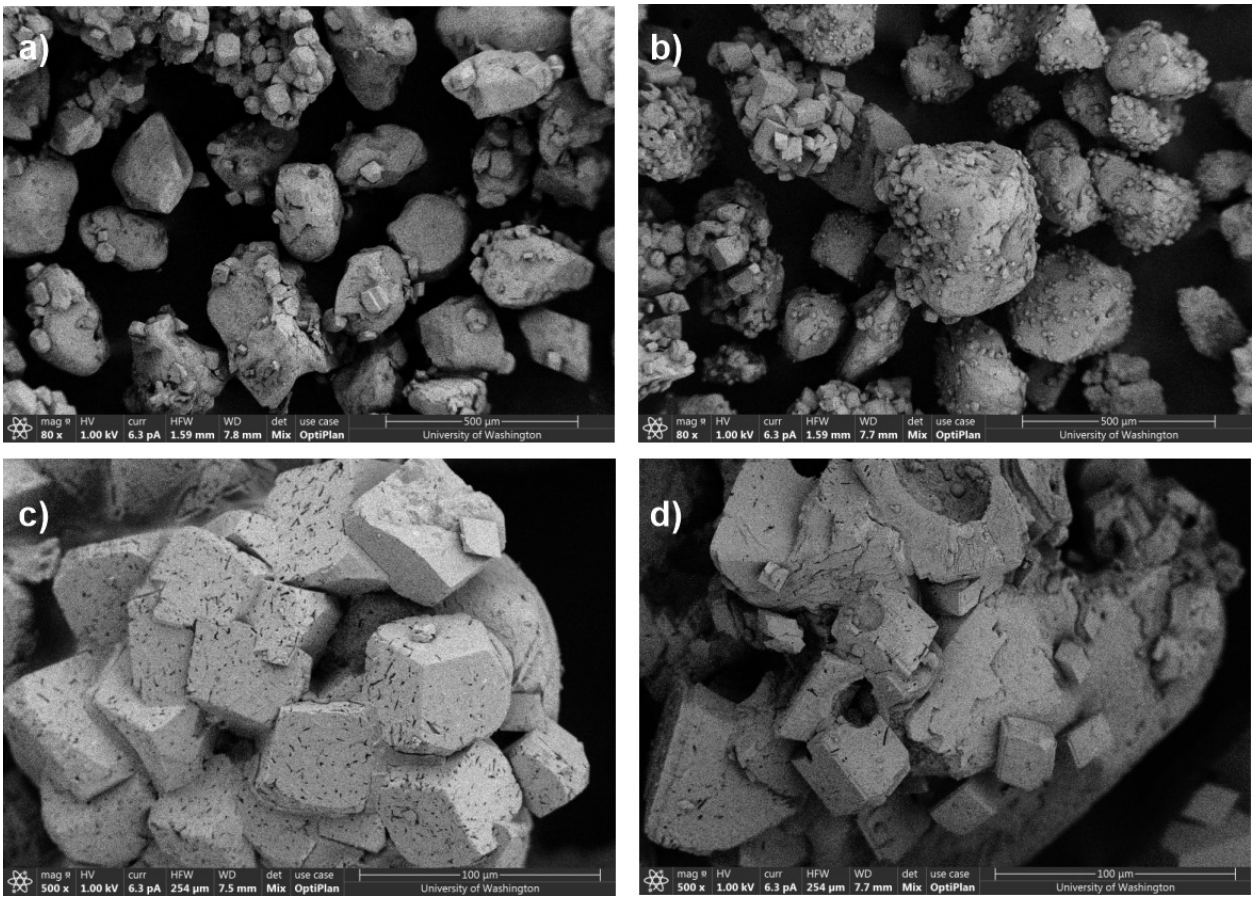

Figure 3.38 Representative SEM images of end-state precipitate samples from (a,c) 1000 mM and (b,d) 0 mM ammonium chloride concentration varied experiments at (a,b) 80x and c,d) 500x magnifications.

3.7 SOIL TYPES

Most experimental studies have applied MICP to well-characterized, relatively permeable, poorly-graded granular soils, which allow for ease of specimen preparation, increases in sample homogeneity, and relatively fast treatment injections. All experiments conducted thus far in this study were performed using a similar poorly-graded Ottawa F-65 sand, which has well-defined properties and is primarily composed of quartz mineral. While the majority of past studies have applied MICP treatments to similar quartz sands, several studies have also investigated the use of bio-cementation in other soil types including carbonate sands (Dyer and Viganotti 2017, Xiao et al., 2018), silty sands (Zamani 2017), soft clays (Xiao et al., 2020), sand and clay mixtures (Jiang et al., 2017), sandstones (Zhe et al., 2016), organic soils (Phang et al., 2018), fine oil sand tailings (Liang et al., 2015), sands contaminated with heavy metals (Achal, V., 2011), coal ash (Safavizadeh et al., 2019), and other anthropogenic and natural geomaterials. During field-scale MICP applications, the mineralogy of existing soils cannot be directly controlled, however, an improved understanding of the effect of soil type on precipitate mineralogy may allow for determination of optimal and suboptimal conditions for MICP. It is suspected that changes in soil type may influence the morphology, mineralogy and/or distribution of calcium carbonate precipitates following MICP in a number of ways including through changes in pore fluid ion compositions, particle surface roughnesses, mineralogical compositions, particle sizes, and soil surface charges. Thus, understanding the effect of soil type on MICP may be important towards identifying its efficiency at a particular site. Through identification of unfavorable soil mineralogies for MICP, it is possible that field challenges may be better anticipated and/or avoided entirely.

In order to examine the effect of different parent soils of varying particle sizes and mineralogies on the MICP process eleven different plate experiments were performed. These experiments can be roughly divided into two subgroups: (1) well-characterized soils of relatively pure mineralogy (Quartz, Feldspar, Olivine, Mica, Kaolinite, and Montmorillonite) and (2) site specific sand mixtures of varying mineralogies from a variety of different natural sources and depositional environments (Fraser River Sand, Concrete Sand, Covelo Sand, Delta Sand, and Monterey Sand). Prior to experimentation, XRD analyses were completed on untreated samples of each soil type to identify the major minerals present.

Table 3.3 presents the results of the S-Q analyses completed on the observed diffraction patterns, as well as the source of each soil material. Consistent with all previous experiments, 5.3 grams of soil were added to each plate experiment with the exception of the clay mineral tests (Kaolinite and Montmorillonite) wherein 2.3 grams and 1.1 grams were added to the kaolinite and montmorillonite plates, respectively. Reductions in added soil masses in these clay mineral experiments were completed in order to maintain enough free aqueous solutions within experiments to allow for timed sampling. All soil samples were oven-dried at temperatures of 120 ºC for 48 hours prior to experiments and all solutions were intentionally non-nutritive to reduce the potential for biological contamination and limit the presence of trace organics. All cementation solutions were initially prepared by adding 250 mM urea and calcium chloride dihydrate to deionized water. Similar to previous experiments, all soils were inoculated with *S. pasteurii* cells and refrigerated at 4º C for 24 hours before all experiments.

Table 3.3. Primary Mineralogical Composition of Tested Soils (Determined from XRD Analyses)

Soil	Primary Mineral	Other Minerals	Source
Ottawa Sand	Quartz (~100%)	-	US Silica Inc.
Feldspar	Microcline (78%)	Albite (12%), Quartz (10%)	Northern West Stuff
Olivine	Forsterite (90%)	Fayalite (10%)	Northern West Stuff
Mica	Lepidolite (~100%)	-	Northern West Stuff
Kaolinite	Kaolinite (~100%)	-	Unknown Source
Montmorillonite	Montmorillonite (96%)	Quartz (4%)	Unknown Source
Fraser River Sand	Quartz (85%)	Albite (15%)	Field Sample (Delta, BC)
Concrete Sand	Quartz (75%)	Albite (25%)	Teichert Aggregates (Woodland, CA)
Covelo Sand	Quartz (87%)	Albite (13%)	Field Sample (Covelo, CA)
Delta Sand	Quartz (58%)	Albite (42%)	Syar Industries (Petaluma, CA)
Monterey Sand	Quartz (47%)	Microcline (42%), Albite (11%)	Cemex Inc. (Pleasanton, CA)

Figure 3.39 presents normalized concentrations of urea and calcium in time for all experiments containing pure mineral soils (Figure 3.39a, b) and sand mixture soils (Figure 3.39c, d). All experiments were inoculated with *S. pasteurii* cells at an estimated cell density of 8.2×10^7 cells/mL. As shown, for the relatively pure mineral soil experiments, minimal changes in ureolytic rates were observed between experiments. The kaolinite and mica plate experiments, however, did show relatively minor increases in initial ureolytic rate of less than 20%. While the mechanisms

responsible for increases in ureolytic rates in these experiments were not clear, it remains possible that small variations in inoculated bacterial cell densities could have occurred between samples.

Interestingly, many of the natural sand specimens (Fraser Sand, Covelo Sand, Delta Sand, and Concrete Sand) showed detectable decreases in ureolytic rates when compared to the Ottawa F-65 Sand control experiment (Figure 3.39c). In particular, the Fraser River Sand experiment showed such a pronounced inhibition of ureolysis that urea degradation activity appeared to cease entirely near 35% reaction completion. Similarly, the mechanisms responsible for large decreases in ureolytic activity in the tested natural sand mixtures remained unclear as they were primarily composed of common quartz and feldspar minerals that were not found to affect ureolytic rates in other plate experiments. One possibility is that exchangeable ions such as magnesium may have existed on soil surfaces and altered the composition of solutions in these experiments. Although not fully identified, these inhibiting ions may have compromised enzyme or cellular functions even at relatively low concentrations. Soils used in the Fraser River Sand experiment were gathered from a deltaic area where soils were subjected to brackish and marine groundwater conditions depending on seasonal and tidal fluctuations. This area also contains transported sediments from other locations with strong industrial use, suggesting that trace concentrations of heavy metals and other contaminants may be present in this soil. It should also be noted that similar reductions in ureolytic activity were also observed during multiple MICP treatments performed using small-scale soil columns in an unpublished study involving this same Fraser River Sand material.

Collectively the results of these soil varying experiments suggested that while soil mineralogies can influence ureolysis, these effects are generally only small when higher purity minerals are present. In natural soil mixtures, however, trace minerals and ions may play a critical role in affecting observed ureolytic activity. Interestingly when these soil mixtures were

characterized using XRD, obtained results did not suggest the presence of significant amounts of other minerals that were not evaluated in other pure mineral experiments which showed minimal ureolytic inhibition. This suggests that exchangeable ions may be responsible for the observed activity differences. Additionally, the signification inhibition of ureolysis in the Fraser River Sand experiment was somewhat consistent with the results of the seawater experiments, wherein marine conditions were found to inhibit ureolysis. While definitive mechanisms could not yet be isolated for these experiments, future analysis of exchangeable ions present in these soils may provide more conclusive information.

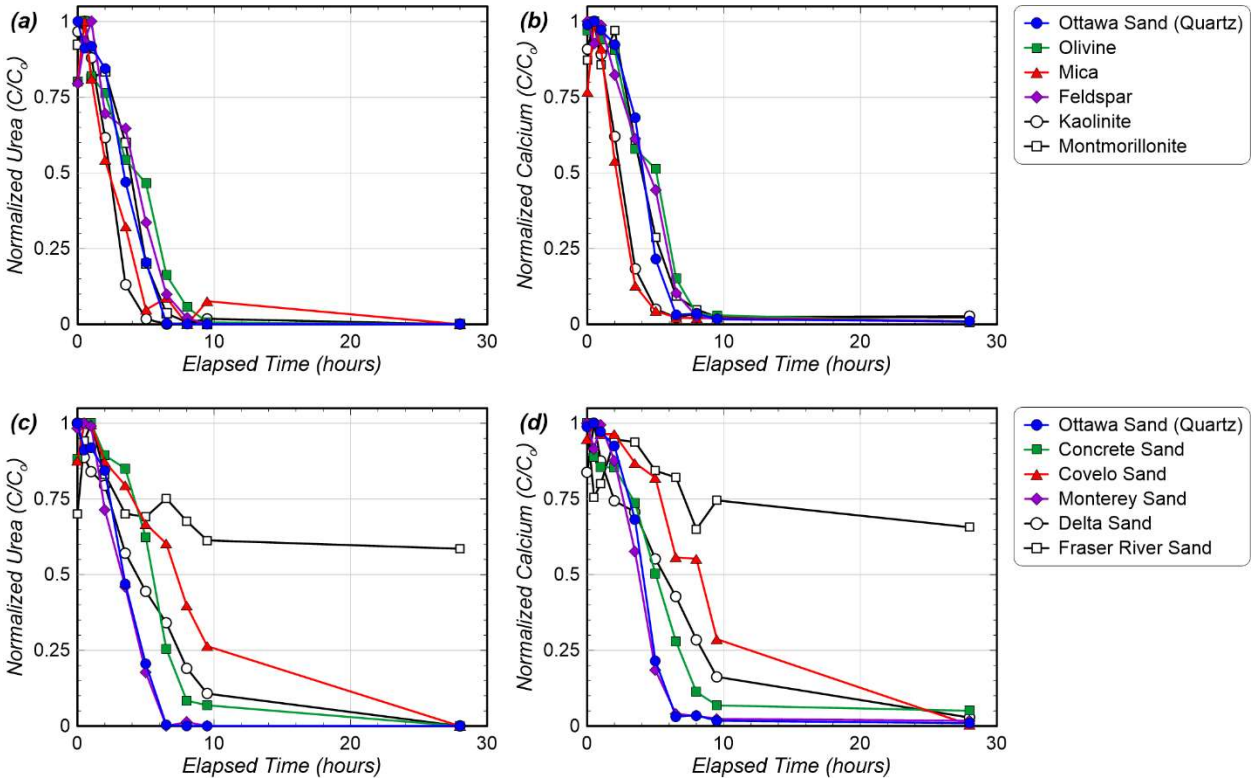

Figure 3.39 Normalized concentrations of (a, c) urea and (b, d) calcium in time for all soil varied experiments.

Following all experiments, end-state precipitates were characterized using XRD. Figure 3.40 presents the results of the S-Q analysis of the observed diffraction patterns for the (a) pure mineral and (b) sand mixture soil varied experiments. For all soil types investigated in these experiments, calcite was found to be the dominant mineral phase and was present at relative percentages exceeding 80% in all experiments. The lowest relative percentage of calcite was found in the montmorillonite specimen, which had only 5% less than the control experiment. The montmorillonite specimen also showed the highest relative percentage of vaterite at 14%. All other experiments showed relative calcite percentages between 85% and 93% and vaterite percentages of 10% or less, both of which were within the ranges observed for control experiments. While minor changes in the relative percentages across experiments were observed, overall these results suggest that none of the tested soils had dramatic effects on the mineralogy of calcium carbonate precipitated during MICP.

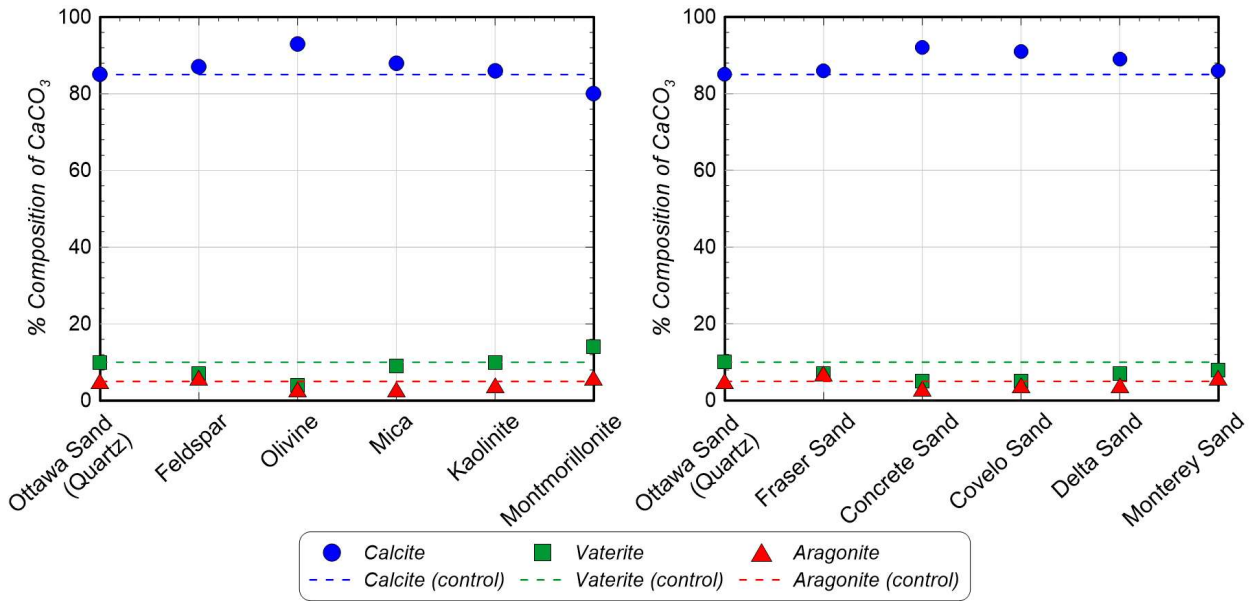

Figure 3.40 Relative $CaCO_3$ mineral content percentages for all soil varied experiments with (a) pure minerals and (b) sand mixture soils as determined by XRD analyses.

Figure 3.41 shows representative SEM images of end-state precipitate samples collected from soil varied experiments. As expected, the control specimen with Ottawa F-65 Sand displayed rhombohedral morphologies consistent with those expected for calcite (Figure 3.41a). The montmorillonite specimen also displayed mostly rhombohedral morphologies (Figure 3.41b,c), however, the sizes of the precipitated crystals were consistently smaller (diameter ≈5 μm) than those observed in the control specimen. Calcite crystals also appeared to form large precipitate structures in montmorillonite specimen, which was surprising considering the much larger particle surface area available for crystals to precipitate on. While the XRD analyses suggested that the presence of montmorillonite may have resulted in small reductions in the relative percentage of calcite precipitated, the obtained SEM images did not clearly illustrate this trend and suggested that montmorillonite largely did not affect the morphology of precipitated calcium carbonate.

The effect of kaolinite (Figure 3.41d,e) on achieved calcium carbonate precipitates was more evident from SEM imaging. In general, the morphology appeared to be consistent with the rhombohedral forms of calcite, however, these rhombohedral forms were interspersed with crystal morphologies that frequently appeared to be disordered or fragmented (Figure 3.41e). While XRD analyses similarly suggested that precipitates in the kaolinite sample were mostly composed of calcite, the distribution of obtained precipitation appeared to be much more chaotic than in the control experiment, suggesting that the presence of kaolinite may play some role in altering the distribution, shape, and overall structure of the precipitated calcium carbonate.

Lastly, SEM imaging of the Fraser River sand specimen (Figure 3.41f) revealed mostly rhombohedral morphologies consistent with calcite and had no prominent differences when compared to precipitates from the control experiment. Although inhibiting factors present in the

Fraser River Sand material dramatically influenced the kinetics of ureolysis, these factors did not appear to have substantial effects on the morphology or mineralogy of the precipitated calcium carbonate.

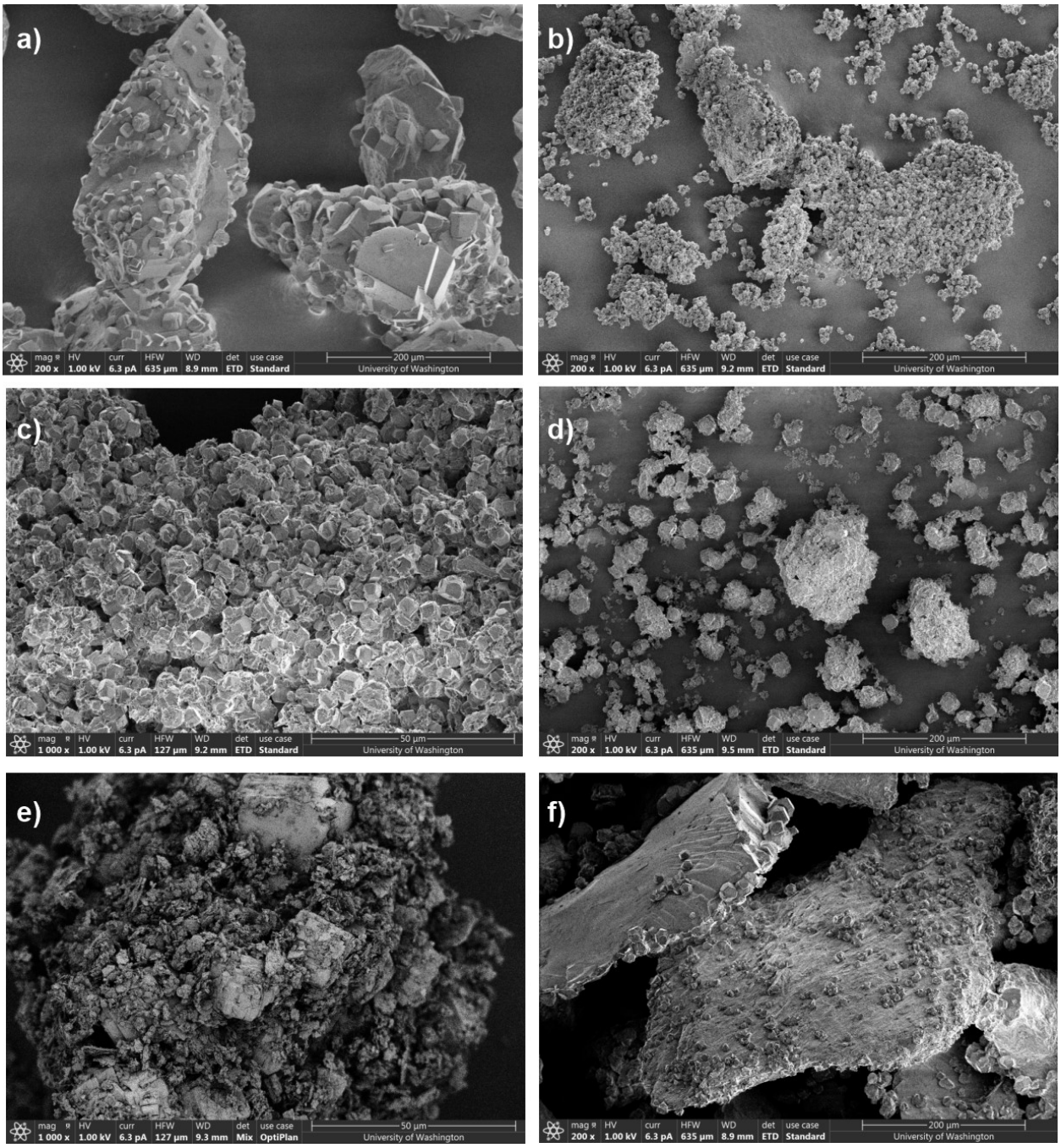

Figure 3.41 Representative SEM images of end-state precipitated from (a) Ottawa F-65 sand (control), (b, c) montmorillonite, (d, e) kaolinite, and (f) Fraser River sand samples at (a,b,d,f) 200x and (c,e) 1000x magnifications.

Chapter 4. EFFECT OF BIOLOGICAL FACTORS ON MICP

4.1 UREOLYTIC RATE

Ureolytic rates during MICP applications are controlled by both applied cell densities and per cell enzymatic activities. In order to examine the effect of changes in ureolytic rates on the MICP process three plate experiments were performed. All cementation solutions were prepared by adding 250 mM urea and calcium chloride dihydrate to deionized water. Ureolytic rates were varied by inoculating plate experiments with three different *S. pasteurii* cell densities, 1.7 x 10^7, 7.4 x 10^7, and 3.4 x 10^8 cells/mL, obtained through differences in added cell pellet volumes.

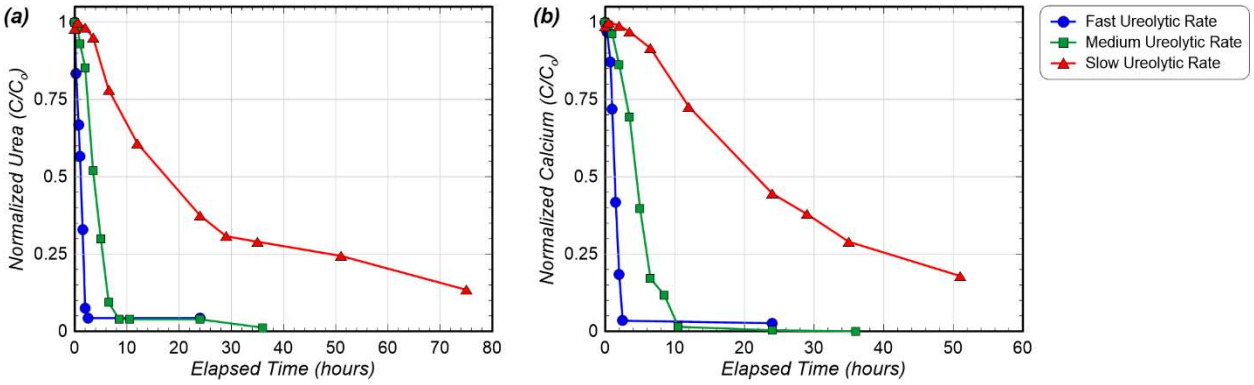

Figure 4.1 Normalized concentrations of (a) urea and (b) calcium in time for ureolytic rate varied experiments.

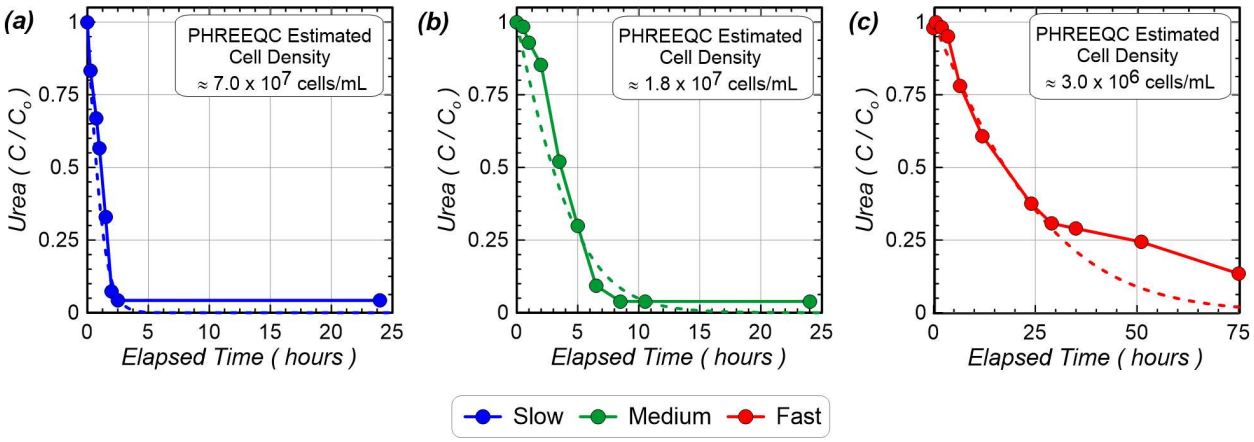

Figure 4.2 Normalized concentrations of urea in time for (a) fast, (b) medium, and (c) slow ureolytic rate experiments with calibrated PHREEQC models and estimated cell densities in text boxes.

Figure 4.1 presents normalized concentrations of urea and calcium in time for the slow, medium, and fast ureolytic rate experiments. As expected, increases in augmented cell densities resulted in increases in ureolytic rates. Similar changes in calcium consumption in time were also observed. Figure 4.2 shows comparisons of normalized concentrations of urea in time observed for ureolytic rate experiments with urea degradation trends estimated from a PHREEQC model that was calibrated to match the observed ureolytic rates over the first 25 hours of experiments. Although urea measurements showed an initial lag in the onset of urea hydrolysis as well as changes in ureolytic rates over time, the PHREEQC batch reaction model projected trends expected based upon the initial ureolytic rates while assuming a steady state cell population and whole cell kinetic parameters following Lauchnor et al. (2015). PHREEQC estimated cell densities varied near 1.5 orders of magnitude between experiments with 3.0×10^6, 1.8×10^7, and 7.0×10^7 cells/mL estimated in the slow, medium, and fast rate experiments, respectively. These cell densities were notably smaller than those estimated from OD_{600} measurements as stated previously. For the slow ureolytic rate experiments (Figure 4.2c), the PHREEQC-predicted trend

matched the experimental data well for the first 30 hours before overestimating urea degradation. The large reduction in the experimentally observed ureolytic activity at later time in the slow rate experiment may have resulted from cell death due to the absence of growth factors in these experiments as well as encapsulation of the smaller initial inoculant during precipitation.

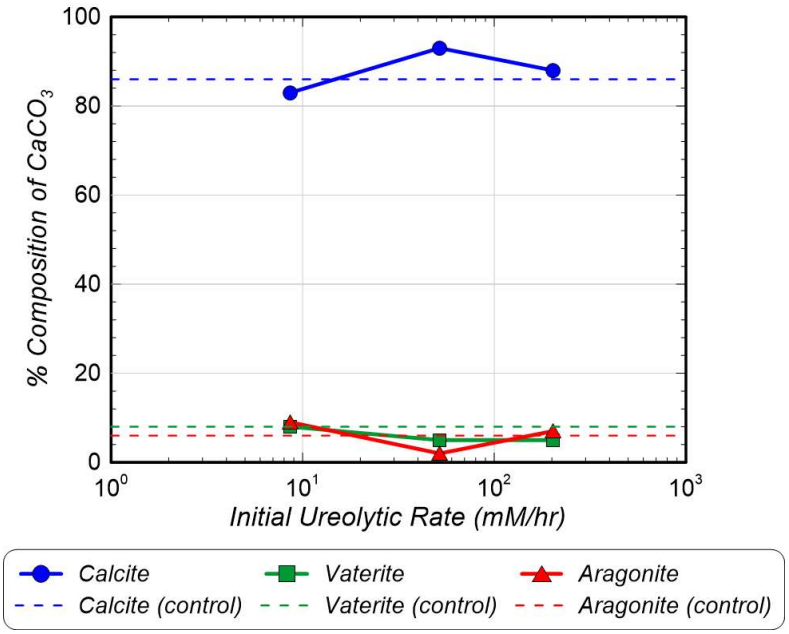

Figure 4.3 Relative $CaCO_3$ mineral content percentages for ureolytic rate varied experiments determined by XRD.

Following all experiments, resulting precipitates were analyzed using XRD. Figure 4.3 presents the results of the S-Q analysis of the observed diffraction patterns for the slow, medium, and fast ureolytic rate experiments. In all experiments, calcite was found to be the dominant mineral phase at similar relative percentages as those observed in the control. The lowest relative percentage of calcite and the highest relative percentage of vaterite was observed for the slow ureolytic rate experiment. This result was consistent with the findings of the earlier temporal experiments described in Chapter 3.1.3 of this study, wherein vaterite was found to exist at higher

abundances in experiments that did not react to completion. As shown in Figure 4.2c, the slow rate experiment was stopped with approximately 15% of the injected urea and calcium remaining in solution. The fast ureolytic rate experiment showed a slightly lower relative percentage of calcite (5%) than the medium ureolytic rate experiment, however, these relative percentages were still within the variations observed in the control experiments. The results of the XRD analyses suggest that ureolytic rates appear to have only minimal effects on the relative percentages of calcium carbonate polymorphs precipitated during MICP for the rates tested provided that changes in applied cell densities are used to obtain different rates. It remains possible that different results could have been observed if rates were inhibited at similar cell densities; however, other experiments with similar cell densities and differences in rates, such as those presented in the ammonium chloride varied experiments, also suggest that the effect of changes in ureolytic rates on obtained mineralogies are minimal for the practical timeframes considered in this study.

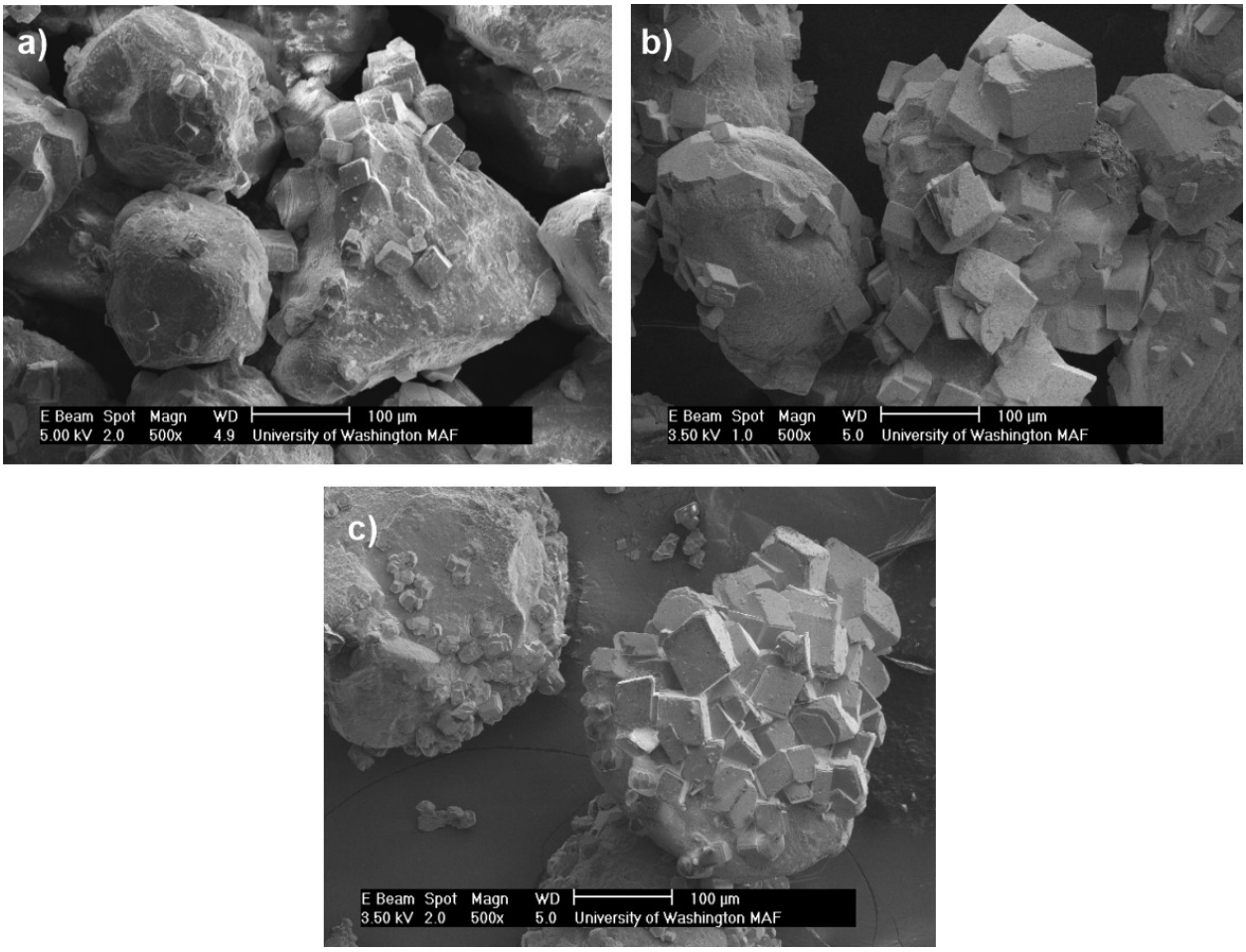

Figure 4.4 Representative SEM images of end-state precipitate samples from (a) fast, (b) medium, and (c) slow ureolytic rate experiments.

Figure 4.4 shows representative SEM images of end-state precipitates collected from the fast, medium, and slow ureolytic rate experiments. When, comparing precipitate morphologies, the fast ureolytic rate precipitates generally showed smaller crystal sizes than the medium and slow rates. These results are consistent with crystal growth theory and observation from other studies wherein ureolytic cell densities and rates were varied (Gomez et al., 2019) as well as results from the previous ammonium chloride varied experiments. In addition, fewer of the precipitates appeared to have nucleated on sand surfaces as rates increased. This result was consistent with observations during and after the fast rate experiment, wherein more precipitation appeared to exist on the

surfaces of the glass plate when compared to other ureolytic rate experiments. In addition, similar observations were also made for precipitates from experiments containing high sodium bicarbonate wherein more rapid abiotic precipitation was present. For precipitates from the fast ureolytic rate experiment, numerous surface imperfections with voids consistent with the rod-shaped form and size of *S. pasteurii* cells (approximately 1-5 μm in length and 0.2-0.5 μm in width) were also observed for some calcite crystals. Similar bacterial impressions have been reported by a variety of researchers (Gomez et al. 2018, and others). Figure 4.5 presents images from one particular region on calcite crystals which displayed these bacterial impressions.

In general, most crystal forms in all ureolytic rate samples appeared to be consistent with the rhombohedral crystal morphology expected for calcite. No spherical shapes consistent with vaterite were observed in any of the samples, although some semi-spherical negative spaces or "vaterite casts" were observed in both the slow and medium rate precipitate images.

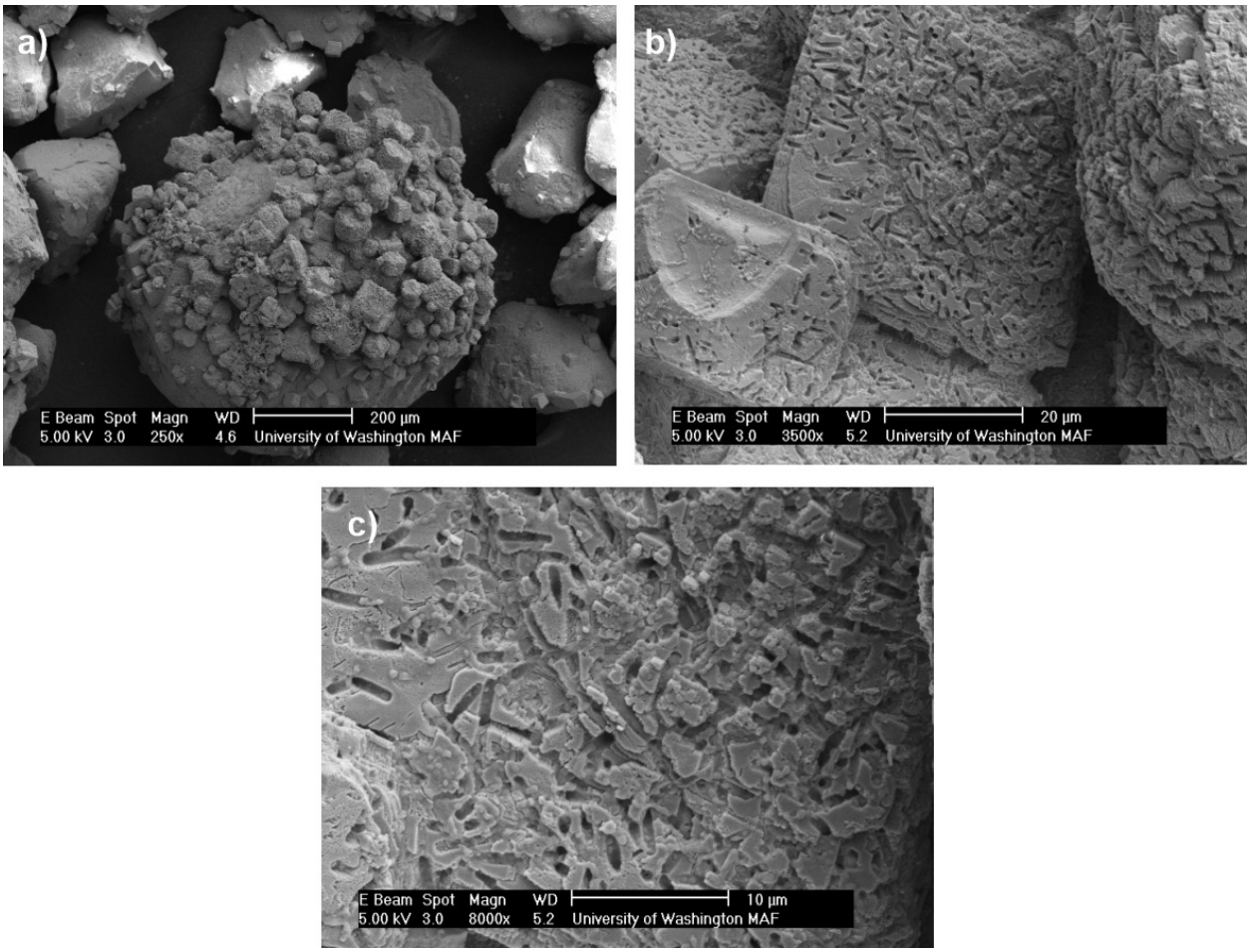

Figure 4.5 Representative SEM images of bacterial cell impressions observed in the fast ureolytic rate experiment magnified at (a) 250x, (b) 3500x, and (c) 8000x.

4.2 GROWTH FACTORS

Growth factors are often included in applied cementation solutions during MICP in order to maintain the activity of augmented or enriched ureolytic cells. Growth factors are organic compounds that provide necessary nutrients (e.g. amino acids, nitrogen, and carbon sources) for bacterial cell metabolic needs, cell maintenance, growth, and enzyme synthesis. Common growth factors included in MICP treatment solutions include yeast extract, nutrient broth, molasses, and sodium acetate. The selection of applied growth factors can have important implications for MICP

treatment costs, as the lack of sustained microbial activity may require additional augmentation or enrichment treatments and growth factor additions themselves also contribute to overall project costs. Growth factors oftentimes have definitive chemical composition and thus can be dramatically different between manufacturers and can even vary between produced batches. Despite this uncertainty, growth factors play a critical role in MICP injections. It has remained unclear, however, what effect, if any, the choice of supplied growth factors has on the MICP process and resulting precipitates.

In order to examine the effects of various commonly used growth factors on the MICP process twelve plate experiments were performed. Six solutions were prepared with either yeast extract (Fisher Scientific) or nutrient broth (BD Difco) at concentrations of 0.1, 1.0, and 5.0 g/L. Two additional solutions were prepared using molasses (Molasses Dark, Fisher Scientific) at concentrations of 0.1 and 5.0 g/L. Three solutions were also prepared with sodium acetate anhydrous (Fisher Scientific, 99.7% assay) included at concentrations of 5 mM, 50 mM, and 500 mM. Finally, an additional solution was prepared using deionized water with no growth factors added for the control experiment. Selected growth factor concentrations were intended to represent the range of concentrations used in past experiments as well as magnify the potential effects of growth factors through the application of high concentrations. All cementation solutions were prepared by adding 250 mM urea and calcium chloride dihydrate to the solutions described above. All experiments were inoculated with *S. pasteurii* at an estimated cell density of 7.2×10^7 cells/mL.

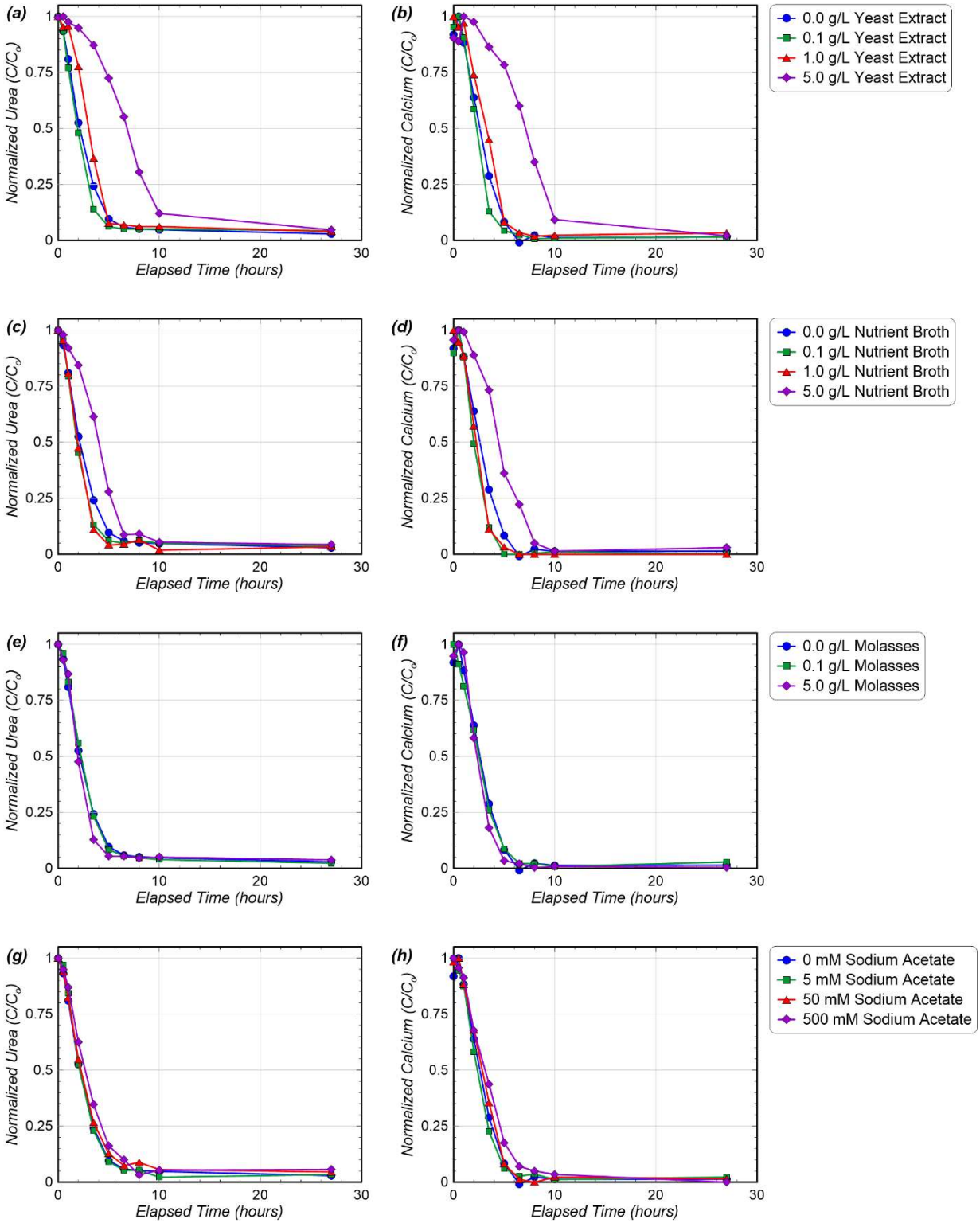

Figure 4.6 Normalized concentrations of (a, c, e, g) urea and (b, d, f, h) calcium in time for growth factor experiments containing varying (a, b) yeast extract, (c, d) nutrient broth, (e, f) molasses, and (g, h) sodium acetate concentrations.

Figure 4.6 presents normalized concentrations of urea and calcium in time for all growth factor varied experiments. Initially it was hypothesized that increases in growth factor concentrations may result in increased ureolytic activity due to higher viable cell densities and cell growth. Surprisingly, however, both the highest yeast extract and nutrient broth concentration experiments demonstrated noticeable decreases in initial ureolytic rates of 40% and 25%, respectively. This was counter to initial expectations and suggested that higher concentrations of growth factors inhibited ureolytic activities. Possible explanations for observed rate decreases include effects from increased solution ionic strengths and/or the presence of inhibiting ion concentrations. In addition, the pelleting process employed in these experiments may have reduced cell viability, thus limiting the potential for cellular growth in these experiments. It is also possible that urea hydrolysis may have proceeded much more rapidly than cell growth, thus eliminating our ability to indirectly observe the effects of cell growth using urea degradation measurements. No detectable effects on ureolytic rates were observed for the two lowest yeast extract and nutrient broth concentration experiments. It should be noted that these concentrations (0.1 to 1.0 g/L) are more typical of concentrations supplied in most MICP treatment solutions.

In contrast, experiments containing both high and low concentrations of molasses exhibited only minimal reductions in ureolytic activities. This result was somewhat surprising given the noted increase in solution density and viscosity in the 5.0 g/L molasses experiment, which was expected to potentially inhibit intercellular diffusion of urea. In addition, only minimal changes in ureolytic rates were observed for all sodium acetate concentration varied experiments.

Following all experiments, end-state precipitates were characterized using XRD. Figure 4.7 presents the results of the S-Q analysis of the observed diffraction patterns for all growth factor varied experiments. As shown, in the yeast extract, nutrient broth, and molasses experiments, the

relative percentage of calcite consistently decreased as the concentrations of these growth factors increased. In contrast, experiments containing both low and high concentrations of sodium acetate appeared to have no notable effects on the mineralogy of end-state precipitates (Figure 4.7d). Mineralogies observed in the yeast extract, nutrient broth, and molasses concentration varied experiments were therefore further compared. In the highest yeast extract concentration (5 g/L) experiment, precipitates had the lowest relative percentage of calcite (59%) while the highest nutrient broth (5 g/L) and highest molasses concentration (5 g/L) experiments had slightly larger relative percentage of calcites of 65% and 75%, respectively. At the lowest concentrations tested (0.1 g/L), precipitates from the low yeast extract experiment again had the lowest relative percentage of calcite (79%) when compared to precipitates from the low nutrient broth (84%) and low molasses (86%) experiments. These results collectively suggested that at similar concentrations, solutions containing molasses (Figure 4.7d) resulted in higher relative percentages of calcite in achieved precipitates when compared to precipitates formed in the presence of yeast extract (Figure 4.7a) and nutrient broth (Figure 4.7b). While it is difficult to attribute these results to specific differences between these growth factors, it is notable that all growth factor experiments showing detectable changes in mineralogy (e.g. yeast extract, nutrient broth, molasses) involved growth factors that contained some proteins and amino acids. Of the three growth factors listed above, molasses would be expected to contain significantly less proteins and amino acids and accordingly had more minimal effects on mineralogy. Additionally, sodium acetate contains no such proteins, and all sodium acetate experiments showed no discernible effects on mineralogy. Given the stark mineralogical differences observed between experiments, it is clear that the selection of growth factors to be used in MICP treatment solutions may be of significant practical importance.

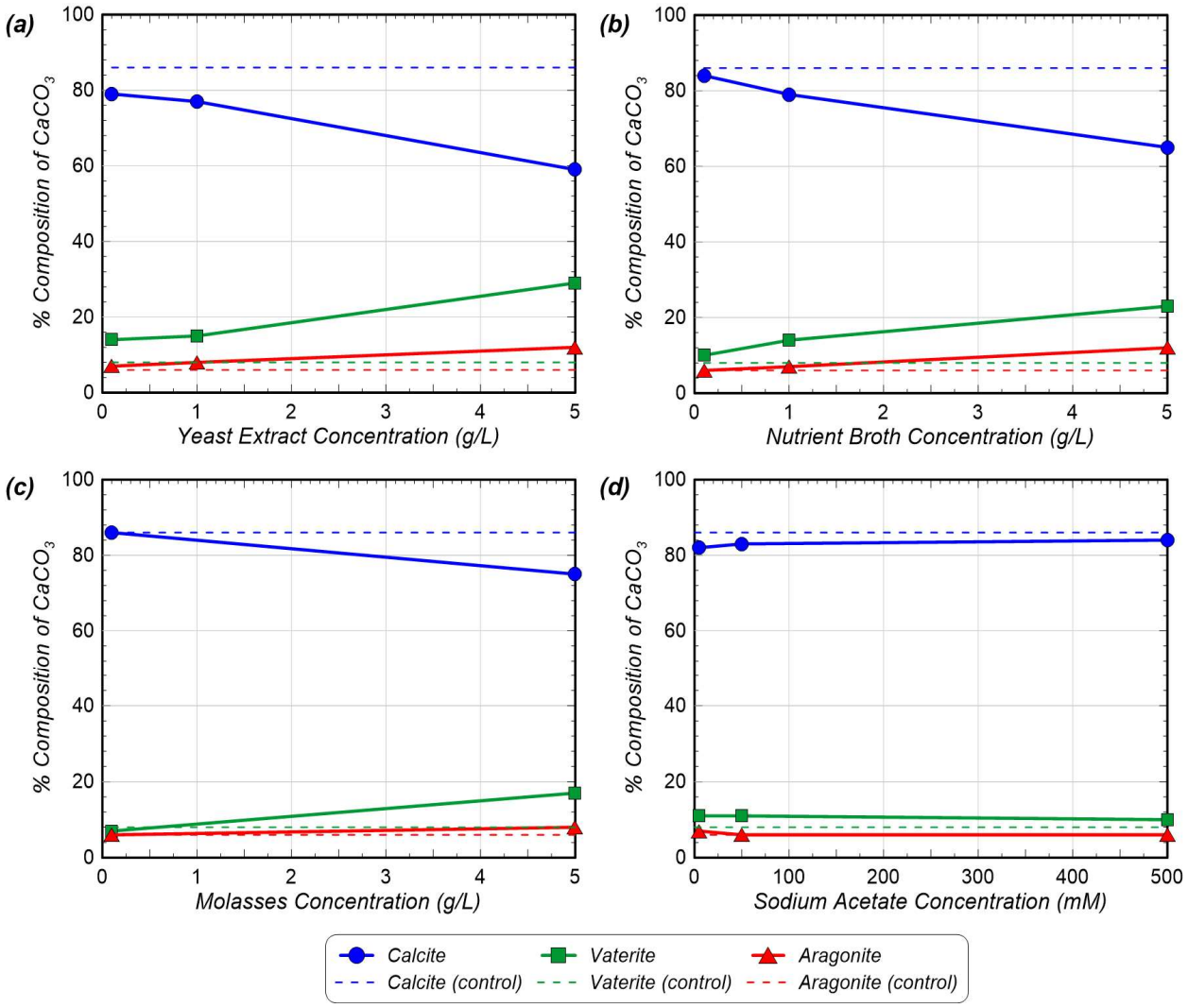

Figure 4.7 Relative $CaCO_3$ mineral percentages for (a) yeast extract, (b) nutrient broth, (c) sodium acetate, and (d) molasses concentration varied experiments as determined by XRD.

Figure 4.8 shows representative SEM images of end-state precipitates collected from yeast extract and nutrient broth concentration varied experiments. As shown, the control specimen with no added growth factors displayed rhombohedral morphologies typical of calcite (Figure 4.8a,b). Similarly, at low concentrations (0.1 g/L), precipitates from both the yeast extract (Figure 4.8c) and nutrient broth (Figure 4.8e) experiments also displayed similar rhombohedral morphologies,

in agreement with the similar mineralogies suggested by XRD analyses. At higher concentrations (5.0 g/L), however, spherical and more rounded morphologies consistent with vaterite and/or amorphous calcite minerals appeared frequently on soil particle surfaces in both the yeast extract (Figure 4.8d) and nutrient broth (Figure 4.8f) experiments. Again, these SEM images were consistent with results from XRD analyses and supported the conclusion that high concentrations (5.0 g/L) of yeast extract and nutrient broth may affect the mineralogy of precipitated calcium carbonate by decreasing relative percentages of calcite and increasing relative percentages of vaterite.

Figure 4.9 shows representative SEM images of end-state precipitates collected from the molasses concentration varied experiments. As shown, the control specimen with no added molasses again displayed rhombohedral morphologies expected for calcite (Figure 4.9a). Similar to precipitates from the low yeast extract and nutrient broth experiments, precipitates from the low molasses concentration (0.1 g/L) experiment also displayed mostly rhombohedral morphologies (Figure 4.9b). When higher concentrations (5.0 g/L) of molasses were present, however, resulting precipitates again displayed predominantly rhombohedral morphologies consistent with calcite (Figure 4.9c) in contrast to high yeast extract and nutrient broth experiments. These results were somewhat consistent with the XRD analyses which suggested that high concentrations of molasses (5.0 g/L) may not affect the mineralogy of produced calcium carbonate precipitates as much as high concentrations of yeast extract or nutrient broth (5.0 g/L).

Figure 4.10 presents representative SEM images of end-state precipitates from the sodium acetate concentration varied experiments. As shown, again the control specimen with no added sodium acetate displayed rhombohedral morphologies expected for calcite (Figure 4.10a). Precipitates produced in both the medium (50 mM) and high (500 mM) concentration sodium

acetate experiments also displayed morphologies similar to the control, with abundant rhombohedral crystals (Figure 4.10b,c). These results agreed with XRD analyses which suggested that the presence of sodium acetate concentrations up to 500 mM may have little effects on the mineralogy of produced calcium carbonate precipitates.

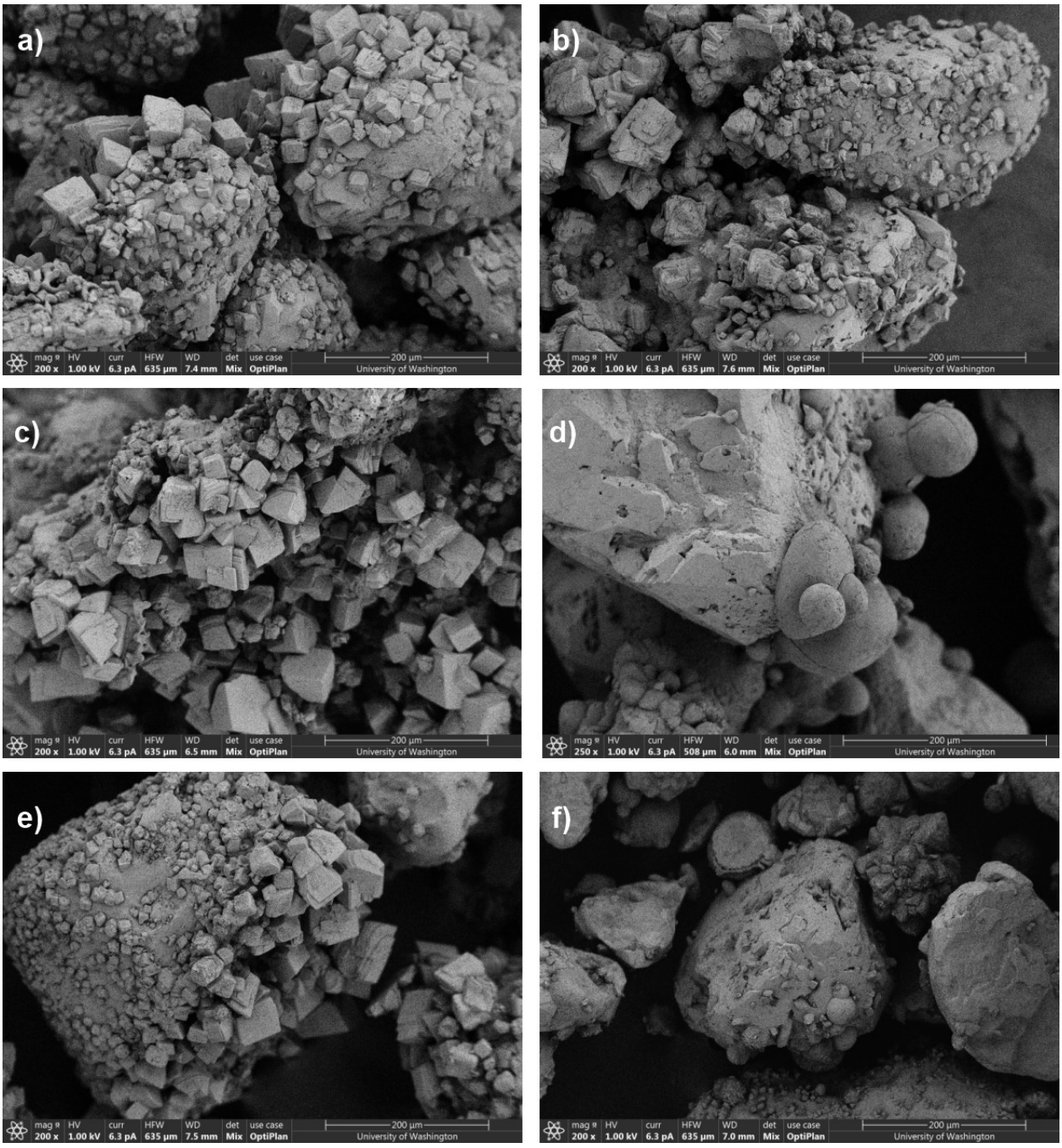

Figure 4.8 Representative SEM images of samples from the (a, b) control, (c) 0.1 g/L yeast extract, (d), 5.0 g/L yeast extract, (e) 0.1 g/L nutrient broth, and (f) 5.0 g/L nutrient broth experiments.

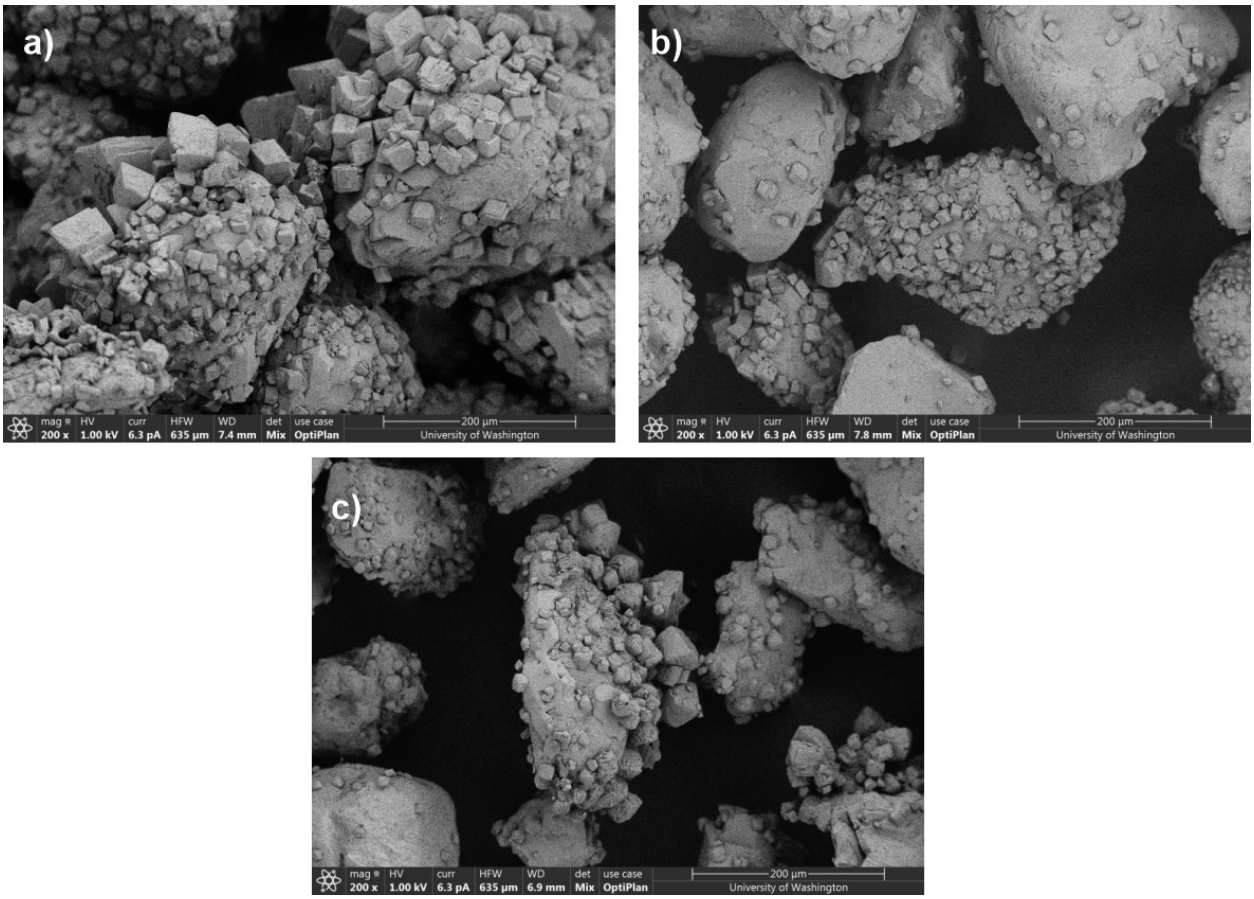

Figure 4.9 Representative SEM images of end-state precipitates from the (a) control, (b) 0.1 g/L molasses, and (c) 5.0 g/L molasses experiments.

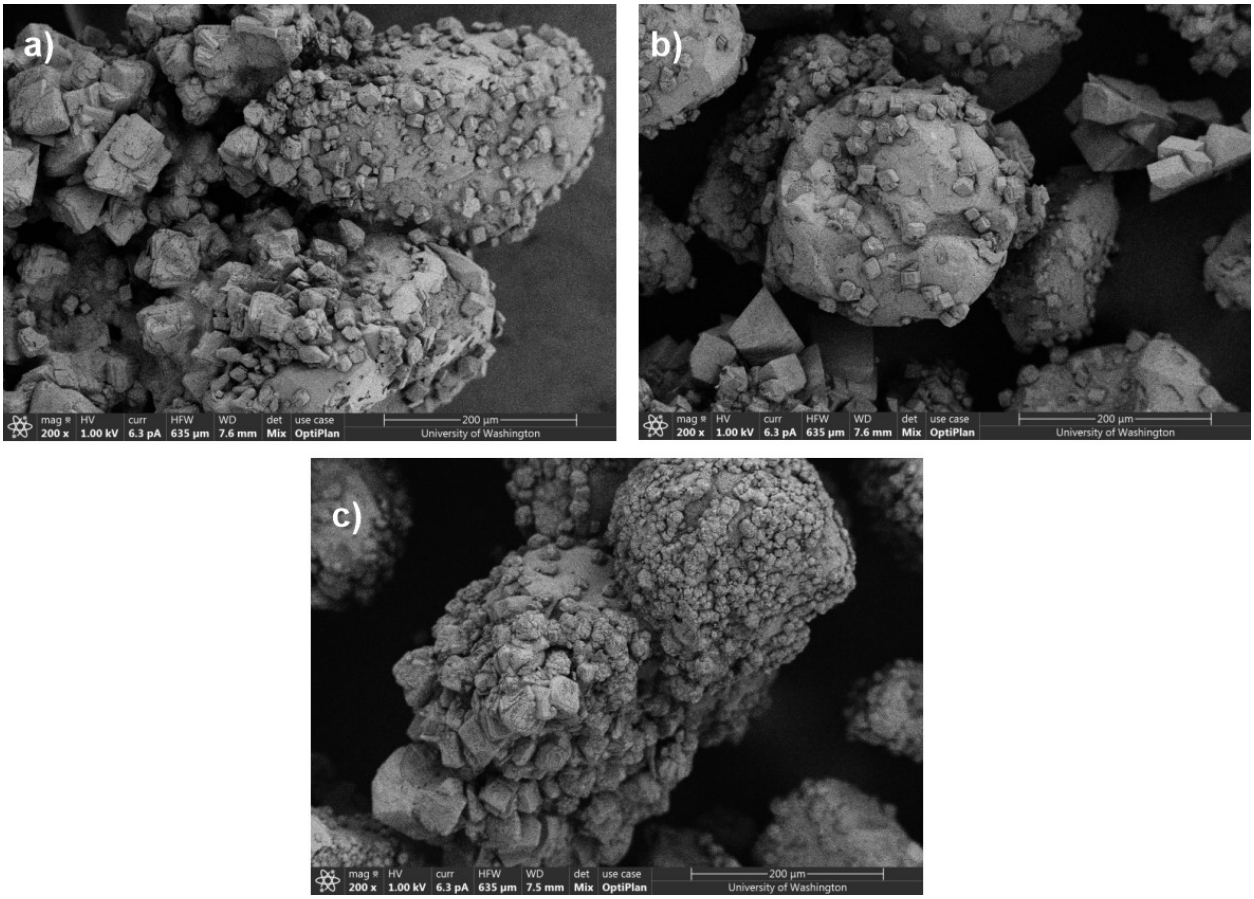

Figure 4.10 Representative SEM images of end-state precipitates from the (a) 0 mM, (b) 50 mM, and (c) 500 mM sodium acetate experiments.

4.3 Bacterial Concentration with Bacillus subtilis

When MICP is applied to natural soil sites, ureolytic bacteria are either supplied and injected (augmented) or enriched *in-situ* (stimulated). In both cases, however, the resulting ureolytic bacterial population will necessarily encounter the presence of many other soil microorganisms. It has been estimated that geotechnically-relevant natural soils often contain between 10^6 and 10^{11} cells per kilogram of soil (Whitman et al., 1998). The presence of these microbes cannot be avoided and as suggested by previous experiments containing varying ureolytic cell densities, changes in bacterial cell densities during MICP may impact the morphology, size, and/or appearance of

precipitated calcium carbonate minerals. It is hypothesized the presence of bacterial cells during MICP may offer preferred nucleation sites for calcium carbonate crystals due to the reduction of activation energies needed to initiate precipitation. Thus, changes in total bacterial cell densities may alter the distribution of resulting precipitates and potentially even the engineering properties of bio-cementation improved soils. For example, changes in crystal size may impact soil frictional resistances and volumetric tendencies during shearing and changes in mineral distributions on particle surfaces and contacts may influence observed stiffnesses and inter-particle cohesion.

In order to examine the effect of non-ureolytic bacterial cell densities on the MICP process, three plate experiments were performed. In several of these experiments, *Bacillus subtilis* (*B. subtilis)* ATCC 23857 cells were also added to examine the impact of the presence of additional bacterial cells on MICP. *B. subtilis* are non-ureolytic, rod-shaped, Gram-positive bacteria of similar size to *S. pasteurii* that can be commonly found in soils. *B. subtilis* cultures were grown, frozen, and pelleted using protocols consistent with the preparation of *S. pasteurii* cells as described in Chapter 2.1.2 with the exception of the growth media used, which instead consisted of 23 g/L nutrient broth (Difco) in deionized water. Since *B. subtilis* is non-ureolytic, it was expected to have no effect on observed ureolytic activity and be present solely as a passive "spectator cell" during all precipitation events. *B. subtilis* is also commonly used as a model organism for studying the impact of Gram-positive bacterial cells for a variety of applications (Völker and Hecker 2005). 24 hours before experiments, each Ottawa F-65 sand sample was augmented with *S. pasteurii* at an estimated cell density of 6.8×10^7 cells/mL in the same manner as previous experiments. In addition, *B. subtilis* cells were also added to two of these sand samples at cell densities corresponding to 1x and 25x that of the augmented *S. pasteurii* cells. Similar to

other experiments, all cementation solutions were prepared by adding 250 mM urea and calcium chloride dihydrate to deionized water.

Figure 4.11 presents normalized concentrations of urea and calcium in time for all *B. subtilis* augmented experiments. As shown, no appreciable changes in ureolytic rates were observed as *B. subtilis* cell densities increased, as expected. Similarly, almost no effects on calcium carbonate precipitation kinetics were observed. Overall, the results suggested that increasing non-ureolytic spectator cell concentrations (specifically *B. subtilis)* during MICP had only minimal effects on ureolytic and calcium carbonate precipitation rates.

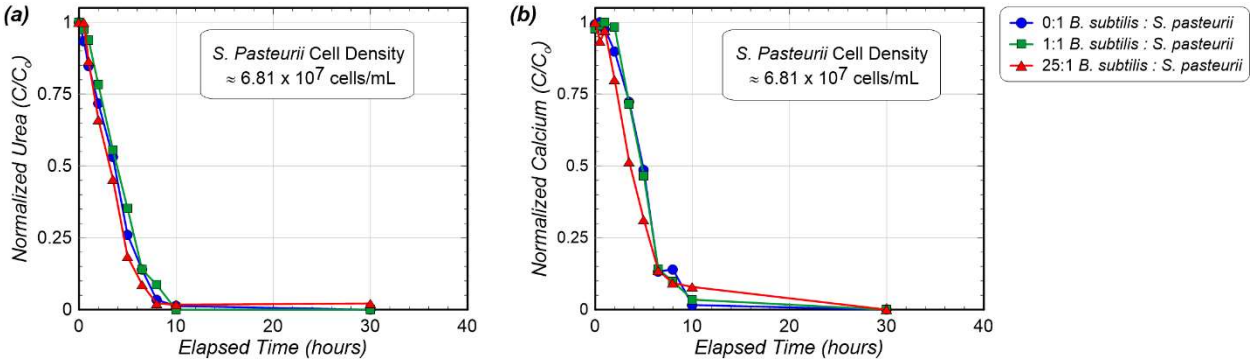

Figure 4.11 Normalized concentrations of (a) urea and (b) calcium in time for experiments with varying *B. subtilis* cell densities augmented at ratios of 0:1, 1:1, and 25:1 to *S. pasteurii* cells, which were supplied at a constant cell density of 6.8 x 10^7 cells/mL.

Following all experiments, end-state precipitates were characterized using XRD. Figure 4.12 presents the results of the S-Q analysis of the observed diffraction patterns for the *B. subtilis* cell density varied experiments. As shown, precipitates from both experiments wherein *B. subtilis* cells were added had a lower relative percentage of calcite and higher relative percentage of vaterite when compared to the control experiment with no added *B. subtilis*. Decreases in calcite relative percentages were not linear with *B. subtilis* cell densities, however, as precipitates from the 1:1 *B.*

subtilis to *S. pasteurii* ratio specimen indicated a slightly lower calcite relative percentage (82%) when compared to those from the 25:1 *B. subtilis* to *S. pasteurii* ratio specimen (85%). Meanwhile precipitates in the control specimen indicated a calcite relative percentage of 92% that was consistent with control experiments. These results suggest that increases in total cell densities may influence the mineralogy of calcium carbonate precipitates formed during MICP, although only to a minor extent.

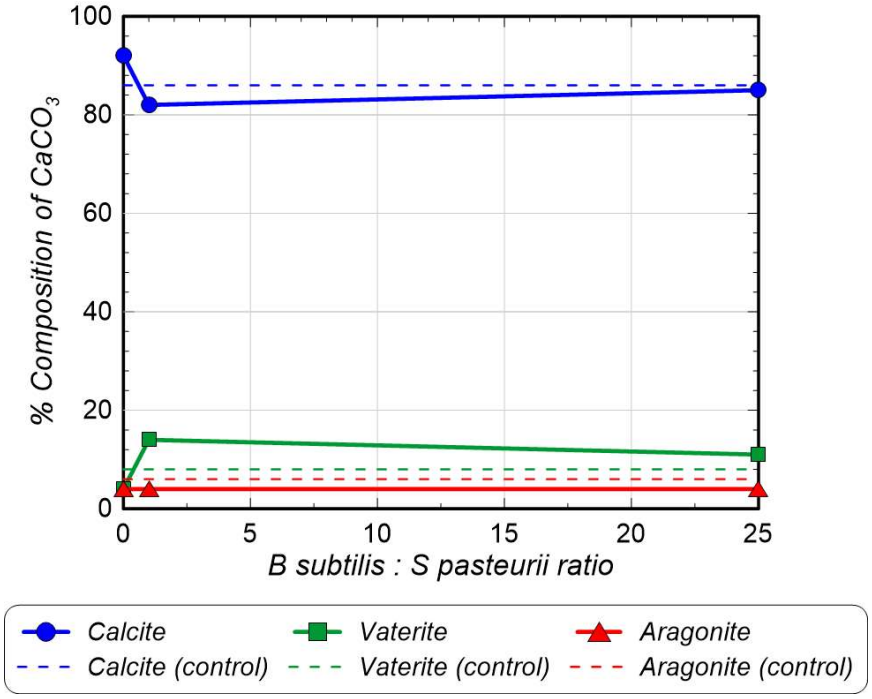

Figure 4.12 Relative $CaCO_3$ mineral content percentages for varying *B. subtilis* cell density experiments determined from XRD analyses, wherein *B. subtilis* was applied at cell density ratios of 0:1, 1:1, and 25:1 to *S. pasteurii* cells. In all experiments, *S. pasteurii* cells were present at an estimated cell density of 6.8 x 10^7 cells/mL.

Figure 4.13 shows representative SEM images of end-state precipitates collected from experiments wherein *B. subtilis* cells were present at various ratios with respect to a consistent *S. pasteurii* cell inoculant. As shown, the control specimen containing no added *B. subtilis* cells

displayed similar rhombohedral morphologies expected for calcite (Figure 4.13a). Precipitates from the 1:1 *B. subtilis* to *S. pasteurii* cell ratio experiment also displayed mostly rhombohedral crystals (Figure 4.13b) with some rounded morphologies and bacterial impressions visible on crystal surfaces at high magnifications (Figure 4.13e) that were similar to the impressions previously observed in the high ureolytic rate experiment. SEM imaging of precipitates from the higher 25:1 *B. subtilis* to *S. pasteurii* cell density ratio experiment revealed more dramatic changes in precipitate morphology than the previous XRD analyses suggested. In this experiment, precipitates exhibited crystal morphologies that were much more poorly-formed (Figure 4.13c), with frequently observed rounded, broken, and possibly amorphous morphologies. Small, rounded, unusual crystal forms were also visible at higher magnifications (Figure 4.13f). Surprisingly, however, well-defined rod-shaped bacterial impressions were not readily identifiable in this specimen despite having higher cell densities than the 1:1 *B. subtilis* to *S. pasteurii* cell density ratio experiment. In addition to these rather unusual morphologies, large calcium carbonate crystal aggregations were observed that appeared to have been precipitated in free solution rather than on soil particle surfaces (Figure 4.13d). Similar crystal clusters were not observed in any other experiments performed during the course of this research, suggesting that calcium carbonate may be more likely to precipitate away from soil surfaces in the presence of high cell densities. It is possible that individual cells or cell clusters may have acted as preferred nucleation sites for precipitation, thus reducing precipitation magnitudes existing on soil particle surfaces. These images also suggest that the morphology of precipitates formed in this manner may differ dramatically from the typical morphology observed for calcite when precipitated on soil particle surfaces. These observations were especially notable given that the XRD analyses suggested that precipitate mineralogies were similar between all experiments.

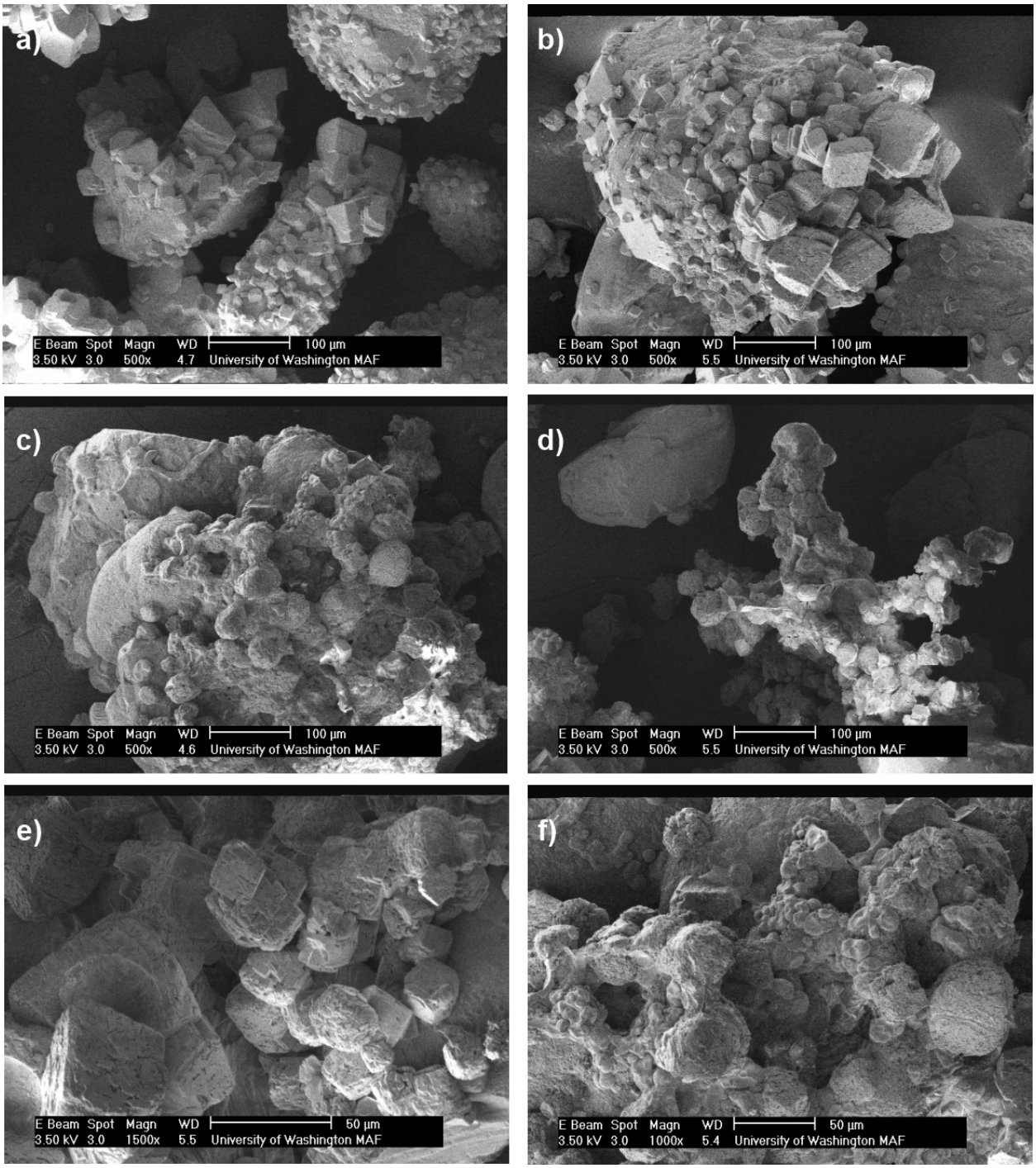

Figure 4.13 Representative SEM images of end-state precipitates from (a) 0:1, (b, e) 1:1, and (c, d, f) 25:1 *B. subtilis* to *S. pasteurii* cell density ratio experiments wherein the supplied *S. pasteurii* cell density was 6.8 x 10^7 cells per mL in all experiments.

4.4 SODIUM ALGINATE

In addition to the presence of other cells, extracellular polymeric substances (EPS) may also exist in natural soils before and during MICP treatments. EPS are natural polymers composed of polysaccharides and other proteins secreted by microorganisms which act to protect cells, aid in the recovery of nutrients, and enable diverse microbial communities to co-exist. EPS are typically gum-like in texture and may restrict enzyme activity, limit locomotion of cells, and/or influence mineral precipitation events, making the effect of the presence of EPS during MICP potentially important. Additionally, many past researchers have suggested that MICP may be actually mediated by *S. pasteurii* biofilm communities (Cuthbert et al. 2012, Philips et al. 2013, and others). In order to study the effects of biofilms for a variety of purposes, sodium alginate has been commonly used as an analog substance for bacterial EPS and can be extracted directly from the cell walls of brown algae (Ye et al., 2005, and others).

In order to examine the effects of changes in EPS concentrations on the MICP process three plate experiments were performed with varying concentrations of sodium alginate. All cementation solutions were first prepared by adding 250 mM urea and calcium chloride dihydrate to deionized water. Low and high sodium alginate concentration solutions were then created by adding either 2 g/L or 20 g/L powdered sodium alginate (alginic acid sodium salt powder, Sigma-Aldrich) to solutions that were subsequently mixed thoroughly using a vortexer. Concentrations of sodium alginate exceeding 20 g/L were found to be too viscous to pass through centrifuge filters used for aqueous solution sampling and therefore were not examined in these experiments. Noticeable differences in solution viscosities were observed for cementation solutions containing both low and high concentrations of sodium alginate. All experiments contained *S. pasteurii* cells at an estimated cell density of 6.8×10^7 cells/mL.

Figure 4.14 presents normalized concentrations of urea and calcium in time for all sodium alginate concentration varied experiments. Surprisingly, no appreciable changes in ureolytic rates were observed as sodium alginate concentrations were increased despite the observed changes in solution viscosities. These results suggested that for the concentrations tested, sodium alginate additions had only minimal effects on ureolytic activities and precipitation rates during MICP. While the high sodium alginate concentration experiment included as much sodium alginate as could be reasonably tested in our experiments, it remains possible that comparable EPS concentrations could be encountered locally in areas where significant biofilms are present such as microbial mats (Decho et al., 2005; Wingender et al., 1999)

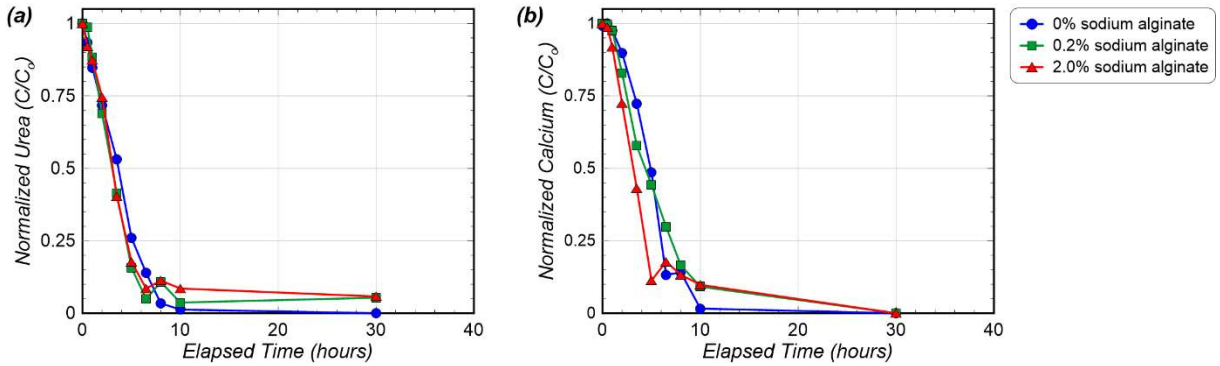

Figure 4.14 Normalized concentrations of (a) urea and (b) calcium in time for experiments containing varying concentrations of sodium alginate, a model extracellular polymeric substance.

Following all experiments, end-state precipitates were characterized using XRD. Figure 4.15 presents the results of the S-Q analysis of the observed diffraction patterns for the sodium alginate concentration varied experiments. Although calcite was found to be the dominant mineral phase in all three experiments, a dramatic reduction in the relative percentage of calcite near 20% was observed for precipitates from both the low and high sodium alginate concentration experiments. This reduction in calcite corresponded with a large increase in vaterite with relative percentages

of 20% and 22% observed in precipitates from the low and high sodium alginate experiments, respectively. A minor increase in aragonite relative percentages to 7% was also observed in both experiments. The dramatic changes in mineralogy observed in the presence of sodium alginate were some of the largest changes observed in all batch experiments performed in this study. These results suggested that the presence of sodium alginate and other EPS may significantly affect the mineralogy of calcium carbonate minerals produced during MICP, with decreases in calcite relative percentages and increases in vaterite and aragonite relative percentages expected at higher EPS concentrations.

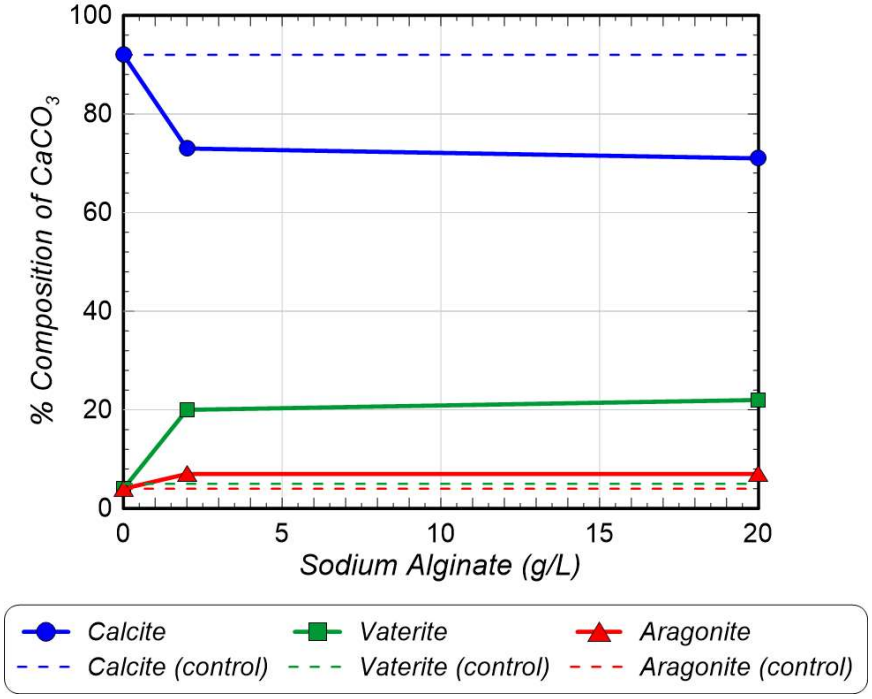

Figure 4.15 Relative $CaCO_3$ mineral content percentages for experiments with varying concentrations of sodium alginate determined from XRD analyses.

Figure 4.16 presents representative SEM images of end-state precipitates collected from the sodium alginate concentration varied experiments. As shown, the control specimen with no added sodium alginate displayed rhombohedral morphologies expected for calcite (Figure 4.16a).

Precipitates from both low (Figure 4.16b) and high (Figure 4.16c,d) sodium alginate concentration experiments, however, exhibited greater spherical morphologies indicative of the presence of vaterite. In addition, other rounded forms that were not clearly spherical were also observed in precipitates from the high sodium alginate (2.0 g/L) concentration specimen and appeared to be indicative of the presence of either amorphous calcium carbonate or EPS residues. In general, these images were consistent with the results of the XRD analyses, which suggested that higher relative percentages of vaterite could be found in both the low and high sodium alginate experiments. Collectively, these results suggest that EPS may have a stabilizing effect on precipitated vaterite. Similar observations have been made in previous mineral studies involving the presence of proteins and other organic compounds (Braissant et al. 2003).

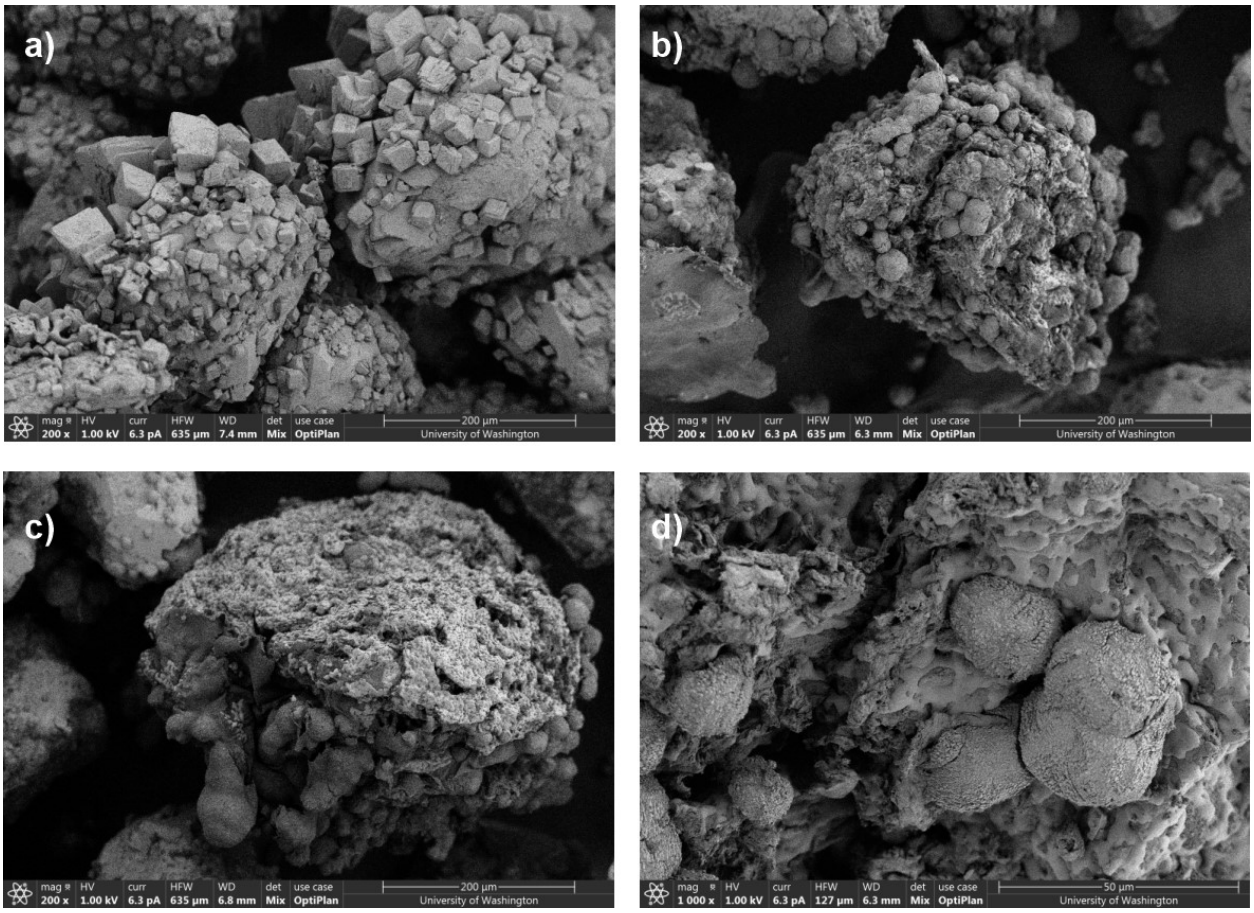

Figure 4.16 Representative SEM images of end-state precipitates from (a) 0%, (b) 0.2%, and (c,d) 2.0% sodium alginate concentration experiments at various magnifications.

4.5 EICP

Enzymatically-induced carbonate precipitation (EICP) is a soil improvement process wherein free urease enzymes are used to facilitate urea hydrolysis for the production of calcium carbonate minerals. These enzymes are oftentimes extracted from biological sources (e.g. jack bean plants) and allow for increases in urea hydrolysis rates by eliminating cell diffusion limitations. Several past studies have suggested that the engineering properties of bio-cementation produced using EICP may be different than that resulting from MICP. For example, Almajed (2017) found that EICP-treated sands demonstrated higher strengths than MICP-treated sands at similar calcium

carbonate contents. Nafisi et al. (2019) found that MICP bio-cemented sands exhibited higher shear strengths and dilative volumetric behaviors than EICP bio-cemented sands at the same shear wave velocity, as well as had precipitate morphologies that were more consistent with calcite. Further investigation of calcium carbonate precipitates produced by MICP and EICP treatment approaches for otherwise identical conditions may improve our understanding of expected differences in engineering behaviors. Similar to MICP, investigating the effects of different biological factors on the EICP process may also be important, as field-scale implementations of EICP may also be conducted in environments wherein other cells and/or biofilms are present. The use of free enzymes to mediate reactions in the presence non-ureolytic *B. subtilis* cells was also examined to better understand the role of urease enzymes and bacterial cells during MICP in a never before investigated decoupled manner.

In order to compare bio-cementation formed during EICP to that formed during MICP, as well as to investigate the influence of various biological factors on EICP, five plate experiments were performed. One experiment involved the MICP control condition, which contained *S. pasteurii* cells at an estimated cell density of 6.81 x 10^7 cells/mL. Another EICP experiment was prepared identically to the MICP control but included the addition of free urease enzymes rather than augmented *S. pasteurii* cells. Three other EICP experiments included the addition of either (1) 6.8 x 10^7 cells/mL of *B. subtilis* cells, (2) 2 g/L sodium alginate, or (3) 6.8 x 10^7 cells/mL of *B. subtilis* cells and 2 g/L sodium alginate. No *S. pasteurii* cells were added to any of the EICP experiments and all urease enzymes were applied at similar concentrations intended to match the initial ureolytic rate present in the MICP experiment. All cementation solutions were prepared by adding 250 mM urea and calcium chloride dihydrate to deionized water. For all EICP experiments containing *B. subtilis* cells, bacterial cells were added to sand samples 24 hours prior to

experiments. In all EICP experiments, 40 mg of jack bean urease (urease derived from Canavalia ensiformis, type III, powder, 40150 units/g solid, Sigma-Aldrich) was added to prepared cementation solutions immediately prior to starting experiments. Ureolytic rate calibration tests were conducted prior to performing EICP plate experiments in order to match initial urea degradation rates to the MICP control experiment. Results from calibration tests indicated that 1 mg of jack bean urease would liberate approximately 35 micromoles of urea per minute.

Figure 4.17 presents normalized concentrations of urea and calcium in time for all EICP experiments. As shown, neither the addition of *B. subtilis* cells or sodium alginate had significant effects on observed ureolytic activity or precipitation rates. These results agreed well with previously discussed MICP experiments receiving similar additions and suggested that the effect of spectator cells and sodium alginate on EICP could be studied without any large differences in ureolytic rates.

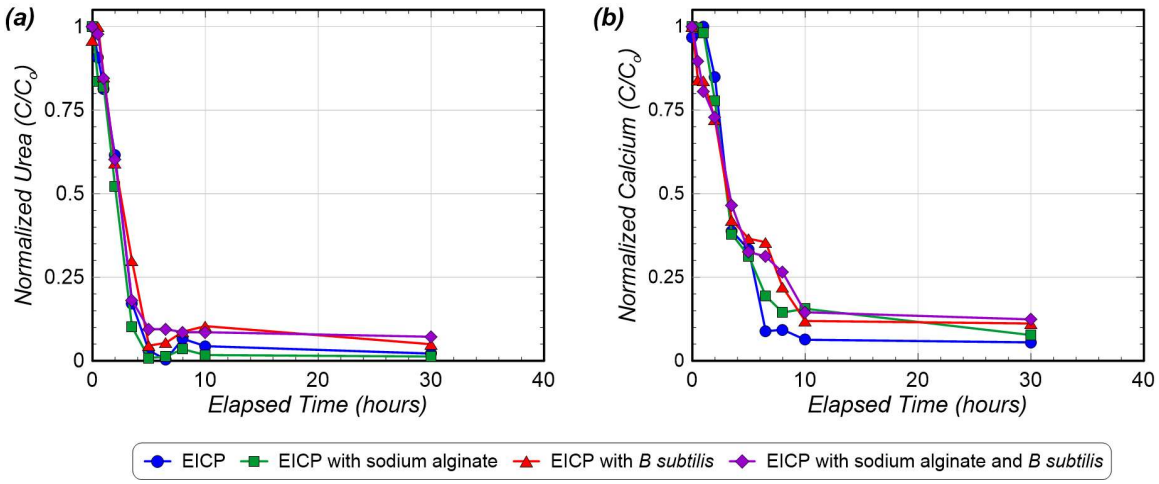

Figure 4.17 Normalized concentrations of (a) urea and (b) calcium in time for EICP experiments with various combinations of supplied sodium alginate (2 g/L) and additions of *B. subtilis* cells (cell density of 6.8 x 10^7 cells/mL).

Following all experiments, end-state precipitates were characterized using XRD. Figure 4.18 presents the results of the S-Q analysis of the observed diffraction patterns for all EICP experiments. As shown, for identical concentrations of urea and calcium and similar urea degradation rates, bio-cementation using EICP resulted in considerably lower relative percentages of calcite (79%) when compared to MICP (92%). In addition, both aragonite and vaterite relative percentages increased in the EICP experiment when compared to the MICP control experiment. Relative percentages of calcite further decreased in precipitates from EICP experiments containing *B. subtilis* cells (71%), sodium alginate (77%), and both *B. subtilis* cells and sodium alginate (67%). Similar mineralogical observations were made for previous MICP experiments when *B. subtilis* cells and sodium alginate were added. Relative percentages of calcite decreased more dramatically, however, with increases in *B. subtilis* cells than sodium alginate in EICP experiments, whereas the opposite effect was observed in the previous MICP experiments. The mechanisms responsible for this are not fully understood at this time. These results suggest that small changes in existing bacterial cell densities may have significant effects on the mineralogy of precipitates obtained using EICP. The observed decreases in calcite relative percentages for EICP experiments containing sodium alginate were also generally consistent with the results of the MICP experiments. The mineralogy of precipitates from the EICP experiment with both *B. subtilis* cells and sodium alginate added had the lowest relative percentage of calcite of all EICP experiments completed in this study, suggesting that these effects may be compounded when both factors are present. When compared to other MICP experiments, this sample also yielded one of the lowest relative percentages of calcite observed over the entire course of this study. In general, decreases in calcite relative percentages were coupled with corresponding increases in vaterite relative percentages for all experiments involving EICP.

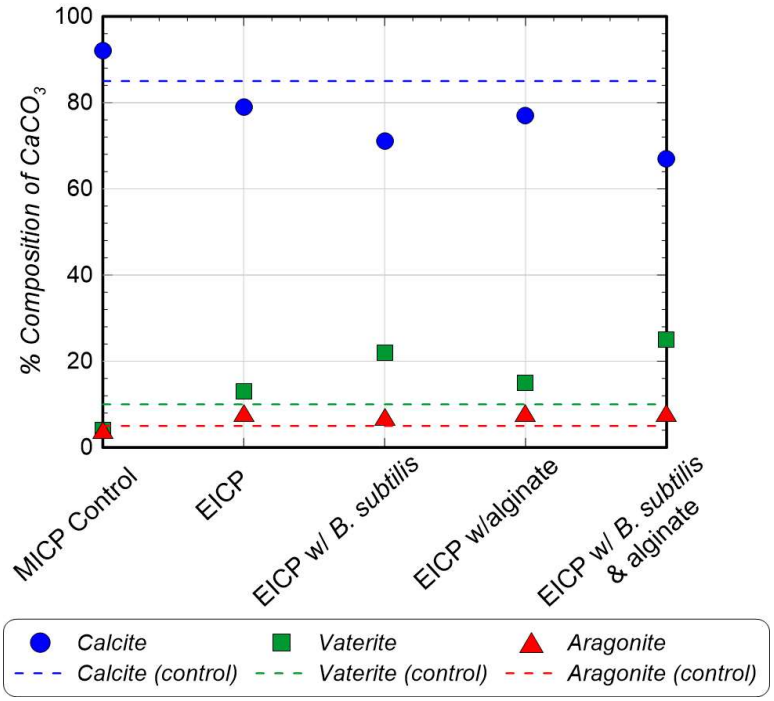

Figure 4.18 Relative $CaCO_3$ mineral content percentages for the MICP control experiment and all other EICP experiments with various combinations of supplied sodium alginate (2 g/L) and additions of *B. subtilis* cells (cell density of 6.8 x 10^7 cells/mL).

Figure 4.19 shows representative SEM images of end-state precipitates from the MICP control experiment and the EICP experiment with no other additions. As shown, the MICP control specimen displayed rhombohedral morphologies expected for calcite (Figure 4.19a). The EICP specimen, on the other hand, displayed both rhombohedral forms as well as more rounded crystals (Figure 4.19b). In addition, much of the precipitated calcium carbonate appeared to be disordered, with broken or chaotic forms, possibly suggesting the presence of amorphous calcium carbonate (Figure 4.19c). Some crystal forms were very unusual in comparison to the precipitates observed in other MICP experiments over the course of this research. For example, "rabbit-ear"-like precipitates were observed in some instances (Figure 4.19d). Similar to the precipitates from the MICP seawater experiments, it was difficult to visually identify many of the crystalline structures

present in the EICP experiment. Overall, the SEM images of the EICP experiment revealed more dramatic changes in morphology than the XRD analyses suggested.

Figure 4.20 shows representative SEM images of end-state precipitates from EICP experiments with *B. subtilis* cell (6.8 x 10^7 cells/mL) and sodium alginate (2 g/L) additions. All EICP specimens displayed similar crystal morphologies as the EICP specimen which had no additions. Many chaotic, broken, and amorphous forms among some rhombohedral crystals were observed. The two EICP experiments that included sodium alginate additions displayed noticeably more rounded morphologies and fewer rhombohedral morphologies (

Figure 4.20b,c) than the experiments with only *B. subtilis* cell additions (

Figure 4.20a). These trends were similar to those observed in the MICP experiments involving *B. subtilis* cell and sodium alginate additions. Overall, these observations generally supported the results of the XRD analyses and suggested that biological additions may further alter the morphology of EICP precipitates, resulting in more rounded forms, possibly indicative of the presence of vaterite, as well as more amorphous morphologies.

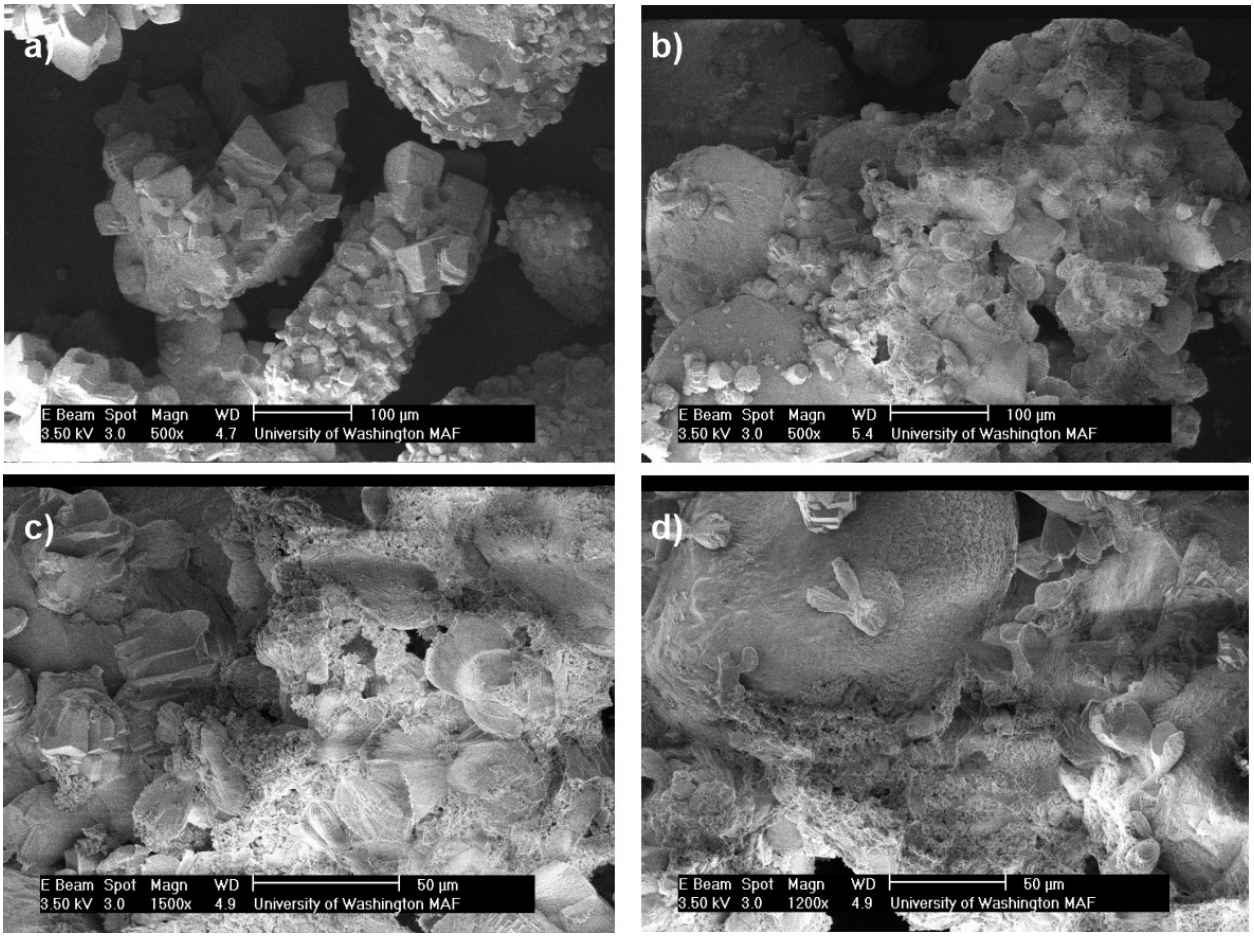

Figure 4.19 Representative SEM images of end-state precipitates from (a) MICP and (b,c,d) EICP experiments at various magnifications.

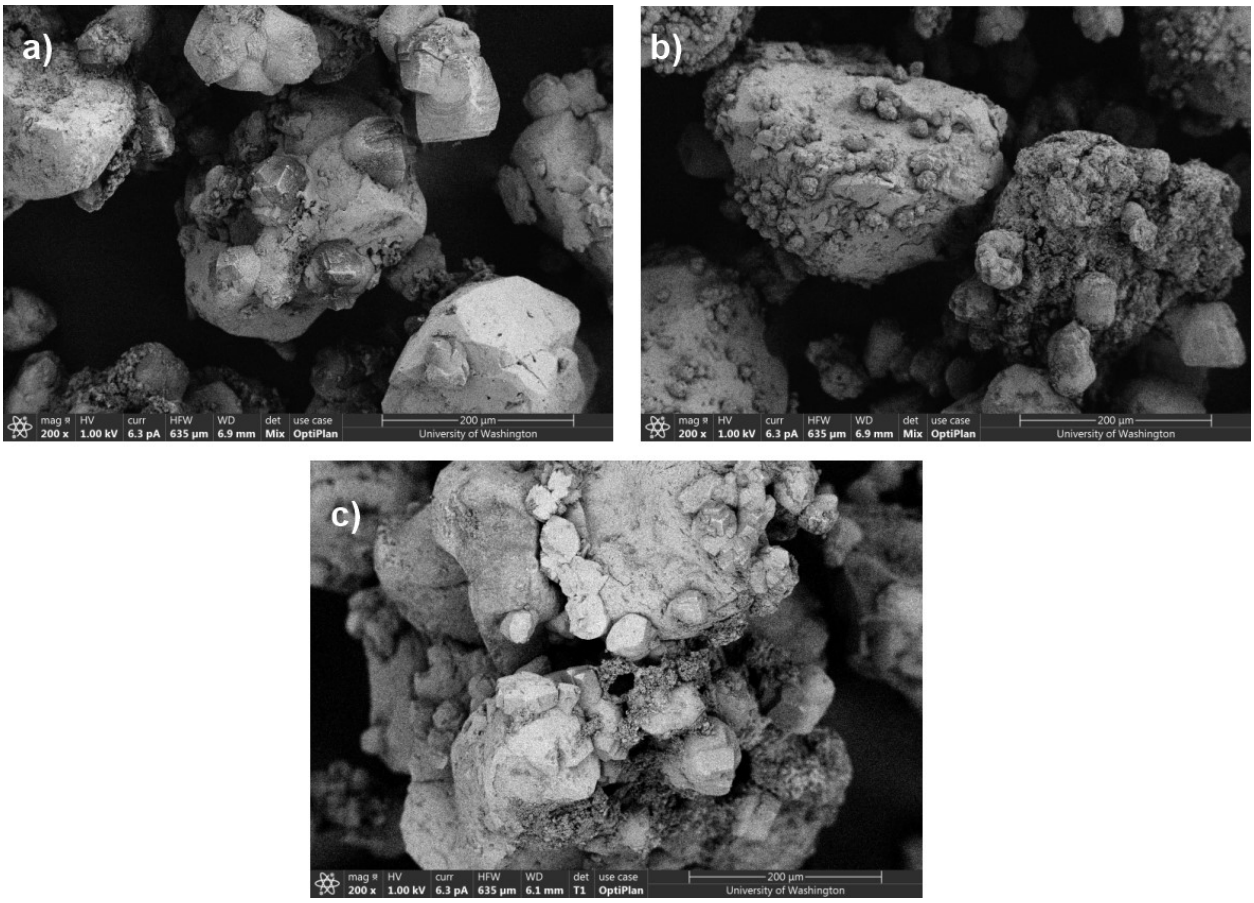

Figure 4.20 Representative SEM images of EICP experiments containing (a) 0.2% sodium alginate, (b) *B. subtilis* cell additions (6.8 x 10^7 cells/mL), and (c) both 0.2% sodium alginate and *B. subtilis* cell additions (6.8 x 10^7 cells/mL).

Chapter 5. CONCLUSIONS

Although significant advances have been made towards improving our knowledge of MICP soil improvement, critical gaps have remained in our understanding of how various treatment formulations and environmental conditions may affect process reaction kinetics, bio-cementation chemical and mechanical properties, and their collective impacts on material long-term permeance and engineering performance. In this study, a systematic sequence of small-scale batch experiments were performed to examine the effects of various practically-relevant chemical and biological factors on the MICP process with specific focus on changes in reaction kinetics and the mineralogy and morphology of produced bio-cementation. Batch experiments were designed to allow for systematic investigation and isolation of individual factors while minimizing experimental time and improving consistency of test conditions between experiments. In all experiments performed in this study, calcium carbonate precipitation was driven by urea hydrolysis mediated by either augmented *S. pasteurii* cells (MICP) or free urease enzymes (EICP). In experiments containing inoculated *S. pasteurii* cells, cell densities were estimated from OD_{600} measurements and total direct cell counts and were compared to other cell density estimates based upon observed ureolytic activity using a cell-normalized Michaelis-Menten kinetic model implemented in PHREEQC. During all experiments, small-volume solution sampling was performed in time to track changes in urea and calcium concentrations to assess the effects of experimental conditions on ureolytic activity and calcium carbonate precipitation rates. Following all experiments, end-state precipitates were characterized using x-ray diffraction measurements to assess precipitate mineralogy and quantify relative percentages of $CaCO_3$ polymorphs and scanning electron microscope imaging was used to assess precipitate morphological differences.

From the experimental investigations performed in this study, the following conclusions can be made:

- Results from experiments involving high urea and calcium concentrations (≥ ≈500 mM), artificial seawater, and magnesium (≥ ≈54 mM) and ammonium (≥ ≈100 mM) additions suggest that large reductions in ureolytic activities may occur when these factors are present. While the exact mechanisms responsible for each of these inhibitory effects are not fully known, it is suspected that some of these mechanisms may include cell death and encapsulation through greater magnitudes of precipitates formed at higher urea and calcium concentrations, inhibition of cellular and enzymatic functions including potential interactions with nickel-dependent urease enzymes in the presence of magnesium, and non-competitive inhibition of urease in whole cells by higher ammonium concentrations. Furthermore, the presence of both 54 mM magnesium and higher ionic strength in seawater (0.7 M) appear to be responsible for the majority of the ureolytic rate reductions observed in artificial seawater experiments.
- Results from experiments involving high ionic strengths (1 M) from sodium chloride additions and high concentrations of yeast extract and nutrient broth (5 g/L) suggested that the presence of these factors may result in modest reactions in ureolytic activities with a near ≈20% reduction in initial ureolytic rate. These effects may be related to changes in intercellular diffusion of urea and the addition of other trace ions in growth factor experiments.
- Mineralogical analyses of end-state precipitates formed in experiments containing high urea and calcium concentrations, artificial seawater, and magnesium, sodium, strontium, sulfate, ammonium, acetate, and molasses additions suggested only minimal changes in the

relative percentages of calcite, aragonite, and vaterite in $CaCO_3$ precipitates. In all of these experiments, calcite was found to be the predominant mineral phase, however, some notable changes in precipitate morphology were also observed. Additionally, in experiments containing high urea and calcium concentrations, destructive sampling in time suggested that vaterite may exist as a metastable phase in some of these experiments, with eventual ripening to calcite mineral as reactions proceed toward completion and achieve lower ion-activity-product conditions. Lastly, SEM imaging of precipitates from synthetic seawater experiments suggested that the presence of seawater may dramatically change the morphology, shape, and distribution of precipitates with much more amorphous mineral forms observed.

- When the effect of various growth factors on end-state precipitate mineralogy was explored, results suggested that yeast extract, nutrient broth, and molasses additions may result in large changes in precipitate mineralogy and morphology with greater relative percentages of vaterite and lower relative percentages of calcite observed at higher growth factor concentrations. Interestingly, sodium acetate, which, in contrast to the above three growth factors, contained no proteins or amino acids, was found to have no detectable effects on precipitates.
- Results from MICP experiments involving non-ureolytic *B. subtilis* cells and sodium alginate additions further suggested that the presence of spectator cells and extracellular polymeric substances during MICP may further alter precipitate mineralogy and morphology with greater relative percentages of vaterite and lower relative percentages of calcite observed in the presence of these factors. In particular, the addition of sodium

alginate had a more dramatic effect on precipitates than increases in non-ureolytic *B. subtilis* cell densities.

- When precipitates were formed in nearly identical EICP and MICP experiments, results suggested that the mediation of ureolysis by free enzymes (EICP) may result in greater relative percentages of vaterite and aragonite in precipitates when compared to precipitates produced during MICP. Additionally, much of the precipitated calcium carbonate in the EICP experiment appeared to be much more disordered than that observed in the MICP experiment, with broken or chaotic forms, possibly suggesting the presence of amorphous calcium carbonate.
- Lastly, when *B. subtilis* cells and sodium alginate additions were included in EICP experiments, even more dramatic changes in mineralogy were observed with much greater relative percentages of vaterite detected when compared to the EICP experiment without these factors. Interestingly, despite similar reaction conditions between the EICP experiment containing *B. subtilis* cells and the MICP control experiment, resulting precipitation was dramatically different. This suggested that precipitation formed in the presence of urease enzymes within whole cells cannot be reproduced when bacterial cells and urease enzymes are present separately in solutions.

In summary, the presented experiments suggest that the presence of different environmental conditions and treatment solution additions should be considered carefully for future MICP and EICP applications. While effects on ureolytic rates can be recognized and accounted for during treatment applications, changes in precipitate mineralogy and morphology may have more lasting consequences for the long-term performance of bio-cementation improved soils. Although the experiments performed in this study were not exhaustive, it is suspected that the results of these

investigations may help guide future research aimed at more fully understanding the chemical and mechanical resilience of MICP, including how various treatment and environmental factors may affect precipitate mineralogy, morphology, and distribution and, in turn, the macro-scale engineering properties and long-term chemical stability of bio-cementation improved geomaterials.

BIBLIOGRAPHY

Addadi, L., Raz, S., & Weiner, S. (2003). Taking advantage of disorder: amorphous calcium carbonate and its roles in biomineralization. Advanced Materials, 15(12), 959-970.

Al Qabany, A., Soga, K., (2013). Effect of chemical treatment used in MICP on engineering properties of cemented soil, *Bio-and Chemo-Mechanical Processes in Geotechnical Engineering: Géotechnique Symposium in Print 2013,* 63(4), 331-339.

Al-Sawalmih, A., Li, C., Siegel, S., Fratzl, P., & Paris, O. (2009). On the stability of amorphous minerals in lobster cuticle. *Advanced Materials*, *21*(40), 4011-4015.

Berner, R. A. (1975). The role of magnesium in the crystal growth of calcite and aragonite from sea water. Geochimica et Cosmochimica Acta, 39(4), 489-504.

Bladh, K. W., Bideaux, R. A., Anthony-Morton, E., & Nichols, B. G. (2001). Handbook of mineralogy. Mineralogical Society of America, Berkeley.

Blue, C. R., Giuffre, A., Mergelsberg, S., Han, N., De Yoreo, J. J., & Dove, P. M. (2017). Chemical and physical controls on the transformation of amorphous calcium carbonate into crystalline CaCO3 polymorphs. Geochimica et Cosmochimica Acta, 196, 179-196.

Braissant, O., Cailleau, G., Dupraz, C., Verrecchia, E. (2003). Bacterially Induced Mineralization of Calcium Carbonate in Terrestrial Environments: The Role of Exopolysaccharides and Amino Acids. *Journal of Sedimentary Research*, 73, Issue 3, 485-490.

Burbank, M., Weaver, T., Lewis, R., Williams, T., Williams, B., & Crawford, R. (2013). Geotechnical tests of sands following bioinduced calcite precipitation catalyzed by indigenous bacteria. Journal of Geotechnical and Geoenvironmental Engineering, 139(6), 928-936.

Chou, C. W., Seagren, E. A., Aydilek, A. H., & Lai, M. (2011). Biocalcification of sand through ureolysis. Journal of Geotechnical and Geoenvironmental Engineering, 137(12), 1179-1189.

Cuthbert, M. O., Riley, M. S., Handley-Sidhu, S., Renshaw, J. C., Tobler, D. J., Phoenix, V. R., & Mackay, R. (2012). Controls on the rate of ureolysis and the morphology of carbonate precipitated by S. Pasteurii biofilms and limits due to bacterial encapsulation. *Ecological Engineering*, *41*, 32-40.

Decho, A. W., Visscher, P. T., and Reid, P., 2005. Production and cycling of natural microbial exopolymers (EPS) within a marine stromatolite. *Palaeogeography, Palaeoclimatology, Palaeoecology*, **219**, 71–86.

DeJong, J.T., Soga, K.S., Kavazanjian, E., Burns, S., van Paassen, L., Al Qabany, A., Aydilek, A., Bang, S.S., Burbank, M., Clake, L., Chen, C.Y., Cheng, X., Chu, J., Ciurli, S., Fauriel, S., Filet, A.E., Hamdan, N., Hata, T., Inagaki, Y., Jefferis, S., Kuo, M., Laloui, L., Larrahondo, J., Manning, D.A.C., Martinez, B., Montoya, B.M., Nelson, D.C., Palomino, A., Renforth, P., Santamarina, J.C., Seagren, E.A., Tanyu, B., Tsesarsky, M., Weaver, T. (2013). "Biogeochemical processes and geotechnical applications: progress, opportunities and challenges." *Geotechnique*, 63(4), 287-301.

DeJong, J. T., Fritzges, M. B., & Nüsslein, K. (2006). Microbially induced cementation to control sand response to undrained shear. *Journal of Geotechnical and Geoenvironmental Engineering*, 132(11), 1381-1392

DeJong, J. T., & Kavazanjian, E. (2019). Bio-mediated and Bio-inspired Geotechnics. In *Geotechnical Fundamentals for Addressing New World Challenges* (pp. 193-207). Springer, Cham.

DeJong, J., Martinez, B., Mortensen, B., Nelson, D., Waller, J., et al., (2009). Upscaling of Bio-Mediated Soil Improvement, *17th International Conference on Soil Mechanics and Geotechnical Engineering*, October 2009, INL/CON-09-15487.

DeJong, J. T., Mortensen, B. M., Martinez, B. C., & Nelson, D. C. (2010). Bio-mediated soil improvement. Ecological Engineering, 36(2), 197-210.

Ferris, F.; Stehmeier, L.; Kantzas, A.; Mourits, F. (1997) Bacteriogenic mineral plugging. *Journal of Canadian Petroleum Technology*, 36, (09).

Ferris, F. G., Phoenix, V., Fujita, Y., & Smith, R. W. (2004). Kinetics of calcite precipitation induced by ureolytic bacteria at 10 to 20 C in artificial groundwater. Geochimica et Cosmochimica Acta, 68(8), 1701-1710.

Fidaleo, M., & Lavecchia, R. (2003). Kinetic study of enzymatic urea hydrolysis in the pH range 4-9. *Chemical and biochemical engineering quarterly*, 17(4), 311-318.

Fujita, Y., Ferris, F. G., Lawson, R. D., Colwell, F. S., & Smith, R. W. (2000). Subscribed content calcium carbonate precipitation by ureolytic subsurface bacteria. *Geomicrobiology Journal*, *17*(4), 305-318.

Fujita, Y., Taylor, J. L., Gresham, T. L., Delwiche, M. E., Colwell, F. S., McLing, T. L., ... & Smith, R. W. (2008). Stimulation of microbial urea hydrolysis in groundwater to enhance calcite precipitation. *Environmental science & technology*, *42*(8), 3025-3032.

Fujita, Y., Redden, G. D., Ingram, J. C., Cortez, M. M., Ferris, F. G., & Smith, R. W. (2004). Strontium incorporation into calcite generated by bacterial ureolysis. Geochimica et cosmochimica acta, 68(15), 3261-3270.

Gomez, M. G., Anderson, C. M., DeJong, J. T., Nelson, D. C., & Lau, X. H. (2014). Stimulating in situ soil bacteria for bio-cementation of sands. In *Geo-Congress 2014: Geo-characterization and Modeling for Sustainability* (pp. 1674-1682).

Gomez, M.G., Anderson, C.M., DeJong, J.T., Nelson, D.C., Graddy, C.M.R., and Ginn, T.R. (2016). "Large-scale Comparison of Bioaugmentation and Biostimulation Approaches for Bio-cementation of Sands." *Journal of Geotechnical and Geoenvironmental Engineering, 10.1061/(ASCE)GT.1943-5606.0001640.*

Gomez, M. G., DeJong, J. T., & Anderson, C. M. (2018a). Effect of bio-cementation on geophysical and cone penetration measurements in sands. *Canadian Geotechnical Journal*, *55*(11), 1632-1646.

Gomez, M.G., Graddy, C.M.R., DeJong, J.T., Nelson, D.C., and Tsesarsky, M. (2018b). Stimulation of Native Microorganisms for Biocementation in Samples Recovered from Field-Scale Treatment Depths. *Journal of Geotechnical and Geoenvironmental Engineering, 10.1061/(ASCE)GT.1943-5606.0001804.*

Gomez, M.G., Martinez, B.C., DeJong, J.T., Hunt, C.E., deVlaming, L.A., Major, D.W., and Dworatzek, S.M. (2015). Field Scale Bio-cementation Tests to Improve Sands. *Ground Improvement*, 168(3), pp. 206-216

Gomez, M. G., Graddy, C. M., DeJong, J. T., & Nelson, D. C. (2019). Biogeochemical changes during bio-cementation mediated by stimulated and augmented ureolytic microorganisms. *Scientific Reports*, *9*(1), 1-15.

Graddy, C. M., Gomez, M. G., Kline, L. M., Morrill, S. R., DeJong, J. T., & Nelson, D. C. (2018). Diversity of Sporosarcina-like bacterial strains obtained from meter-scale augmented and

stimulated biocementation experiments. *Environmental Science & Technology*, *52*(7), 3997-4005.

Hamdan, N., & Kavazanjian Jr, E. (2016). Enzyme-induced carbonate mineral precipitation for fugitive dust control. *Géotechnique*, *66*(7), 546-555.

Hoare, J. P., & Laidler, K. J. (1950). The Molecular Kinetics of the Urea-Urease System. II. The Inhibition by Products1. Journal of the American Chemical Society, 72(6), 2487-2489.

Daley, R. J., & Hobbie, J. E. (1975). Direct counts of aquatic bacteria by a modified epifluorescence technique. *Limnology and Oceanography*, 20(5), 875-882.

Huang, J., Liu, C., Xie, L., & Zhang, R. (2018). Amorphous calcium carbonate: a precursor phase for aragonite in shell disease of the pearl oyster. Biochemical and biophysical research communications, 497(1), 102-107.

Jiang, N. J., Soga, K., & Kuo, M. (2017). Microbially induced carbonate precipitation for seepage-induced internal erosion control in sand–clay mixtures. Journal of Geotechnical and Geoenvironmental Engineering, 143(3), 04016100.

Khodadadi, T. H., Kavazanjian, E., & Bilsel, H. (2017). Mineralogy of calcium carbonate in MICP-treated soil using soaking and injection treatment methods. In Geotechnical Frontiers 2017, pp. 195-201.

Knorst, M. T., Neubert, R., & Wohlrab, W. (1997). Analytical methods for measuring urea in pharmaceutical formulations. Journal of pharmaceutical and biomedical analysis, 15(11), 1627-1632.

Krajewska, B. (2009). Ureases I. Functional, catalytic and kinetic properties: A review. Journal of Molecular Catalysis B: Enzymatic, 59(1-3), 9-21.

Lauchnor, E. G., Topp, D. M., Parker, A. E., & Gerlach, R. (2015). Whole cell kinetics of ureolysis by S porosarcina pasteurii. Journal of applied microbiology, 118(6), 1321-1332.

Lee, M., Gomez, M.G., El Kortbawi, M., Ziotopoulou, K., (2020). "Examining the Liquefaction Resistance of Lightly Cemented Sands Using Microbially Induced Calcite Precipitation (MICP)", *ASCE GeoCongress 2020 Technical Papers*, Minneapolis, MN.

Li, M., Wen, K., Li, Y., & Zhu, L. (2018). Impact of oxygen availability on microbially induced calcite precipitation (MICP) treatment. Geomicrobiology Journal, 35(1), 15-22.

Mandelstam, J., & McQuillen, K. (1968). Biochemistry of bacterial growth. *Biochemistry of bacterial growth.*

Martinez, B. C., DeJong, J. T., Ginn, T. R., Montoya, B. M., Barkouki, T. H., Hunt, C., Tanyu, B., & Major, D. (2013). Experimental optimization of microbial-induced carbonate precipitation for soil improvement. *Journal of Geotechnical and Geoenvironmental Engineering*, 139(4), 587-598.

Minto, J. M., MacLachlan, E., El Mountassir, G., & Lunn, R. J. (2016). Rock fracture grouting with microbially induced carbonate precipitation. *Water Resources Research*, *52*(11), 8827-8844.

Mobley, H. L., Island, M. D., & Hausinger, R. P. (1995). Molecular biology of microbial ureases. *Microbiological Reviews*, *59*(3), 451-480.

Montoya, B. M., & DeJong, J. T. (2015). Stress-strain behavior of sands cemented by microbially induced calcite precipitation. *Journal of Geotechnical and Geoenvironmental Engineering*, 141(6), 04015019.

Montoya, B. M., DeJong, J. T., & Boulanger, R. W. (2013). Dynamic response of liquefiable sand improved by microbial-induced calcite precipitation. *Géotechnique*, *63*(4), 302.

Myszka, B., Schüßler, M., Hurle, K., Demmert, B., Detsch, R., Boccaccini, A. R., & Wolf, S. E. (2019). Phase-specific bioactivity and altered Ostwald ripening pathways of calcium carbonate polymorphs in simulated body fluid. RSC advances, 9(32), 18232-18244. Nafisi, A., Safavizadeh, S., & Montoya, B. M. (2019). Influence of microbe and enzyme-induced treatments on cemented sand shear response. *Journal of Geotechnical and Geoenvironmental Engineering*, 145(9), 06019008.

Nassar, M. K., Gurung, D., Bastani, M., Ginn, T. R., Shafei, B., Gomez, M. G., ... & DeJong, J. T. (2018). Large-scale experiments in microbially induced calcite precipitation (MICP): Reactive transport model development and prediction. *Water Resources Research*, *54*(1), 480-500.

O'Donnell, S.T., Kavazanjian Jr, E., & Rittmann, B.E. (2017). "MIDP: Liquefaction mitigation via microbial denitrification as a two-stage process. II: MICP *Journal of Geotechnical and Geoenvironmental Engineering*, 143(12), 04017095.

Paquette, J., & Reeder, R. J. (1995). Relationship between surface structure, growth mechanism, and trace element incorporation in calcite. *Geochimica et Cosmochimica Acta*, 59(4), 735-749.

Parkhurst, D. L., & Appelo, C. A. J. (2013). Description of input and examples for PHREEQC version 3--A computer program for speciation, batch-reaction, one-dimensional transport, and inverse geochemical calculations. *U.S. Geological Survey Techniques and Methods*, book 6, chap. A43, 497 p.

Phillips, A., Troyer, E., Hiebert, R., Kirland, C., Gerlach, R., Cunningham, A., Spangler, L., Kirksey, J., Rowe, W., and Esposito, R., (2018). Enhancing wellbore cement integrity with

microbially induced calcite precipitation (MICP): a field scale demonstration. *Journal of petroleum science and engineering*, 171, 1141-1148.

Phillips, A. J., Lauchnor, E., Eldring, J., Esposito, R., Mitchell, A. C., Gerlach, R., ... & Spangler, L. H. (2013). Potential CO2 leakage reduction through biofilm-induced calcium carbonate precipitation. *Environmental science & technology*, *47*(1), 142-149.

Ratke, L., & Voorhees, P. W. (2013). Growth and coarsening: Ostwald ripening in material processing. *Springer Science & Business Media*.

Raz, S., Hamilton, P. C., Wilt, F. H., Weiner, S., & Addadi, L. (2003). The transient phase of amorphous calcium carbonate in sea urchin larval spicules: the involvement of proteins and magnesium ions in its formation and stabilization. *Advanced Functional Materials*, *13*(6), 480-486.

Reddy, M. M., & Nancollas, G. H. (1976). The crystallization of calcium carbonate: IV. The effect of magnesium, strontium and sulfate ions. *Journal of Crystal Growth*, 35(1), 33-38.

Rodriguez-Blanco, J. D., Shaw, S., & Benning, L. G. (2011). The kinetics and mechanisms of amorphous calcium carbonate (ACC) crystallization to calcite, via vaterite. *Nanoscale*, *3*(1), 265-271.

Safavizadeh, S., Montoya, B. M., & Gabr, M. A. (2019). Microbial induced calcium carbonate precipitation in coal ash. *Géotechnique*, *69*(8), 727-740.

Seagren, E.A., & Aydilek, A.H. (2010). "Biomediated geomechanical processes." *Environmental microbiology,* 2nd Ed., pp. 319-348.

Smith R.W., Fujita Y., Hubbard S.S. & Ginn T.R. (2012). *Field Investigations of Microbially Facilitated Calcite Precipitation for Immobilization of Strontium-90 and other Trace Metals in the Subsurface*. US Department of Energy, Washington, DC, pp. 1–20.

Spencer, C. A., & Sass, H. (2019). Use of carrier materials to immobilise and supply cementation medium for microbially mediated self-healing of biocement. In *IOP Conference Series: Materials Science and Engineering*, 660(1), 012067.

Stocks-Fischer, S., Galinat, J. K., & Bang, S. S. (1999). Microbiological precipitation of CaCO3. *Soil Biology and Biochemistry*, *31*(11), 1563-1571.

Terzis, D., & Laloui, L. (2018). 3-D micro-architecture and mechanical response of soil cemented via microbial-induced calcite precipitation. *Scientific reports*, *8*(1), 1-11.

Tobler, D. J., Cuthbert, M. O., Greswell, R. B., Riley, M. S., Renshaw, J. C., Handley-Sidhu, S., & Phoenix, V. R. (2011). Comparison of rates of ureolysis between Sporosarcina pasteurii and an indigenous groundwater community under conditions required to precipitate large volumes of calcite. *Geochimica et Cosmochimica Acta*, *75*(11), 3290-3301.

Tobler, D. J., Maclachlan, E., & Phoenix, V. R. (2012). Microbially mediated plugging of porous media and the impact of differing injection strategies. *Ecological Engineering*, *42*, 270-278.

van Paassen, L. A. (2011). Bio-mediated ground improvement: from laboratory experiment to pilot applications. In Geo-Frontiers 2011: Advances in Geotechnical Engineering (pp. 4099-4108).

van Paassen, L., Ghose, R., van der Linden, T., van der Star, W., and van Loosdrecht, M. (2010). Quantifying Biomediated Ground Improvement by Ureolysis: Large-Scale Biogrout Experiment. *Journal of Geotechnical and Geoenvironmental Engineering*, 136(12), 1721-1728.

van Paassen, L. A., Daza, C. M., Staal, M., Sorokin, D. Y., van der Zon, W., & van Loosdrecht, M. C. (2010). Potential soil reinforcement by biological denitrification. *Ecological Engineering*, *36*(2), 168-175.

Völker, U., & Hecker, M. (2005). From genomics via proteomics to cellular physiology of the Gram-positive model organism Bacillus subtilis. *Cellular Microbiology*, *7*(8), 1077-1085.

Weil, M. H., DeJong, J. T., Martinez, B. C., & Mortensen, B. M. (2012). Seismic and resistivity measurements for real-time monitoring of microbially induced calcite precipitation in sand. *Geotechnical Testing Journal*, *35*(2), 330-341.

Whiffin, V. S., Van Paassen, L. A., & Harkes, M. P. (2007). Microbial carbonate precipitation as a soil improvement technique. *Geomicrobiology Journal*, *24*(5), 417-423.

Whitman, W. B., Coleman, D. C., & Wiebe, W. J. (1998). Prokaryotes: the unseen majority. *Proceedings of the National Academy of Sciences*, 95(12), 6578-6583.

Wingender, & Hawkins. (1999). *Microbial extracellular polymeric substances*. Springer Berlin Heidelberg.

Xiao, P., Liu, H., Xiao, Y., Stuedlein, A. W., Evans, T. M. (2018). Liquefaction resistance of bio-cementer calcareous sand. *Soil Dynamics and Earthquake Engineering*, 107, 9-19.

Xiao, J. Z., Wei, Y. Q., Cai, H., Wang, Z. W., Yang, T., Wang, Q. H., & Wu, S. F. (2020). Microbial-Induced Carbonate Precipitation for Strengthening Soft Clay. *Advances in Materials Science and Engineering*.

Ye, Y., Le Clech, P., Chen, V., Fane, A. G., & Jefferson, B. (2005). Fouling mechanisms of alginate solutions as model extracellular polymeric substances. *Desalination*, *175*(1), 7-20

Zamani, A., & Montoya, B. M. (2018). Undrained monotonic shear response of MICP-treated silty sands. *Journal of Geotechnical and Geoenvironmental Engineering*, *144*(6), 04018029.

Zhou, G. T., Yao, Q. Z., Fu, S. Q., & Guan, Y. B. (2010). Controlled crystallization of unstable vaterite with distinct morphologies and their polymorphic transition to stable calcite. *European Journal of Mineralogy*, *22*(2), 259-269.

APPENDIX A

Table 5.4. All Chemicals Used for Batch Experiments

Treatment Constituent	***Manufacturer***	***Product Number***	***Usage***
Urea	Fisher Scientific	U15-3	All plate experiments
Calcium Chloride Dihydrate	Fisher Scientific	C79-3	All plate experiments
Tris Base	Fisher Scientific	BP152-500	Cell growth media
Ammonium Sulfate	Fisher Scientific	A702-500	Cell growth media
Yeast Extract	Fisher Scientific	BP1422-500	Cell growth media, growth factor experiments
Sea Salts	Sigma Aldrich	S9983-1KG	Seawater experiments
Magnesium Chloride Hexahydrate	Fischer Scientific	M33-500	Groundwater ion experiments
Sodium Chloride	Fisher Scientific	S271-1	Groundwater ion experiments
Sodium Sulfate	Alfa Aesar	11560	Groundwater ion experiments
Strontium Chloride Hexahydrate, ACS	MP Biomedicals	152583	Groundwater ion experiments
Molasses	Fisher Scientific	S25753	Growth factor experiments
Difco Nutrient Broth, (dehydrated)	Becton, Dickinson, and Company	2330000	Growth factor experiments
Sodium Acetate Trihydrate	Fisher Scientific	S209-3	Growth factor experiments
Ammonium Chloride	Fischer Scientific	A661-500	Treatment additions experiments
Sodium Bicarbonate	Fisher Scientific	S233-500	Treatment additions experiments
Alginic Acid Sodium Salt Powder	Sigma Aldrich	180947-100G	Biological factor experiments
Urease from *Canavalia ensiformis*	Sigma Aldrich	U1500-20KU	EICP experiments
p-Dimethylamino-benzaldehyde	Fisher Scientific	D71-100	Urea assays
Hydrochloric Acid 1N Solution	Fisher Scientific	SA48-1	All plate experiments, urea assays
QuantiChrom Calcium Assay Kit	BioAssay Systems	DICA-500	Calcium assays
Ethanol Solution 96% v/v	Fisher Scientific	BP8202-500	All plate experiments

Table 5.5. Estimates of *S. pasteurii* cell densities and initial ureolytic rates for all MICP batch experiments from: (a) direct OD_{600} measurements and a total direct cell count (TDC) to OD_{600} relationship and (b) calibration to observed ureolytic activity using a cell-normalized Michaelis-Menten kinetic model implemented in PHREEQC with whole cell urease kinetic parameters from Lauchnor et al. (2015). Initial ureolytic rates were computed at a consistent urea concentration of 250 mM using kinetic parameters from Lauchnor et al. (2015) for both cases.

Experiment Series	***Experimental Details***	***(a) OD_{600}/ TDC Estimated Cell Density (10^7 cells/mL)***	***(b) PHREEQC Estimated Cell Density (10^7 cells/mL)***	***(a) Initial Ureolytic Rate Estimated from OD_{600}/ TDC Cell Densities (mM/hr)***	***(b) Initial Ureolytic Rate Estimated from PHREEQC Estimated Cell Densities (mM/hr)***
Ureolytic Rate Varied	Fast Ureolytic Rate	33.5	7.0	966.0	201.8
Ureolytic Rate Varied	Medium Ureolytic Rate	7.4	1.8	212.1	51.9
Ureolytic Rate Varied	Slow Ureolytic Rate	1.7	0.3	48.8	8.6
Concentration Varied	50 mM Concentration	7.4	1.8	66.3	16.2
Concentration Varied	500 mM Concentration	7.4	1.3	292.4	51.7
Concentration Varied	1250 mM Concentration	7.4	0.4	378.4	20.6
Urea:Ca^{+2} Ratio Varied	Ratio 0.5:1, 250 mM Urea	7.7	1.0	142.8	18.6
Urea:Ca^{+2} Ratio Varied	Ratio 1:1, 250 mM Urea	7.7	1.2	221.3	34.6
Urea:Ca^{+2} Ratio Varied	Ratio 5:1, 250 mM Urea	7.7	0.4	394.9	20.6
Urea:Ca^{+2} Ratio Varied	Ratio 0.5:1, 500 mM Urea	7.7	1.0	221.3	28.8
Urea:Ca^{+2} Ratio Varied	Ratio 1:1, 500 mM Urea	7.7	0.6	305.1	23.9
Urea:Ca^{+2} Ratio Varied	Ratio 5:1, 500 mM Urea	7.7	0.4	437.8	22.8
pH Varied	pH = 5	7.6	1.8	219.0	51.9
pH Varied	pH = 7	7.6	1.8	219.0	51.9
pH Varied	pH = 9	7.6	2.8	219.0	80.7
Seawater Varied	0% Seawater	7.6	2.2	219.0	63.4
Seawater Varied	50% Seawater	7.6	1.8	219.0	51.9

Experiment Series	*Experimental Details*	*(a) OD_{600}/ TDC Estimated Cell Density (10^7 cells/mL)*	*(b) PHREEQC Estimated Cell Density (10^7 cells/mL)*	*(a) Initial Ureolytic Rate Estimated from OD_{600}/ TDC Cell Densities (mM/hr)*	*(b) Initial Ureolytic Rate Estimated from PHREEQC Estimated Cell Densities (mM/hr)*
Seawater Varied	100% Seawater	7.6	1.0	219.0	28.8
High Concentration Time Varied	1250 mM, 5% Complete	7.1	0.6	366.3	28.3
High Concentration Time Varied	1250 mM, 20% Complete	7.1	0.8	366.3	38.6
High Concentration Time Varied	1250 mM, 60% Complete	7.1	0.6	366.3	28.3
High Concentration Time Varied	1250 mM, 100% Complete	7.5	0.6	386.6	30.9
High Concentration Time Varied	1250 mM, No Ca^{+2}	7.3	1.8	374.4	92.6
Ion Varied	Mg^{+2} (27mM)	7.1	1.1	205.2	31.7
Ion Varied	Mg^{+2} (54mM)	7.1	1.1	205.2	31.7
Ion Varied	Mg^{+2} (108mM)	7.1	0.7	205.2	20.2
Ion Varied	Sr^{+2} (0.22mM)	7.1	1.3	205.2	37.5
Ion Varied	Sr^{+2} (0.11mM)	7.1	1.4	205.2	40.4
Ion Varied	Sr^{+2} (0.055mM)	7.1	1.4	205.2	40.4
Ion Varied	SO_4^{-2}(14mM)	7.1	1.3	205.2	37.5
Ion Varied	Control	7.1	1.5	205.2	43.2
Seawater & Mg^{+2} Varied (Low Ca^{+2})	Control	6.6	0.9	189.7	25.9
Seawater & Mg^{+2} Varied (Low Ca^{+2})	Seawater	6.6	0.4	189.7	10.7
Seawater & Mg^{+2} Varied (Low Ca^{+2})	Mg^{+2} (54mM)	6.6	0.5	189.7	13.0
Seawater & Mg^{+2} Varied (Low Ca^{+2})	Mg^{+2} (54mM) + Ca (10mM)	6.6	0.4	189.7	11.5
Seawater & Mg^{+2} Varied (Low Ca^{+2})	Mg^{+2} (108mM)	6.6	0.3	189.7	9.5

Experiment Series	*Experimental Details*	*(a) OD_{600}/ TDC Estimated Cell Density (10^7 cells/mL)*	*(b) PHREEQC Estimated Cell Density (10^7 cells/mL)*	*(a) Initial Ureolytic Rate Estimated from OD_{600}/ TDC Cell Densities (mM/hr)*	*(b) Initial Ureolytic Rate Estimated from PHREEQC Estimated Cell Densities (mM/hr)*
Seawater & Mg^{+2} Varied (Low Ca^{+2})	Mg^{+2} (108mM) + Ca^{+2} (10mM)	6.6	3.2	189.7	92.3
Treatment Additive Varied	Control	7.6	1.0	219.0	28.8
Treatment Additive Varied	NH_4Cl (1000 mM)	7.6	0.6	219.0	17.3
Treatment Additive Varied	NH_4Cl (100 mM)	7.6	0.6	219.0	17.3
Treatment Additive Varied	NH_4Cl (10 mM)	7.6	0.3	219.0	9.2
Treatment Additive Varied	$NaHCO_3$ (1000 mM)	7.6	1.0	219.0	28.8
Treatment Additive Varied	$NaHCO_3$ (250 mM)	7.6	1.0	219.0	28.8
Treatment Additive Varied	$NaHCO_3$ (25 mM)	7.6	1.0	219.0	28.8
Treatment Additive Varied	Control	8.0	1.6	230.7	46.1
Treatment Additive Varied	NH_4Cl (1000 mM)	8.0	0.8	230.7	23.1
Treatment Additive Varied	NH_4Cl (100 mM)	8.0	1.2	230.7	34.6
Treatment Additive Varied	NH_4Cl (10 mM)	8.0	1.6	230.7	46.1
Treatment Additive Varied	NaCl (1000 mM)	8.0	1.3	230.7	36.0
Treatment Additive Varied	NaCl (100 mM)	8.0	1.6	230.7	46.1

Experiment Series	***Experimental Details***	***(a) OD_{600}/ TDC Estimated Cell Density (10^7 cells/mL)***	***(b) PHREEQC Estimated Cell Density (10^7 cells/mL)***	***(a) Initial Ureolytic Rate Estimated from OD_{600}/ TDC Cell Densities (mM/hr)***	***(b) Initial Ureolytic Rate Estimated from PHREEQC Estimated Cell Densities (mM/hr)***
Treatment Additive Varied	NaCl (10 mM)	8.0	1.6	230.7	46.1
Soil Varied	Ottawa F-65 Sand	8.2	2.0	235.4	57.7
Soil Varied	Feldspar	8.2	1.7	235.4	49.0
Soil Varied	Olivine	8.2	1.6	235.4	46.1
Soil Varied	Mica	8.2	2.4	235.4	69.2
Soil Varied	Covelo Sand	8.2	0.9	235.4	25.9
Soil Varied	Concrete Sand	8.2	1.3	235.4	37.5
Soil Varied	Fraser Sand	8.2	0.5	235.4	14.4
Soil Varied	Delta Sand	8.2	1.3	235.4	37.5
Soil Varied	Monterrey Sand	8.2	2.0	235.4	57.7
Soil Varied	Kaolinite Clay	8.2	2.8	235.4	80.7
Soil Varied	Montmorilloni te Clay	8.2	2.0	235.4	57.7
Biological Factor Varied	Control	6.8	1.9	196.3	54.8
Biological Factor Varied	1:1 *B. subtilis* to *S. pasteurii* cells	6.8	1.7	196.3	49.0
Biological Factor Varied	25:1 *B. subtilis* to *S. pasteurii* cells	6.8	2.1	196.3	60.5
Biological Factor Varied	Sodium alginate (0.2%)	6.8	2.1	196.3	60.5
Biological Factor Varied	Sodium alginate (2.0%)	6.8	2.1	196.3	60.5
Growth Factor Varied	Control	7.2	2.7	207.5	77.8
Growth Factor Varied	Molasses (0.1 g /L)	7.2	2.7	207.5	77.8
Growth Factor Varied	Molasses (5 g /L)	7.2	3.5	207.5	100.9
Growth Factor Varied	Yeast Extract (0.1 g/L)	7.2	3.5	207.5	100.9
Growth Factor Varied	Yeast Extract (1.0 g/L)	7.2	2.3	207.5	66.3
Growth Factor Varied	Yeast Extract (5.0 g/L)	7.2	1.0	207.5	28.8

Experiment Series	***Experimental Details***	***(a) OD_{600}/ TDC Estimated Cell Density (10^7 cells/mL)***	***(b) PHREEQC Estimated Cell Density (10^7 cells/mL)***	***(a) Initial Ureolytic Rate Estimated from OD_{600}/ TDC Cell Densities (mM/hr)***	***(b) Initial Ureolytic Rate Estimated from PHREEQC Estimated Cell Densities (mM/hr)***
Growth Factor Varied	Nutrient Broth (0.1 g/L)	7.2	3.5	207.5	100.9
Growth Factor Varied	Nutrient Broth (1.0 g/L)	7.2	3.5	207.5	100.9
Growth Factor Varied	Nutrient Broth (5.0 g/L)	7.2	1.8	207.5	51.9
Growth Factor Varied	Sodium Acetate (5 mM)	7.2	2.7	207.5	77.8
Growth Factor Varied	Sodium Acetate (50 mM)	7.2	2.7	207.5	77.8
Growth Factor Varied	Sodium Acetate (500 mM)	7.2	2.3	207.5	66.3

Table 5.6. XRD Analysis Results for Select Experiments (sorted by lowest relative percentage of calcite in $CaCO_3$ precipitates)

Experiment Series	***Experimental Details***	***Calcite %***	***Vaterite %***	***Aragonite %***
Growth Factor Varied	Yeast Extract (5.0 g/L)	59	29	12
Growth Factor Varied	Nutrient Broth (5.0 g/L)	65	23	12
Biological Factor Varied	EICP w/ *B. subtilis* cells & sodium alginate (0.2%)	67	25	8
Biological Factor Varied	Sodium alginate (2.0%)	71	22	7
Biological Factor Varied	EICP w/ *B. subtilis* cells	71	22	7
Biological Factor Varied	Sodium alginate (0.2%)	73	20	7
High Concentration Time Varied	1250 mM, 20% Complete	74	20	6
Concentration Varied	1250 mM Concentration	75	23	2
Growth Factor Varied	Molasses (5 g/L)	75	17	8
Biological Factor Varied	EICP w/ sodium alginate (0.2%)	77	15	8
Growth Factor Varied	Yeast Extract (1.0 g/L)	77	15	8
Urea:Ca^{+2} Ratio Varied	Ratio 1:1, 500 mM Urea	79	15	6
High Concentration Time Varied	1250 mM, 60% Complete	79	17	4
Biological Factor Varied	EICP	79	13	8
Growth Factor Varied	Yeast Extract (0.1 g/L)	79	14	7
Growth Factor Varied	Nutrient Broth (1.0 g/L)	79	14	7
Seawater Varied	100% Seawater	80	7	13
Soil Varied	Montmorillonite Clay	80	14	6
Seawater Varied	50% Seawater	81	10	9
Ion Varied	Mg^{+2} (108mM)	81	11	8